THE UNIVERSITY OF MICHIGAN

COLLEGE OF LITERATURE, SCIENCE, AND THE ARTS
Department of Physics

Technical Report No. 24

PERIPHERAL DIPION PRODUCTION BY PIONS OF 12 AND 18 GeV/c

L. W. Jones
E. Bleuler
D. O. Caldwell
B. Elsner
D. Harting
W. C. Middelkoop
B. Zacharov

ORA Project 03106

under contract with:

DEPARTMENT OF THE NAVY
OFFICE OF NAVAL RESEARCH
WASHINGTON, D.C.

CONTRACT NO. Nonr-1224(23)
NR-022-274

administered through:

OFFICE OF RESEARCH ADMINISTRATION ANN ARBOR

June 1966

This report was prepared as a paper for submission to Physical Review.

Peripheral Dipion Production by Pions of 12 and 18 GeV/c

L. W. Jones*), E. Bleuler**), D. O. Caldwell***),
B. Elsner+), D. Harting++), W.C. Middelkoop,
and B. Zacharov+++).

CERN, Geneva, Switzerland

June 1966
(Submitted to The Physical Review)

*) The University of Michigan and John S. Guggenheim Fellow. Supported in part by the Ford Foundation and the U.S. Office of Naval Research, contract Nonr 1224(23).

**) John S. Guggenheim Fellow. Currently at the Pennsylvania State University.

***) National Science Foundation Senior Fellow. Supported in part by the U.S. Atomic Energy Commission. Currently at the University of California, Santa Barbara.

+) Currently at DESY, Hamburg.

++) Currently at the Zeeman Laboratorium, Amsterdam.

+++) Currently at the Daresbury Nuclear Physics Laboratory, Daresbury, Lancs.

ABSTRACT

A spark chamber experiment on the peripheral production of 9245 pion pairs by 12 and 18 GeV/c incident pions is reported and analyzed in terms of the one pion-exchange model wherein the final state at the nucleon vertex contains generally one or more pions. The relevant dynamics and kinematics appropriate to this problem are reviewed, and the experimental and analysis techniques permitting good resolution and detection bias correction are discussed in some detail. From the results, fair agreement is found between the data and the one pion exchange calculation for the ρ^0 production cross sections and the nucleon vertex missing mass spectra. The ρ^0 is found to be consistent with a single peak, and no evidence of peak splitting is observed. A search for a narrow s-wave dipion resonance is made with negative results. Normalizing to the ρ^0 meson, the s-wave $\pi^+\pi^-$ scattering cross section is computed from the abundant low dipion-mass events, giving a cross section falling smoothly from 50 mb (300 MeV) to about 20 mb (600 MeV). No evidence of an s-wave resonance is found in this range of energies. The forward-backward pion-pion scattering asymmetry is found to be negative by $2\frac{1}{2}$ standard deviations below 450 MeV consistent with a negative and falling J=T=0

phase shift. The extrapolated forward-backward asymmetry and the s-wave cross section are both consistent with a J=T=0 phase shift near $|90°|$ near 750 MeV.

I. INTRODUCTION

In a CERN spark chamber experiment designed to study peripheral production of pion pairs at high energies, 9,245 events of the interactions of 12 and 18 GeV/c negative pions with nucleons have been analyzed. The data were used to explore the character of the ρ^0 meson, its peripheral "inelastic" production (i.e. production accompanied by one or more pions at the nucleon vertex), the recoil mass spectra at the nucleon vertex, and the $\pi^+\pi^-$ interaction in the s-state. Due to the nature of the geometrical detection efficiencies, the data are most numerous for events of low momentum transfer and small dipion mass. The experimental technique contained some novel features to achieve good resolution on the dipion system parameters at these high energies.

Results from a prototype experiment have been published[1] and preliminary results from this experiment have been discussed as the analysis has progressed.[2-5] In Section II the theoretical framework of the peripheral model as applied to this problem is reviewed and the special kinematical properties of the system are presented. Section III presents details of the experimental design and performance; Section IV discusses the data analysis procedures and in particular the detection efficiency problem; and Section V presents the

normalization procedure. In Section VI the data are presented and in Section VII observations are made on the character of the ρ° production cross-section magnitude, the missing mass spectra, the s-wave pion-pion interaction, and the observation of a negative forward-backward asymmetry for low dipion masses. A summary and acknowledgements complete the paper.

II. THEORY

Dynamics

The experimental data are all related to the general process wherein an incident negative pion on a nucleon gives rise to a pair of oppositely-charged pions of rather high energy, and to an undetected recoiling nucleon or nucleon system. With the restriction of events to small momentum transfers to the nucleon system and moderate values of the invariant mass at the nucleon vertex, we presume that the data can be interpreted in terms of a peripheral process, and that the dominant mechanism is one-pion exchange. The Feynman diagrams which will concern us are those of Fig. 1 where (a) represents the Chew-Low process of scattering of a real pion on a virtual exchanged pion, (b) is the same process except that a boson resonant state is assumed to be formed, and (c) and (d) correspond to (a) and (b) except that the final-state nucleon system is left excited to some higher energy and may decay through emission of pions. For convenience we shall refer to processes (a) and(b) as "elastic" and to processes (c) and (d) as "inelastic". We label the incident pion and nucleon as particles 1 and 2, respectively, and the emergent boson and nucleon systems as "particles" 3 and 4, respectively. The following definitions will be employed throughout:

μ the pion rest mass;

m the diboson rest mass (the invariant mass of particle 3;

M the nucleon rest mass;

M' the invariant mass of the outgoing nucleon system 4;

t the invariant four-momentum transfer carried by the exchanged particle (negative in the physical region), $t = (P_1 - P_3)^2 = -\Delta^2$;

p the three-momentum of the incident pion;

q the center-of-mass three-momentum of the "decay" pions of particle 3, $q^2 = (m/2)^2 - \mu^2$.

All energies and masses are expressed in GeV and momenta in GeV/c. In the expressions below $\hbar = c = 1$.

In general, the cross section for Fig. 1 for one-pion exchange is given by[6] :

$$\frac{d^3\sigma}{dm^2 dM'^2 d|t|} = \frac{1}{16\pi^3}\frac{m}{p^2M^2}\left[p_{1,3}\right]\sigma_1(m)\frac{1}{(t-\mu^2)^2}M'\left[p_{2,4}\right]\sigma_2(M') \tag{1}$$

where $\left[p_{1,3}\right]$ is the three-momentum of the incident pion in the center-of-mass of particle 3, $\left[p_{2,4}\right]$ is the three-momentum of the target nucleon in the center-of-mass of particle (system) 4, $\sigma_1(m)$ is the π-π interaction cross section at an energy m, $\sigma_2(M')$ is the π-N total cross section at an energy M':

$$\left[p_{1,3}\right] = \frac{1}{2m}\left\{\left[t-(m-\mu)^2\right]\left[t-(m+\mu)^2\right]\right\}^{\frac{1}{2}}$$
$$= \frac{1}{2m}\left[(m^2+\mu^2-t)^2 - 4m^2\mu^2\right]^{\frac{1}{2}};$$

$$\left[p_{2,4}\right] = \frac{1}{2M'}\left\{\left[t-(M'-M)^2\right]\left[t-(M'+M)^2\right]\right\}^{\frac{1}{2}}$$
$$= \frac{1}{2M'}\left[(M'^2+M^2-t)^2 - 4M'^2M^2\right]^{\frac{1}{2}}$$

For an s-wave π-π interaction characterized by a phase shift δ_o in the rest frame of particle 3:

$$\frac{d^3\sigma}{dm^2 dM'^2 d|t|} = \frac{1}{8\pi^2} \frac{[2M'p_{2,4}]\,\sigma_2(M')}{p^2M^2(t-\mu^2)^2} \frac{m}{q} \sin^2\delta_o , \qquad (2)$$

if the isospin considerations are neglected. For the process $\pi^+\pi^- \rightarrow \pi^+\pi^-$ in an s-state, both T=0 and T=2 phase shifts δ_o^0 and δ_o^2 can contribute, giving rise to a pion-pion scattering amplitude containing

$$\left(\frac{2}{3} e^{i\delta_o^0} \sin\delta_o^0 + \frac{1}{3} e^{i\delta_o^2} \sin\delta_o^2\right). \qquad (2a)$$

For a p-wave π-π interaction, the spin of the outgoing dipion state adds off-mass-shell factors of $[p_{1,3}]$ to the expression, which gives, in terms of the p-wave phase shift δ_1^1:

$$\frac{d^3\sigma}{dm^2 dM'^2 d|t|} =$$

$$\frac{1}{32\pi^2} \frac{[2M'p_{2,4}]\sigma_2(M')\,[2m\,p_{1,3}]^2\,3\sin^2\delta_1^1}{p^2M^2(t-\mu^2)^2\,mq^3} . \qquad (3)$$

In the range of dipion masses considered here (below 900 MeV) the data from bubble chambers is consistent with the dominance of only three phase shifts, all real, in the pion-pion scattering: δ_o^0, δ_o^2, and δ_1^1. Thus the scattering amplitude can be expressed more generally by

$$\left[\frac{2}{3} e^{i\delta_o^0} \sin\delta_o^0 + \frac{1}{3} e^{i\delta_o^2} \sin\delta_o^2 + 3\left(\frac{p_{1\,3}}{q}\right)\cos\theta\, e^{i\delta_1^1} \sin\delta_1^1\right]$$

where θ is defined as the polar angle between the incident

and scattered negative pion in the dipion center-of-mass system. The corresponding azimuthal angle φ is equivalent to the Treiman-Yang angle and is defined as the angle between the dipion production and decay planes in the dipion c.m. A generalized expression for the differential cross section for the process of Fig. 1 (c) which includes Eqs. (2) and (3) as special cases can be written:

$$\frac{d^4\sigma}{dm^2 dM'^2 d|t| d(\cos\theta)} = \frac{1}{16\pi^2}\frac{[2M'p_{2,4}]\,\sigma_2(M')}{p^2M^2(t-\mu^2)^2}\left(\frac{m}{q}\right) x \qquad (3a)$$

$$\left[\frac{4}{9}\sin^2\delta_0^0 + \frac{4}{9}\sin\delta_0^0\sin\delta_0^2\cos(\delta_0^0-\delta_0^2) + \frac{1}{9}\sin^2\delta_0^2 + \right.$$

$$\frac{p_{1,3}}{q}\cos\theta\left\{4\cos(\delta_0^0-\delta_1^1)\sin\delta_0^0\sin\delta_1^1 + \right.$$

$$\left.\left. 2\cos(\delta_0^2-\delta_1^1)\sin\delta_0^2\sin\delta_1^1\right\} + 9\left(\frac{p_{1,3}}{q}\right)^2\cos^2\theta\sin^2\delta_1^1\right].$$

If there is a resonance at energy m_o, width Γ, in the p-state, for example the ρ, the cross section is[7]:

$$\frac{d^3\sigma}{dm^2 dM'^2 d|t|} = \qquad (4)$$

$$\frac{1}{16\pi^2}\frac{[2M'p_{2,4}]\,\sigma_2(M')\,[2mp_{1,3}]^2}{p^2M^2(t-\mu^2)^2}\left(\frac{g^2}{4\pi}\right)\frac{m_o\Gamma}{m^2\left[(m^2-m_o^2)^2+(m_o\Gamma)^2\right]},$$

where $(g^2/4\pi)$ is the $\rho\pi\pi$ coupling constant, while moreover

$$m_o\Gamma = \frac{2}{3}\left(\frac{g^2}{4\pi}\right)\frac{q^3}{m}, \text{ and}$$

$$\sin^2\delta = \frac{(m_o\Gamma)^2}{(m^2-m_o)^2+(m_o\Gamma)^2}.$$

The width Γ is a function of energy where, for the ρ meson:

$$\Gamma = \Gamma_o \left(\frac{q}{q_o}\right)^3 \left(\frac{m_o}{m}\right) , \qquad (4a)$$

where q_o and m_o are the values of q and m at resonance. These effects are of minor importance for the ρ case, and in general Γ will be set equal to Γ_o. Numerically, for $m_o = 750$ MeV:

$$\left(\frac{g^2}{4\pi}\right) = 0.02\, \Gamma(\text{MeV}).$$

For an integration over a range of dipion mass, Δm, centered at m_o, Eq. (4) can be written as:

$$\frac{d^2\sigma}{dM'^2 d|t|} = \frac{\chi}{16\pi} \left(\frac{g^2}{4\pi}\right) \frac{[2M' p_{2,4}]\, \sigma_2(M')\, [2m p_{1,3}]^2}{p^2 m^2 M^2 (t-\mu^2)^2} , \qquad (5)$$

where:

$$\chi = \frac{2}{\pi} \tan^{-1}\left(\frac{\Delta m}{\Gamma}\right) .$$

If particle 4 is an unexcited nucleon (also mass M), Eq. (5) becomes[3]:

$$\frac{d\sigma}{d|t|} = \frac{\pi\chi}{4} \left(\frac{g^2}{4\pi}\right)\left(\frac{G^2}{4\pi}\right) \frac{(-t)\, [2m\, p_{1,3}]^2}{p^2 M^2 m^2\, (t-\mu^2)^2} , \qquad (6)$$

where $(G^2/4\pi)$ is the pion-nucleon coupling constant.

To equations (2)-(6) multiplicative terms may be included to account for (i) vertex form factors, (ii) initial and final state interactions, and (iii) spin effects due to the spin of the final state nucleon system M'. Since the target contains carbon there could also be errors from the assumption that nucleons behave independently except for screening effects.

On the other hand, the large values of M' which dominate our data would not be seriously suppressed by the Pauli principle, and we have no evidence of coherence effects; for example, the dipion yield is seen to go as $A^{0.61}$. Data from experiments for p of 2-4 GeV/c were brought into agreement with Eq. (6) by including somewhat arbitrary form factor expressions of the form[8]:

$$F^2(t) = \left\{ \frac{0.72}{1 + \left(\frac{\mu^2 - t}{4.73\,\mu^2} \right)} + 0.28 \right\}^2 \qquad (7)$$

Gottfried and Jackson have argued that a more reasonable physical basis for suppression of the cross section for the process of Eq. (6) at large values of $|t|$ is the interaction of the incident pion and outgoing particle, for example ρ meson with the target nucleon at small impact parameters[9]. It has been argued that much of this interaction might be included in an integration over final states at the nucleon vertex (integration over M') as is done in the analysis below. Thus the small impact parameter, large momentum transfer initial and final state interactions at high energies may lead primarily to excitation of the nucleon to isobar states without destroying the identity of the ρ or pion[3]. On the other hand, form factor effects should suppress the large-momentum-transfer interaction independent of the M' integration.

Jackson has emphasized that the spin of the nucleon system may be taken into account by including terms f(M') of the following form[7]. If particle 4 is the $(3/2)^+$ isobar

$(M'_o = 1238)$:

$$f_{(3/2)^+}(M') = \left[\frac{(M + M')^2 - t}{(M + M')^2 - \mu^2}\right]^2 \left[\frac{(M - M')^2 - t}{(M - M')^2 - \mu^2}\right]. \tag{8a}$$

If particle 4 is the $(3/2)^-$ isobar $(M'_o = 1512)$:

$$f_{(3/2)^-}(M') = \left[\frac{(M + M')^2 - t}{(M + M')^2 - \mu^2}\right] \left[\frac{(M - M')^2 - t}{(M - M')^2 - \mu^2}\right]^2 \tag{8b}$$

If particle 4 is the $(5/2)^-$ isobar $(M' = 1688)$:

$$f_{(5/2)}(M') \cong \left[\frac{(M - M')^2 - t}{(M - M')^2 - \mu^2}\right]^3. \tag{8c}$$

In general, for angular momentum ℓ,

$$f_\ell(M') \cong \left[\frac{(M - M')^2 - t}{(M - M')^2 - \mu^2}\right]^\ell. \tag{8d}$$

Jackson further comments[7] that it is not clear to what extent these factors should be retained when absorptive effects are important. Table I. notes some numerical values for $f(M')$ for particular resonances. These correction factors would be upper limits at each value of M', t since the pion-nucleon resonances occur for the ℓ-values near ℓ_{max} ($\ell_{max} \cong kR$), and the important exponent in $f(M')$ is ℓ_{max}. Especially at larger M' the different ℓ-values up to ℓ_{max} may give nearly equal contributions. The numerical cross sections calculated for the production of the ρ° by incident pions on nucleons are given in Table II. for a variety of incident momenta.

According to the known properties of identified resonances, the exchange of an A_2 meson could in principle contribute to the processes discussed in this paper as well

as one pion exchange. While no extensive calculations have been made, two observations are relevant. The spin of the A_2 would enhance its contribution relative to the pion; from the Regge pole viewpoint, the A_2 trajectory crosses $t = 0$ near $\alpha = 0.5$, the pion trajectory crosses near $\alpha = 0$, and the cross section should contain terms $s^{\alpha(t)}$ for each contributing trajectory. On the other hand, the propagator term, $(t-\mu^2)^{-2}$, suppresses the cross section for exchanged particles of large mass, μ, as almost μ^4. The ratio of the propagator terms for A_2 and pion exchange is about 10^{-4} for $t = 0$ and 240^{-1} for $t = -0.10(\text{GeV/c})^2$. The magnitude of this suppression has encouraged us to ignore the possible contribution of A^2 exchange processes in this study.

Kinematics

This experiment differs from typical bubble chamber experiments in at least two important respects; firstly, the incident pion energy was very high (12 and 18 GeV) and secondly, the dipion data were analyzed by integrating over a range of M' at the nucleon vertex. These two factors resulted in some kinematical curiosities, noted below.

With p,m,μ, and M specified, the character of the outgoing system can be parameterized in different ways. The three-momentum of the boson in the laboratory, p_3, and its lab angle to the incident pion, θ_p, are a sufficient set of variables. However, the choice of t and M' is equivalent, and is more immediately related to the physics. The choice of high incident energy and relatively small momentum transfers favors the selection of peripheral events. In addition the integration over M' was carried over only a fraction of the available range. In Fig. 2, the available physical area in t, $(M')^2$ space is plotted for m = 750 MeV and different values of p. The regions used in the analysis, $|t|<0.3(\text{GeV/c})^2$, $M'<2.5$ GeV and $M'<3.0$ GeV, are indicated in Fig. 3 where the plot is expanded to illustrate the behavior of the M', t boundary in the region of interest for this experiment. The extent to which the reaction is peripheral can be further seen by noting the dependence of p_3 on M' and t. With $p \gg \mu$, m:

$$(p-p_3)^2 \cong \frac{M'^4}{4M^2} + M'^2 \frac{(M^2 - t)}{2M^2} + \frac{(M^2 - t)^2}{4M^2} - (M^2 - t). \tag{9}$$

The dependence on t is small for $|t| < 0.3$ $(\text{GeV}/c)^2$ and $M' > 1.5$ GeV. Eq. (9) is plotted in Fig. 4.

In spite of this favorable situation, the identification of an event with low $|t|$, $p_3 \simeq p$, and $M' \simeq M$ is still not a guarantee of a correctly labelled peripheral interaction. For example, the process $\pi^- + p \rightarrow \omega^\circ + n$ can resemble the process $\pi^- + p \rightarrow (\pi^+\pi^-) + N^*$, if the ω is produced with the minimum momentum transfer and the decay π° goes straight backward in the ω c.m. Numerically, and 18 GeV/c incident pion can make an ω of 17.8 GeV which can decay in such a way that the two charged pions have a momentum of 16.5 GeV/c and an effective invariant mass of 520 MeV, while the π°-neutron system will appear to have an invariant mass of only $\sim$1.5 GeV. Conversely, an inelastically scattered pion could produce an isobar which in turn could decay in such a way that a pion from the isobar, taken together with the fast, inelastic pion, would appear to constitute a dipion of invariant mass below 1 GeV. For example, an 18 GeV/c pion can inelastically scatter on a nucleon to produce a mass 1450 MeV isobar state; this can in turn decay into a pion and neutron such that the over-all pion-pion-neutron final state is indistinguishable from a $\rho^\circ n$ state. Correspondingly, a collinear final state of π^-, π^+, n produced by a 12 GeV/c pion could be interpreted either as $\rho^\circ n$ (with the ρ° produced at minimum $|t|$ and decaying with $\theta = 0$) or as inelastic scattering to produce

an isobar of mass 1320 MeV. For these numerical examples the ambiguous positive pion has a lab momentum of less than one GeV/c while our system cuts off pions of less than three GeV/c, so that the actual cases of misidentification should be infrequent.

We believe that the vast majority of the events in our analysis correspond, in fact, to the processes of Fig. 1 through the restrictions to small $|t|$, moderate M', and $p_3 \simeq p$ since these cuts include a very small portion of the phase space for other channels. This situation is favored by our use of high energies, as the particle multiplicity increases as $E^{\frac{1}{4}}$, while the available phase space increases at least as E^2, and the populated perimeter of the phase plots increases as E^1.

It is likely, on the other hand, that events with very large M' do contain many mis-labeled events. Thus, a plot of events with M' > 2.5 GeV divided by events with M' < 2.5 GeV shows a broad peak near 500 MeV (Fig. 5) as one might expect from the distribution of the effective invariant mass of the two charged pion pairs from ω mesons. It is worth recalling that no amount of detailed kinematical data on any single event can determine to which vertex a particular pion, for example, should be associated, if both possibilities are kinematically allowed, or indeed if a two-vertex peripheral diagram is appropriate.

The use of variables m, M', and t for the final state complicates the analysis since the kinematical limit on M',

for example, depends on both m and t. In Fig. 6 and Fig. 7, the limiting curves of M' versus m are plotted for different values of t for p of 12 and 18 GeV/c. This is important in the evaluation of $d\sigma/dm$, as the factors in Eqs. (2)-(5) containing the M' dependence give a cross section which increases rapidly with the M' upper limit. Except for the factor $\sigma_2(M')$ (which varies slowly at larger M') the M' dependence of Eqs. (2)-(5) is of the form:

$$\frac{d\sigma}{dM'} \propto M'\left[2M'p_{2,4}\right] .$$

For the case of ρ-meson production, Eq. (5) can be simplified in the asymptotic limit of very high energy and small momentum transfer: $p \gg M' \gg M, m$; $M > |t| > \mu$. On these limits the curves of Fig. 3 are given approximately by

$$M'^2 \cong -\frac{2Mpt}{m^2} + M^2 \simeq -\frac{2Mpt}{m^2} .$$

Since $p_{2,4} \sim M'$ for $M'^2 \gg M^2, |t|$, the differential cross section for inelastic ρ° production can be approximated by

$$\frac{d\sigma}{d|t|} \propto \int_{M'^2_{min}}^{M'^2_{max}} \left(\frac{M'}{pt}\right)^2 dM'^2 \cong \text{constant}.$$

This result, independent of t and p, might lead to a violation of unitarity if extended to other boson resonance production and other exchange processes unless modifications of the

theory are invoked to suppress the reaction at both larger momentum transfers and higher energies. Alternately the model itself may be wrong.

One significant feature of the high energy of this experiment is the long decay mean-free path of emerging resonances, for example the ρ, relative to the range of nuclear forces. If the ρ meson has a width Γ = 100 MeV, the decay mean-free path is given numerically by $\lambda = 2\beta\gamma$ fermi. Values of λ taken in the center-of-mass of the final state nucleon system M' are given in Table III for different incident momenta and taking for M' a single nucleon recoil (M' = M) and a recoiling system of M' = 1.5 GeV.

In studying the peak energy and width of a resonance such as the ρ, many masking factors may enter. The m and q dependence of Γ would tend to lower the mass slightly (~5MeV). On the other hand, the term $\left[2mp_{1,3}\right]^2$ weights the values towards larger mass (~5-10 MeV). However, for low $|t|$, the M' dependence on m, and the strong weight of the maximum allowed M' on the cross section would lower the apparent peak energy in a manner depending on the t interval. Of course physical effects resulting from the mixing of the two resonances in the nucleon force field[10] may be a significant factor in shifting the ρ peak. The two-pion decay of the ω[11] and the J=T=0 proposed ϵ meson[12,13] could both distort the data in the ρ mass region, although neither would have a strong effect on the integrated cross section over the ρ peak.

III. EXPERIMENTAL ARRANGEMENT

In experiments above 10 GeV, the resolution attainable with spark chamber configurations becomes very good relative to other techniques. As momenta increase and angles decrease, good resolution can be maintained through increasing the spacing between components without significantly enlarging the detectors. Thus we believe that this technique will become increasingly valuable, and warrants detailed description herein.

The apparatus, previously described briefly,[14] consisted of two two-meter magnets and eight spark chambers, so designed that for each event the incoming pion and each of the two high-momentum outgoing bosons were momentum analyzed to about 1%. Cherenkov counters discriminated between outgoing pions and kaons over a portion of the solid angle, and an additional threshold Cherenkov counter in the beam permitted separation of incident pions and kaons. Data were taken under four sets of conditions using as a target a block of polyethylene or of carbon and with the central momentum of the incident beam at 12.16 or 18.04 GeV/c.

Geometry

The apparatus is shown schematically in Fig. 8. In Fig. 9 a photograph of the terminal section of the experiment (with the light-shielding enclosure removed) is reproduced. Each of the spark chambers contained six 1 cm. gaps and

seven plates of 0.025 mm hardened aluminum foil plus two 0.125 mm mylar windows. Chamber 7 (following the second magnet) was a double chamber. The chambers were constructed of lucite rectangular frames cemented together and to the foils with epoxy.

The second, or analyzing magnet, had an aperture of 55 x 14 cm^2 and a pole length of 2 meters. The front of the pole tips was 180 cm from the target, so that the angle subtended by the magnet aperture from the target was 0.196 radians horizontally (to the center of the magnet) and 0.037 radians vertically (to the far end of the magnet). This small solid angle coupled with the long effective length of the magnet (2.05 m at 18 kgauss) biased strongly against detecting events other than those where two high momentum particles were produced at small angles. While this selection of peripheral events corresponded with the objectives of the experiment, it also necessitated a large bias correction for detected events. Thus, the probability of detecting a ρ meson produced with a small momentum transfer at 18 GeV was about 5%, and this detection probability was a function of all the kinematical variables characterizing the event. The manner in which this detection probability was evaluated and applied to the data is discussed below.

The spark chambers were arranged in pairs with the members of each pair spaced by 1 meter, permitting a (nominal) one milliradian angle measurement of each track entering or leaving a magnet.

On each spark chamber, fiducial marks were located and the chambers were carefully surveyed relative to the magnets and to each other.

Optics

The chambers and illuminated fiducial marks were photographed by a single camera at 55:1 demagnification onto 35 mm film with a 300 mm f.l. lens. The image of each chamber was seen through three or four plane, front-surface mirrors. The optical alignment, and related problems, were very similar to those used in the elastic scattering experiment by many of the same group. This is described in detail in the literature.[15]

Trigger Logic

The objective of the scintillation counters was to trigger the spark chambers and camera to record probable peripheral dipion events, e.g., where one particle entered the target and two emerged through the solid angle and high field of the analyzing magnet. Behind the last spark chamber were two counters, one to the left of the z-axis of the experiment and one to the right. These counters were slightly larger in area than the last spark chamber, and a coincidence between them was the prime selection of a probable peripheral meson-production event. However, there is a first order focusing of meson pairs of a given invariant mass, m, along the z-axis of the system, so that for a certain range of dipion masses the trigger efficiency would be very low with this

system. This problem was remedied by placing a second pair of coincidence counters about one meter behind the first pair with the output of the two separate coincidences added in the trigger logic. The resulting trigger efficiency was a smoothly varying function of m, and fell off with increasing momentum transfer. The detection efficiency was very low when the pion pairs had the same charge or when the sign of their charges was such that they diverged in the magnet. In the analysis only oppositely-charged pion pairs were considered.

In order to reduce spurious triggers from events produced by the beam beyond the target, a set of three 5 mm thick scintillators was placed 20 cm beyond the target with the bias of each set at about $1\frac{1}{2}$ times the median pulse-height for a minimum ionizing particle. Thus a coincidence between all three indicated with a high probability that more than one particle had gone through the set; on the other hand, the probability that a dipion event from the target was missed in the counters was very small. The Landau pulse-height spread made the use of more than one counter essential. In practice, the bias on the counters was adjusted so that the loss of double pion events was negligible, while the rate for spurious triggers was suppressed by about a factor of 10. It was still observed that only about one event in ten was a dipion event useful for analysis. These dE/dx counters also provided a target themselves constituting 40% as much material as was contained in the target, and 20% of the events were due to interactions in these counters. The z-vertices of the events

from the counters permitted their separation from the "target" events, and the detection probability calculation properly included their origins. Fig. 10 contains a plot of z-vertex distributions for a sample of events.

Cherenkov Counters

Two large gas threshold Cherenkov counters were installed behind the last trigger counters to separate pions from kaons. Using gas (Freon-114 and Freon-22) at atmospheric pressure, the threshold for Cherenkov radiation could be set at $(1-\beta) = 0.00137$ or $(1-\beta) = 0.00075$, corresponding to separation of pions and kaons in the range either from 2.68 GeV/c to 9.40 GeV/c or from 3.62 GeV/c to 12.8 GeV/c. The counters were made of aluminum sheet metal, and each employed a single 5-inch photomultiplier (RCA 7046). A large spherical aluminum mirror collected the Cherenkov light onto the phototube. The counter design can be seen in Fig. 11. The Cherenkov counters were used to flash lights when they triggered in coincidence with an event trigger, and these lights were recorded on the film frame. The counters were tested in the pion beam and found to be 92% (one counter) and 96% (the other counter) efficient for pions along the axis. It is probable that a better figure for the average efficiency for pions through the counter in the experiment was closer to 90%. Of detected and analyzed events, 46.9% of the emerging bosons passed through a Cherenkov counter in the 12 GeV/c run, and 44.2% in the 18 GeV/c run. Of the particles which passed through the counters, 25.8% did not trigger

them in the 12 GeV/c run and 18.1% did not trigger them in the 18 GeV/c run. Allowing for an efficiency of about 90%, these data are consistent with emerging bosons consisting of 90% pions. In analyzing the data, we considered as dipions all events in which both of the bosons passing through a Cherenkov counter triggered it, and all events where the Cherenkov counter labelling did not exclude assignment as a dipion. This included some kaon events from these where the kaons did not pass through a Cherenkov counter and missed some dipion events due to inefficiency of the Cherenkov counter. The possible error in normalization from these sources is discussed in Sec. V.

Precision and Errors

The errors in determining momentum, dipion mass, missing mass, and other physical quantities came from the following: the alignment of the spark chambers and their fiducials in the laboratory, the alignment of the optics, the film resolution, the precision of film digitization, multiple Coulomb scattering, and magnetic field calibration. The original surveying precision was ±0.2 - 0.3 mm in the laboratory. By autocollimation of the system the optics were aligned to correspond to a maximum parallax error (between sparks and fiducial marks) of ±0.3 mm, except in the horizontal views of the last large spark chambers (±0.5 mm). The film was digitized to a precision of ±7 microns least count with image plane digitizers at CERN for approximately two-thirds of the events, and to ±2.5 microns or ±1 micron with focal-

plane digitizers at Michigan and MIT for the remaining one-third of the events. The poorer figure corresponds to ±0.4 mm. in the laboratory, and probably represents a working average uncertainty. Film grain did not seem to be a limitation here. These errors combine to give ±0.55 mm. uncertainty in the location of a track segment crossing a fiducial line. For two track segments spaced by one meter, the angle uncertainty is ±0.78 milliradians. The error in determining a bending angle (momentum) or the opening angle of a pair of tracks is then ±1.1 milliradians. For a 2 meter, 18 kgauss magnet, the bending angle-momentum product $p\theta = 1.08$ GeV/c radians. The momentum measurement uncertainty is then given by

$$\delta p = 0.92 p^2 \delta\theta = \pm 10^{-3} p^2; \quad \frac{\delta p}{p} = \pm 10^{-3} p \ . \quad (10)$$

For p = 12 GeV/c, $\delta p/p = \pm 1.2\%$; for p = 18 GeV/c, $\delta p/p = \pm 1.8\%$. These errors are reflected directly in comparing the momenta of beam pions as measured in the two magnets, and such measurements bear out the validity of this analysis, giving ±2% as the measured difference between the momentum of 12 GeV/c beam pions between the two halves of the system and ±3% as the measured difference for 18 GeV/c beam pions.

Multiple Coulomb scattering adds to the measurement uncertainty, and considering other possible sources of error, the measured values of $\delta p/p$ seem surprisingly good. However, each track is overdetermined, and least squares fitting is used to improve momentum and angle measurements. The field

is known from field maps and from wire orbits to a precision of much better than 1%.

Multiple scattering can be important for low momentum pions. It would enter both in the determination of the opening angle, θ_o, of two emerging pions from the target and of the momentum of either pion.

For the opening angle determination, track co-ordinates in the two spark chambers beyond the target are read. Scattering in the target, the air, and the first spark chamber would affect this angle; assuming that an average event originates in the target center, there are 0.08 radiation lengths of matter before the second spark chamber, corresponding to an angle uncertainty $\delta\theta = 0.0042/p$ (GeV/c). Thus for a 4 GeV/c pion, multiple scattering would introduce an uncertainty comparable to the resolution factors discussed above.

The measurement of a momentum is deteriorated by multiple scattering in 5 m. of air and two spark chambers containing 0.02 radiation lengths of material. This contributes an uncertainty $\delta\theta = 0.0021/p$ (GeV/c), so that the scattering uncertainty exceeds the measurement only below 2.1 GeV/c.

For momenta of the emergent pions, p_+ and p_-, large compared to the pion rest mass, μ, and θ_o small, the dipion mass is given by

$$m^2 = \mu^2 \left[2 + \frac{p_+}{p_-} + \frac{p_-}{p_+} \right] + p_+ p_- \theta_o^2 .$$

For nearly symmetric decays, $p_+ \simeq p_-$

$$\delta m \cong \frac{p_3}{2} \delta\theta$$

where p_3 is the dipion momentum in the laboratory. This expression includes the relationships of Eq. (10) above for this particular magnet, and the expression is valid to within a factor of two for p_+ and p_- differing by a factor of two. The discussion above leads us to expect errors in dipion mass of 1% or 2% even for ρ mesons produced at 18 GeV. From goodness of fit tests of measurements in the ρ-mass region, the errors in δm inferred from our data are ±11 MeV (12 GeV/c ρ events) and ±15 MeV (18 GeV/c ρ events).

While the dominant dipion states studied here (e.g., the ρ°) are too broad to permit a measurement of the mass resolution, a qualitative check on the resolution is possible from a selection of $\pi^+\pi^-$ pairs from K_1° decays. Since the K_1° decay mean free path at these energies is tens of centimeters, a $K_1^\circ \longrightarrow 2\pi$ event should appear in our analysis as a dipion of mass 494 MeV with a "production" vertex downstream from the target. Accordingly we have plotted the mass spectrum of dipions with their z-vertex coordinate between 7 and 17 cm from the target center (e.g., between the target and the ionization counters). As presented in Fig. 12, this shows contributions from the tails of the target vertex distributions where the increasing opening angle at higher masses and lower incident energy gives better resolution and corresponding fewer events in this interval. However, a clear peak in the mass bin from 490 to 495 MeV is apparent,

especially in the 12 GeV/c data. This meager K^o data is consistent with or better than the resolution discussed above.

The missing mass, M', is given approximately by

$$(M')^2 \cong M^2 + 2M(p - p_3) ,$$

so that

$$\delta M' \cong \frac{M}{M'} \delta (p - p_3) .$$

For nearly symmetric dipion decays, $p_3 \cong 2p^{\pm}$; the error $\delta p^{\pm}$ should be about $\frac{1}{4} \delta p$, or δp_3 would be about $(2)^{\frac{1}{2}} \delta p/4$. Hence the missing-mass error is dominated by the momentum error in the incident beam. From these considerations we believe that $\delta M' \cong 0.17(M/M')$ for 12 GeV/c and $\delta M' \cong 0.35(M/M')$ for 18 GeV/c. In addition to measurement uncertainties, the Fermi motion of nucleons in carbon adds further uncertainty in the missing mass as the assumption that the target nucleon is initially at rest is not valid. For a collinear process, where the Fermi momentum, p_2, the incident pion, and the emerging dipion all lie on a single line,

$$(M')^2 \cong (M'_A)^2 \left[1 \pm \frac{P_2}{M} \left(1 - \frac{M}{M'_A} \right)^2 \right]$$

where M_A is the missing mass inferred neglecting the Fermi motion. For $M'_A = M'$,

$$\delta M' \cong \frac{p_2}{2} \left(1 - \frac{M}{M'} \right) .$$

Thus a 150 MeV/c Fermi momentum gives rise to a ±75 MeV

missing-mass uncertainty.

The errors on the four-momentum transfer, dipion decay angles, etc., are all small and of less consequence in the analysis than errors in dipion mass or missing mass.

IV. DATA ANALYSIS

Film Digitization

Over 200 000 photographs were taken in the experiment and scanned for probable diboson events. The selected frames were digitized as described below. For each event the measurement consisted of recording co-ordinates of four fiducial marks and of two points for each track segment in each chamber. The points chosen to define the track segment were the intersections of a line superposed through the relevant set of six sparks and intersecting two parallel fiducial lines recorded on either side of each chamber view. The orientation of these reference lines was precisely known from surveying and from the measurement of a "fiducial set". A "fiducial set" was a digitization of 46 fiducial points on a film frame. These contained the four reference fiducials used for each event and from 2 to 6 fiducials for each of the 16 chamber views (two stereo views of each of the eight chambers). On the views of the larger chambers (35 and 120 cm) up to 6 fiducial measurements, or about one measurement every 15 cm. of real space, permitted correction for possible distortion of the image over the chamber area due to possible curvature of the mirrors. These calibration measurements were stored in the form of geometrical transform coefficients in the computer. A "fiducial set" was measured about every 200 film frames and used as a reference for events

recorded subsequently since it was observed that gradual changes in mirror positions caused observable changes in the fiducial co-ordinates. A typical film frame is reproduced in Fig. 13, and the spark chamber positions on the film are noted in Fig. 14.

Each digitized event was stored on magnetic tape and processed by the SCRAP[16] program system. There are four main phases of the SCRAP program: geometrical reconstruction, event selection on the basis of specified topology, geometrical optimization, and kinematic analysis. After geometrical reconstruction of each track in terms of real space parameters, the input data was filtered and selected for a possible two-prong event; in cases of ambiguity or of more than one interaction vertex, each possibility was stored sequentially for further processing. Thus, for example, frequently three or more closely spaced tracks appeared in the chambers just beyond the target, but only two tracks continued beyond the analysis magnet. In some of these cases, the pairing of track segments to correspond to particle trajectories was ambiguous. Events not satisfying established criteria and tolerances were listed separately, together with the reason for their rejection.

Events which satisfactorily passed the selection phase of SCRAP were optimized by the use of constrained least-squares fitting techniques. This was possible here because the measurements over-determined the topology, and were very valuable in obtaining the best values of spacial parameters

and momentum for each track. In this experiment the optimization of the interaction vertex[17] was performed separately from the trajectory optimization[18] for each of the three relevant particles.

Because there was no kinematical over-determination, kinematical analysis of each event was performed simply by calculating a suitable set of kinematic quantities, completely specifying the event in both laboratory and c.m. systems. In general, since the nature of the decay particles could not be assumed a priori, the kinematical analysis was performed for three assumptions separately: both decay particle pions, both kaons, or one pion and one kaon. Then, with a knowledge of the decay particles momenta, their path-length through the Cherenkov counters and the threshold for detection in the counters, together with the actual recorded response of the Cherenkov counters, a best hypothesis could be made for the nature of the parent diboson (namely, dipion, dikaon, or kaon-pion).

All the parameters, both geometrical and kinematical, specifying each good event were stored on a data summary or abstract tape together with the calculated errors and best kinematical hypothesis.

The abstract tape was finally sorted and duplicate events eliminated, and subsequently processed using the CERN SUMX routines in order to produce the histograms, lists, and other plots desired.

Weighting Factors

For each event two sets of detection probabilities (reciprocal weighting factors) were calculated and recorded on the abstract tape. For the first set (I), the diboson production azimuth was considered to be the only unessential variable, whereas all other variables - production coordinates, incident beam direction, dipion production and decay polar angles, and relative decay azimuth - were kept fixed. The detection probability, then, was the range of production azimuthal angles which would allow the two particles to be detected, divided by 2π. For the second set (II), the decay probability was assumed to be independent of the relative decay azimuth, as postulated by Yang and Treiman[15] for a one-pion-exchange peripheral interaction.

Each set contained four different detection probabilities, depending on the possible use of the Cherenkov counter information:

i) neither of the particles was required to enter the Cherenkov counters;

ii) one particle had to traverse the left Cherenkov counter in such a manner that a pion could be distinguished from a kaon, whereas the other particles were not constrained;

iii) as (ii), but for the right-hand counter;

iv) both particles had to be identifiable in their respective Cherenkov counters.

In each case, the azimuthal ranges were also constrained by the requirement of proper traversal through the scintillation coincidence counters, i.e. events triggered by a third particles would be discarded. Further restrictions arose from the requirements that both particles had to miss an anticoincidence counter placed immediately behind the magnet pole tips and that their lateral excursions in the magnet had to stay within limits set by the field drop-off. In setting these limits, we were forced by the complications arising from the field inhomogeneities to adopt arbitrary safe values and to let the computer decide whether to accept an event for evaluation, rather than the coincidence and veto counters. In particular, the initial particle directions were required to lie between two planes defined by the production vertex and two lines passing two millimeters inside the horizontal boundaries of the window of the veto counter. Experimentally, of course, the vertical focusing allows particles to pass the window even if they start with larger vertical excursions. For such detected events, then, no detection probability was calculated and they were not used for the computation of cross sections and angular distributions.

The method used for the calculation of a detection probability of set I (fixed dipion decay azimuth, $\Delta\varphi = \varphi_N - \varphi_P$) is illustrated in Fig. 15. The subscripts N and P refer to the negative and positive emergent pions, respectively. Note that fixed $\Delta\varphi$ is equivalent to fixed φ. The initial direction of each particle in the laboratory is

represented by a point whose coordinates are $f \equiv dx/dz$ and $d \equiv dy/dz$. The limits d_{max} and d_{min} are set as described above. There are up to four pairs of allowed regions for the horizontal excursions, depending on the trigger and Cherenkov counter requirements. They were obtained by using the main program to find, for selected values of f, the values of k (the central-field curvature of the path) which would make the particle hit the edges of the counters. Analytic approximations for the limits f(k) for all counter edges were then found. The values f(k) depend somewhat on d, i.e., the vertical boundary lines in Fig. 15 should be slightly curved due to vertical focusing effects. Except for marginal cases, the influence of the curvature is small and has been neglected in this calculation. As shown in Fig. 15, the allowed azimuths for the two particles N and P (shaded regions) were calculated in the small-angle approximation, the loci for N and P being circles. Those parts of the allowed regions which overlap properly, i.e., where $\varphi_N - \varphi_P$ has the fixed experimental value (cross-hatched) yield the detection probability.

For set II, both the production and the decay azimuth were varied. Forty equal (9°) steps in the c.m. dipion decay azimuthal angle φ were taken. For each value of φ an event with the same p, m, M', t, θ, etc., was generated by the computer and a detection probability of set I was computed. The φ-averaged detection probability, P_{II} is

then given by

$$P_{II} = \frac{1}{40} \sum_{i=1}^{40} P_{I_i}$$

where P_{I_i} are the appropriate set I detection probabilities.

An alternative procedure for generating weighting factors would have been to make a Monte-Carlo sample of events and compute their detection probabilities, and to apply these to the observed events. However this procedure would be subject to bias unless an unreasonable large data sample were used. Each event is characterized, not only by (p, m, M', t, θ, and φ) but by the vertex coordinates in the target and the direction of the incident pion. In principle the detection probability depends on all of these. As an example, in order to study ρ mesons produced at $|t| < 0.1$, $M' < 2500$ MeV and $|\cos\theta| < 0.3$, some assumed distribution of all variables would have to be assumed to choose the correct Monte-Carlo sample. In the method used, the sample of events used to find such a detection probability is just the experimentally detected sample, so that the distribution of, for example, target vertices, is the most suitable one. This argument only breaks down where the detection probability as a function of some variable is zero over a fraction of the range of that variable considered. We have taken particular care to avoid this pitfall, and find that this is a serious problem here only for the φ decay angle of the dipion. For this reason we have computed and used the set II

weighting factors, where φ-isotropy is assumed and the detection probability computed accordingly.

V. NORMALIZATION

The data in this experiment are used in three ways: as raw data, as data weighted for detection probability, and as data weighted and normalized for determination of absolute cross sections. Below we discuss the parameters which enter into the normalizations and the resulting uncertainties.

About one-quarter of the film was carefully rescanned and remeasured to find the absolute number of detected and measured dibosons per incident beam pion. The normalization was done separately for 12 and 18 GeV/c incident pions and for carbon and polyethylene targets.

In order to reduce the numbers of events to cross sections, it was also necessary to know the ratio of events from the polyethylene target (with mass and momentum transfer cuts) to events from both the target and the dE/dx counter. This ratio was 0.769. After making this correction it was no longer necessary to distinguish between events from the dE/dx counters and the target, except in so far as the correct vertex was used in the detection probability determination for each event.

From rescanning and remeasuring the film it was learned that a remaining 2% of the events may have been missed even on a second scan and second measurement. Another 3% were missed from program restrictions on the magnet trajectory and vertex constraints (the program clipped the

extremes of the distributions to this extent in order to reject spurious or false events).

From measurements of beams of pions of this length and energy at CERN, it is known that there is a 5 ± 1% muon contamination in the pion beam. From 9245 events in the experiment, 60 were initiated by kaons as deduced from a threshold Cherenkov counter in the incident beam.

The number of incident beam mesons giving one analyzed diboson event was 2.794×10^{-5} based on 1819 dibosons from the 12 GeV/c data and 1.247×10^{-4} based on 1143 dibosons from the 18 GeV/c data. These figures include corrections for the fraction of the film from which good events were taken (e.g. no event was digitized from frames where two or more incident pions appeared in the spark chambers before the target). The entire data sample contains 5111 dibosons from the 12 GeV/c data and 4134 dibosons from the 18 GeV/c data. For a single event, the cross section is given by

$$\sigma_i = \frac{f}{\pi_o n N E \left[\pi/(\pi+\mu)\right]} \frac{1}{P_i}$$

where: f is the fraction of events from the target, 0.769;

π_o is the corrected number of incident mesons per event;

n is the total number of analyzed events;

N is the effective number of target nucleons, 0.885×10^{24} (see below);

E is the scanning and measuring efficiency, 0.95;

$[\pi/(\pi + \mu)]$ is the fraction of the beam which is pions, 0.95;

P_i is the detection probability of the event in question.

For the numbers presented above, the parameters give, for the two energies,

$$\sigma_i = 5.25 \times 10^{-33} \frac{1}{P_i} \text{ (12 GeV/c)}$$

$$\sigma_i = 2.89 \times 10^{-32} \frac{1}{P_i} \text{ (18 GeV/c) .}$$

The combined statistical uncertainties on these figures are ±5% due to statistics on all factors except N, the effective number of nucleons in the target.

A given number of events contained in a certain interval of m, M', t, cos θ, etc., are converted to a cross section by averaging their detection probabilities and multiplying the value of σ_i by the number of events. For example if k events have detection probabilities P_i,

$$\overline{P} = \sum_{i=1}^{1} P_i \Big/ k \ .$$

$$\sigma = (5.25 \times 10^{-33} \ k/\ \overline{P}) \text{cm}^2$$

if the events are from the 12 GeV/c data.

In order to deduce an effective number of nucleons in the target (to infer a cross section per nucleon) data from the carbon and polyethylene targets were compared. This was done by comparing the ratios of events from the target and

from the dE/dx counters (sorted in the analysis according to the axial vertex co-ordinate of each event) from the two targets, and at both energies. This method has the advantage of being independent of absolute normalization. The target events were only used for M' < 2200 MeV (12 GeV/c data) and M' < 2500 MeV (18 GeV/c data) and for $|t| < 0.30$ $(GeV/c)^2$, while all analyzed events from the dE/dx counters were used. Table IV gives the numbers of events involved in this study, where the target events are further separated according to low m events and ρ events. The carbon target consisted of a 2 cm. high-density carbon block fixed to a 5 mm thick scintillation counter. It contained 5.67 g carbon, 0.04 g hydrogen. The polyethylene target was 3 cm. CH_2 fixed to the same counter and contained 2.79 g carbon and 0.43 g hydrogen. The weighted average ratio of yield from the polyethylene and carbon targets was 0.670 ± 0.082 for m < 650 MeV events and 0.708 ± 0.097 for 650 < m < 850 MeV (the ρ events). These values correspond to A^n where $n = 0.56 \begin{smallmatrix} + 0.24 \\ - 0.16 \end{smallmatrix}$ (for ρ events) and $n = 0.63 \begin{smallmatrix} + 0.25 \\ - 0.15 \end{smallmatrix}$ (for m < 650). The large uncertainty is due to the small sample of data from the carbon target.

Since the difference between low mass and ρ events is not significant, we have averaged the two ratios, giving a ratio yield of 0.687 ± 0.063. The n value thus determined is $0.61 \begin{smallmatrix} + 0.14 \\ - 0.13 \end{smallmatrix}$. The target contains then $1.47 \begin{smallmatrix} + 0.48 \\ - 0.26 \end{smallmatrix}$ grams of effective nucleons, or $0.885 \times 10^{24} \begin{smallmatrix} + 33\% \\ - 18\% \end{smallmatrix}$ effective nucleons. This error is reflected in an uncertainty in cross sections

of -33%, + 18%. The difference in these numbers between 12 and 18 GeV/c was not significant and the data from the two energies are averaged above. The best value of the exponent, 0.61, would mean that the carbon nucleus contains 4.55 effective nucleons, or 2.27 protons and 2.27 neutrons. Thus for the polyethylene target, approximately two-thirds of the effective nucleons are protons, half of them bound in carbon, and one-third of the nucleons are neutrons, all bound in carbon. For comparison with theory we shall consider the proton-to-neutron ratio in the target as 2:1.

As discussed above in connection with the Cherenkov counters, the labeling of events as dipions is subject to uncertainty both because only about half the bosons pass through Cherenkov counters and because the efficiency of the counters is not certain. Table V lists relevant percentages of bosons through the Cherenkov counters and their indicated fraction of kaons. From these figures, maximum errors on dipion yields are possible under either of two extreme assumptions: either the Cherenkov counters are 100% efficient and the number of kaons is relatively large, or the lack of a count in the Cherenkov counter indicates only inefficiency, and every boson is a pion. In the first case, if one assumes that each boson missing a counter is as likely to be a kaon as those detected, then the overestimate on dipion cross sections by assuming that all bosons which missed the counters were pions is 26.3% (12 GeV/c), 17.1%

(18 GeV/c), or 22.1% (the weighted average over 12 and 18 GeV/c). This is an extreme limit, as we know that Cherenkov counters are not 100% efficient; a suitable standard deviation would be about half of these figures. In the second case, if all dibosons are dipions the cross section has been underestimated by 17.5% (12 GeV/c), 12.5% (18 GeV/c), or 15.3% (the weighted mean of 12 and 18 GeV/c). Again these are extreme limits to the error. If the appropriate standard deviations are half of these figures, then for the combined data the Cherenkov counters introduce an uncertainty in the dipion normalization, and consequently the cross sections of +7.7%, -11.1%. Combining this with the statistical uncertainty (±5%) and the A^n uncertainty, +18%, -33%, the over-all normalization of the data is uncertain by +20%, -38%.

VI. DATA

Unweighted Dipion Spectra

The raw dipion mass spectrum data are presented in Figs. 16, 17, and 18. From these histograms the numbers of events in different regions of mass and momentum transfer can be appreciated. While the ρ^0 meson is persistently apparent, essentially all other structure in the raw mass spectra is a consequence of the varying detection probability or of limited statistics. In particular the peak at low m is due entirely to the large detection probability for those masses.

It has been suggested[12] that a narrow peak in the $\pi^+\pi^-$ s-wave system could be seen in the presence of a large ρ by selecting only events with small $|\cos\theta|$ and exploring their mass spectrum. On this basis the Pennsylvania group reported observation of a peak between 700 and 750 MeV. We have selected all events in our unweighted data between 600 and 900 MeV with $|t| < 0.10$ $(\text{GeV/c})^2$ and $|\cos\theta| < 0.30$. This mass spectrum is plotted in Fig. 19. For comparison, the data in the same dipion mass interval but without cuts in t or $\cos\theta$ are given in Fig. 20. The slowly-falling detection probability is apparent and there is some evidence of a broadly-peaked resonance roughly corresponding to the ρ even in Fig. 19. However, we do not see any peak which would

have a width narrower than 100 MeV and a mass less than 750 MeV. As this data sample contains over three times more events than the published Pennsylvania data, we believe that their evidence may have been only a statistical fluctuation.

Weighted Data

As discussed in Section IV , a detection probability P_{II} was assigned to each event. All data were divided into the two incident momentum groups, p of 12 and 18 GeV/c; four intervals of momentum transfer $|t|$, with cuts at .05, .10, .20, and .30 $(GeV/c)^2$, 25 MeV bins of dipion mass m; and bins of 0.10 in cos θ. For a given interval of m, p, and t, the dependence of detection probability on M' was found to be less than 12% over the ranges considered, and consequently no dependence of the detection probability on M' was used.

For each interval of p, t, m, and $|\cos \theta|$ an averaged detection probability was found for all events within the interval. Then for each p and t interval, a two-dimensional smoothing was performed on the averaged detection probabilities versus m and $|\cos \theta|$. This removed anomalies due to statistical fluctuations in detection probabilities within each interval (seldom over about 20%). It was necessary to take care that weighted distributions were only taken over intervals wherein P_{II} is non-zero; when the detection probability falls to zero within an interval the number of weighted events is an underestimate by an unknown amount. Therefore in fits discussed below, the last interval of $|\cos \theta|$ which

contained events for a given m interval was dropped (usually these were larger values of cos θ ; only for low m were events with cos θ > 0.9 detected). As discussed in IV, the detection probabilities were computed averaging over the φ angle of the pion-pion system just because of these capricious zeroes. We, therefore, have in our results no test of the Treiman-Yang isotropy.[19] We have explored our φ distributions observed anc compared them in specific cases with the distribution obtained from a Monte Carlo sample of φ-isotropic events sent through the same geometry. From these tests we can say that our data are consistent with φ isotropy. From lower-energy bubble chamber data, the φ distributions are sufficiently isotropic so that our cos θ and mass plots would not be altered by the amounts of anisotropy reported.

Dividing the number of events in each interval by the average smoothed detection probability in each interval then gave a number of weighted events which could be interpreted directly as a cross section, as discussed in Section V.

The weighted data were sufficiently sparse when subdivided as described above so that fits in 25 MeV intervals of dipion mass to cos θ expansions were not very significant. Therefore, two separate treatments of the data were made. First, the weighted data in each 25 MeV dipion mass interval (and each of the p and t intervals) were added over all intervals of cos θ. This gave a mass spectrum of dipions in each interval, and (when added together) combined over all observed momentum transfers which would reveal any fine structure in the mass spectra but would be incorrect to

the extent that the detection probability varies with cos θ and the true dipion distributions vary with cos θ and mass. Thus, in the ρ mass region where large $|\cos\theta|$ is less efficiently detected these mass plots underestimate the mass spectrum, relative to the low-mass region. These results are plotted in Figs. 21 and 22.

From the data weighted in this way, we attempted to explore the mass and width of the ρ^0 meson peak, and in particular to study any possible splitting of the peak into two sub-peaks or a systematic shift of the peak position with momentum transfer. Data from 600-900 MeV in dipion mass were fit in each momentum transfer interval.

The results of this fitting are given in Table VI. In no case did the fit to a two-peak hypothesis show a better χ^2 than the one-peak fit, and we conclude that in this data there is no evidence of a split peak. There is some trend toward a larger value of m_o with larger $|t|$, although this may not be significant. The width, Γ, is less significant in this data as it will be influenced by the changing angular distributions through the resonance region and the varying detection probability with θ, the pion-pion polar scattering angle. In particular, the detection probability is greater for smaller values of $|\cos\theta|$, and the ρ meson contributes mostly large $|\cos\theta|$. This can result in an erroneously large Γ for the ρ and we believe that the values of Γ are therefore overestimates of the true widths of the ρ meson. On the other hand, fits to the data after extrapolating

the cos θ distributions would suffer in statistical significance from the various uncertainties in these manipulations.

The second treatment of the data combined the weighted numbers of events over 100 MeV dipion mass intervals but still separated in cos θ. These weighted data were then fit to a cos θ expansion:

$$f(\theta) = a_o + a_1 \cos\theta + a_2 \cos^2\theta$$

and the value $b_o = a_o + a_2/3$ was computed. The fitting program also gave errors on these four coefficients. Through the relationship of Section V the reduction of these coefficients to absolute cross sections was done. Tables VII and VIII give values of a_o, a_1, a_2, and b_o with errors for each 100 MeV interval of dipion mass over the ranges of t covered. Also given are the values of σ, the dipion production cross section, in each interval in microbarns.

It is possible to improve the data presentation by combining the fine-grained mass spectra obtained ignoring the angular dependence with the coarse-grained mass spectra deduced from the cos θ fits. We assumed no rapid (i.e., within intervals of less than 100 MeV) changes in the angular distributions occurred; then the structure of the mass spectrum within each 100 MeV interval was determined from the fine-grained mass spectra but the normalization over each interval was taken from the coarse-grained but accurately-extrapolated coefficients of the cos θ distributions. The resulting mass spectra are given in Figs. 23 and 24. Even in these plots the ρ meson appears less strongly than lower dipion

masses when compared with low energy bubble chamber data. This is due to the fact that the data here are integrated over M', and more M' "space" is included in the low -t, low m data than in the ρ data for the same t. As the raw data is manipulated as described here, some errors in detail are bound to creep in. For example, the statistics of the $800 < m < 900$ MeV data at 12 GeV/c are quite poor, but to the extent that they exist they fit a large a_2/a_o (small Q value in Table XI). This forces an extrapolation of the data to larger cross section values near 800 MeV and shifts the apparent ρ^o peak energy to higher masses that the corresponding 18 GeV/c data. We do not believe that this represents any genuine discrepancy between 12 and 18 GeV/c or with lower energy values. It does indicate some of the potential pitfalls in this procedure, and it is for this reason that the most significant interpretations of the data are those made after a minimum of manipulations. The data on the ρ meson peak mass and width cited above were thus taken with only the first weighting procedure applied to the data.

VII. RESULTS

From the weighted dipion spectra and angular distributions several physics analyses could be made. Over the 100 MeV interval from 700 to 800 MeV the ρ° production cross section can be found as a function of t and p. From the isotropic portion of the data a production cross section for s-wave dipions can be obtained, and an s-wave pion-pion cross section deduced. The ratio of s- to p-wave can be found and the forward-backward asymmetry can be deduced versus dipion mass and momentum transfer. Finally, missing mass spectra for low dipion mass and for ρ mesons can be analyzed.

Production of the ρ° Meson

The values of b_o for $700 < m < 800$ MeV as deduced above were converted to cross sections, and these dipion production cross sections are given in Table IX for p of 12 and 18 GeV/c and in each interval of t. Also given are the values calculated from Eq. 5 where the calculation has used $m_o = 750$ MeV, $\Gamma = 100$ MeV. The calculation contains the terms $\chi(g^2/4\pi)$ which reduce to $(.04/\pi)\ \Gamma \arctan(\Delta m/\Gamma)$, thus for $\Delta m \simeq \Gamma$ the calculated cross section depends only weakly on the value of Γ assumed. Table X gives the calculated and observed ratios of "elastic" ρ production (i.e., production of a ρ° and an unexcited recoil nucleon) to "inelastic"

ρ production (where one or more pions are produced at the nucleon vertex). It is evident that this is not a significant contributor to the ρ production compared to the inelastic channels except in the lowest momentum transfer interval.

The ρ production data agree well with the calculation at low -t but fall below the unmodified calculation for larger -t as expected from form factors or absorption effects.[20] This departure is less when only the "inelastic" ρ production events are considered. As noted in Section II, off-mass-shell terms would modify the calculation, but not in a manner varying strongly with t. While the dipion angular distribution in this mass region is only $(2/3)\cos^2\theta$, the depolarization of ρ mesons due to absorption effects would give a departure from pure $\cos^2\theta$, and we interpret the data as consistent with ρ production dominating this mass region, although there is no quantitative formulation of the absorption model for inelastic ρ production as studied here. Thus, background (due to inelastic pion scattering, etc.) as well as s-wave dipion production are both less significant than ρ production. We cannot prove the lack of background quantitatively; qualitatively the data are everywhere consistent with small background. This is plausible, as discussed in Section II. Therefore, it is reasonable that our data, suitably restricted in t and M', should be freer of background than data taken at lower energies.

In a heavy liquid bubble chamber experiment exposed to negative pions of comparable energy, a relatively large A_1 meson production was reported and has been interpreted as resulting from a predominantly coherent peripheral process.[21] In our method of analysis, most of the ρ mesons from A_1 meson decay would have a momentum too low (e.g. corresponding to too large an apparent M' and -t) to be included in our data sample. Correspondingly, it is probable that relatively few of our events would appear as only three-prong events in a bubble chamber, considering the large M' values typifying our data. Therefore, we suspect that our results and theirs are mutually compatible, and that the total ρ meson production may in fact be close to the sum of the two processes.

The Missing Mass Spectra from ρ^0 Production

In Figs. 25 and 26 the missing mass spectrum data are plotted together with the theoretically computed curves. The curves are normalized to the data for M' > 1050 MeV. Much of this data has previously been discussed,[4] so we note here only the important results. The experimental resolution on missing mass is poor, not even cleanly separating the free nucleon recoils from N* recoils. In spite of this the trend suggests that the inelastic ρ production falls less rapidly than the elastic ρ production with momentum transfer. It also appears from the graphs that the lower isobars, specifically the N*(1238) are less prominent than the unmodified calculation would suggest. Off-mass-shell factors (Table I)

would increase the N*(1238) contribution somewhat relative to higher isobars. From the values in Table I and the M' spectra of Figs. 25 and 26, it is apparent that at larger -t values, the larger M' values are the major contributors to ρ production, and that thus the diagonal entries of Table I are the most relevant. Hence, if these factors are indeed appropriate, they should contribute about a factor of 2 corrections to the calculated cross sections over this range of t.

All of these factors, together with the ρ production magnitudes discussed above, lend support to the thesis that absorption processes at the nucleon vertex may lead to more highly excited isobar (or simply inelastic) pion-nucleon states (larger M') without necessarily subtracting from the ρ production integrated over the inelastic channels. To be sure, absorption processes at the meson vertex may still attenuate ρ production with increasing momentum transfer, and form factor effects may also play a role.

The $\pi^+\pi^-$ Interaction in the S-Wave State

In Table XI and Fig. 27, we present the ratio of the isotropic to the total dipion production, a_o/b_o of Tables VII and VIII. This ratio, Q, shows a consistent decrease from threshold to the ρ mass. The values of a_o from Tables VI and VII taken together with the weighted dipion mass spectra in 25 MeV intervals of Fig. 23 can be used to find the cross section for producing dipions in an s-wave. From Eq. 2, a corresponding theoretical calculation is available for the same process based on the same assumptions as the ρ

calculation of Eq. 4. The calculated s-wave cross section, modified by the ratio of the measured to calculated ρ production, could then be compared with the data to deduce a $\pi^+\pi^-$ cross section in the s-wave. Since the forward-backward asymmetry suggested that δ_0^0 was close to $(\pi/2)$ for $700 < m < 800$ MeV (see below), the total $\pi\pi$ cross section in this range would be only about 27/31 due to the ρ^0, and this ratio was also included in the normalization. Assuming that the J=0, T=2 phase shift is negligible,[22] these cross sections can be used to find an s-wave phase shift and scattering length for the J=T=0 state. The results are given in Table XII and Fig. 27.

It is at first apparent that there are no resonances below 600 MeV which would approach saturation of the s-wave unitarity limit with a width of over several MeV.[23] In view of the good statistics at low dipion masses, these data are particularly significant on this point. The s-wave scattering length extrapolates to about 1.1 fermi at threshold. It is also apparent that there are no zeroes in the s-wave pion-pion cross section or phase shift between threshold and 700 MeV.

These results could be in some error for several reasons. Near the ρ meson region the isotropic component may come in part from depolarized ρ's, and indeed this is probably the cause of the rise in the s-wave cross section above the unitarity limit near 650 MeV. Inelastic pion-nucleon scattering or production of other bosons (such as the

ω) would contribute to the apparent s-wave pion-pion interaction cross section; however, these processes would generally produce apparent pion pairs with larger momentum transfer, and dependent on incident momentum. That the cross sections of Table XII do not seem to depend particularly on either incident momentum or momentum transfer seems encouraging evidence that what we see is genuine pion-pion scattering. It is also apparent from Table XI that the low-mass dipions are largely isotropic, whereas inelastic scattering would tend to give a predominantly forward negative pion, with correspondingly larger values of a_1 and a_2 than are seen. It would be prudent, nevertheless, to regard our figures as upper limits to the s-wave pion-pion cross section for this reason. It is also not necessarily true that the s-wave production should be normalized to the ρ production in comparison between the data and the calculations. While the same nucleon off-mass-shell terms pertain in both cases, the low mass dipions production receives contributions from larger missing masses, M', at a given momentum transfer than the corresponding ρ production as seen in Figs. 6 and 7.

The entire ρ production data, but only the inelastic ρ production calculation, were compared for normalization; likewise the total s-wave data and only the inelastic s-wave calculation were used. This would introduce an error tending to cancel between the two mass regions as above.[24] Also absorption effects and effects due to other nucleons in a target carbon nucleus may be different in the two cases

since the ρ emerges as a discrete single particle while the s-wave scattered dipions at low mass emerge as two separate mesons. Again the restriction to small momentum transfers (less than 0.1 $(GeV/c)^2$) and lack of dependence of the interpretation on t within this interval increases our confidence that our interpretation is correct.

In Fig. 29 the missing mass spectra for the 280-400 MeV regions of dipion mass are presented. No detailed calculations of the spectra were made, but the qualitative nature of the data and the kinematic limits are sensible.

Forward-Backward Asymmetry

The coefficient a_1 represents the s-wave, p-wave mixing. A more direct measure of the cross term in the angular distributions is a "polarization" P where

$$P = (F - B)/(F + B);$$

F corresponds to $\theta < 90°$, and B to $\theta \geq 90°$. From the fitted coefficients we have also computed an equivalent P*, where

$$P^* = a_1/2b_o.$$

If our data have no bias with cos θ, P and P* would be equal. Using the raw data (un-weighted numbers of events sorted into the appropriate bins), P is plotted in Fig. 30 for $-t < 0.10$ $(GeV/c)^2$ and with the 12 and 18 GeV/c data taken together. The negative values of P below 500 MeV have not been observed in other experiments. This may be due to the better statistics here (well over 1000 events for m less

than 500 MeV and low -t) and to the high energy of the experiment with the consequent reduction of background effects (as inelastic pion scattering would contribute to positive values of a_1 and P). In order to explore the effect, the data below 450 MeV were combined as presented in Table XIII, where it is seen that the effect is consistent in all intervals, and represents a $2\frac{1}{2}$ standard deviation effect overall. Extensive tests were made to see if this effect was due to a bias in the geometry or the Cherenkov counter labeling. No such evidence was found, in fact the small biases that may exist seem to slightly favor a positive value of P. It is certainly possible that the effect is a statistical fluctuation; the $2\frac{1}{2}$ standard deviation effect of Table XIII is less significant when it is noted that the energy of the cut was made after plotting Fig. 30.

In Table XIV values of P* for each 100 MeV interval of dipion mass are given for the different cuts of momentum transfer. Again P* is negative generally in the lowest mass cut, although for $.05 < -t < .10$ $(GeV/c)^2$, P* is positive where P is negative. This is an entirely reasonable consequence of the fitting process. The consequent errors confirm our reliance on P (from the raw data) rather than P* (from the fits) for our interpretation. It is also consistent with the observation noted above that interpretations based on data subject to a minimum of manipulation are to be preferred.

Chew has suggested[25] that the s-wave T=0 phase shift may fall with increasing m, rather than rise. One consequence

of this behavior would be a negative P for low m, although P would be positive again near the ρ resonance with $\delta_0^0 = -90°$. As t increases P tends to become more positive as would be expected from a small contamination by inelastic π^- scattering. This suggests that even the lowest |t| cut may underestimate this effect, and that the mass at which P passes through zero is probably higher than the value given here. It is also plausible that this background could completely mask the effect in previous low-energy experiments. If P is negative, it would be due to either a negative value of δ_0^0 or of δ_1^1; however, at least at the ρ^0 mass δ_1^1 is known to be positive.[26] The δ_0^2 phase shift is known from bubble chamber data to be small and negative. If δ_0^0 is negative at low m, the δ_0^2 amplitude would add constructively to that from δ_0^0 in the reaction $\pi^+\pi^- \to \pi^+\pi^-$, while they would add destructively in $\pi^+\pi^- \to \pi^0\pi^0$. This is in qualitative agreement with a comparison between the present data and unpublished $\pi^0\pi^0$ data from the Oxford group.[27,28]

Plots of P* versus t in each mass interval averaged over the 12 and 18 GeV/c data are included in Fig. 31. Regrettably the statistics do not permit clear conclusions in each mass interval, so that only the ρ case discussed below and the predominantly negative P* for low m warrant discussion. However, these tables and graphs may serve to point out how improved data over the entire mass range could be used to determine the physical pion-pion interaction through extrapolation to the pole, in the manner originally urged by

Chew and Low.[29] In order to explore the extent to which δ_0^0 is resonant in the energy region $700 < m < 800$ MeV, the values of P* from Table XIV have been studied in this mass interval in particular. As noted for the low-mass data, background effects would generally modify P with increasing -t and off-mass-shell terms would reduce the ratio δ_0^0 / δ_0^1. The values of P* plotted in Fig. 31 were extrapolated to $t = \mu^2$. From Eq. 3a, P* = 0.58 for $\delta_0^0 = \delta_1^1$; $\delta_0^2 = 0$. Experimentally, P* = +0.525 at the pole corresponding to $\sin \delta_0^0 = \pm .92$ for $\delta_1^1 = 90°$, $\delta_0^2 = 0$. (The value of δ_0^2 is known to be about -20° in this mass range.[21]) These data are then consistent with δ_0^0 close to resonance, and the lower-energy data suggest $|\sin \delta_0^0|$ is growing slowly toward unity.

VIII. SUMMARY

A very high momentum experiment has been used to study the peripheral process and pion-pion interactions. The one-pion-exchange process qualitatively explains the ρ^0 production data. The missing mass spectra accompanying the ρ production corroborate this model, and the point is noted that inelastic channels at the nucleon vertex may account for some of the cross section which, in elastic ρ production, is attentuated by absorption processes. It is further observed that the inelastic cross section as calculated is almost independent of incident momentum and momentum transfer at high energies. A detailed study of the s-wave dipion interaction is carried out using the rich low dipion mass data herein. A monotonically falling $\pi\pi$ s-wave cross section is deduced, corresponding to a slowly varying phase shift which may pass near $\pm 90^\circ$ near the ρ mass. Negative forward-backward asymmetry for low dipion mass together with the cross section data are consistent with a negative J=T=0 phase shift falling smoothly from threshold. However, we see no evidence of a relatively narrow ϵ^0 resonance.

More generally, we have learned that an approach to the analysis wherein an integration over final states at one of two peripheral vertices permits detailed study of the other vertex can be successfully exploited. As detailed experiments are pressed to higher and higher energies, where

cross sections for each particular channel continue to fall, the methods of this experiment may find broad application.

IX. ACKNOWLEDGEMENTS

We would like to acknowledge the indispensable assistance in this experiment of W. Beck, H. Kuhn, L. Griffith, and C. Symons of CERN, and of E. Coleman, B. Loo, and S. Powell of The University of Michigan. A major part of the analysis was carried at The University of Michigan, including film measurement and digital calculation, supported by the U.S. Office of Naval Research Contract Nonr 1224(23). Film measurements at M.I.T. were supported by the U.S. Atomic Energy Commission. Valuable assistance in film prescanning was carried out at the University of Bologna under the direction of G. Giacomelli. We have benefited significantly from discussions on the theoretical interpretations of this data with R. Deck, C. Lovelace, and B. Svensson, and G. Chew. Finally, it is a pleasure to express our gratitude to CERN for its hospitality during the course of this experiment and its subsequent analysis.

REFERENCES

1. D.O. Caldwell, et al., Physics Letters 2, 253 (1962).
2. L.W. Jones, D. Harting, W. Middelkoop, B. Zacharov, D.O. Caldwell, E. Bleuler, and B. Elsner, The University of Michigan Technical Report No. 17 (unpublished); and in Ya. A. Smorodinsky, Proceedings of the XII International Conference on High Energy Physics, p. 457, Dubna 1964, published by atomizdat, Moscow (1966).
3. L.W. Jones, Phys. Rev. Letters 14, 186 (1965).
4. L.W. Jones, E. Bleuler, D.O. Caldwell, B. Elsner, D. Harting, W.C. Middelkoop, C.R. Symons, and B. Zacharov, CERN preprint 66/38/5/p/mm (unpublished; and Nuovo Cimento (to be published).
5. L.W. Jones, D.O. Caldwell, B. Zacharov, D. Harting, E. Bleuler, W.C. Middelkoop, and B. Elsner, University of Michigan Technical Report No. 22; and Physics Letters (to be published).
6. S.D. Drell, Phys. Rev. Letters 5, 342 (1960); Rev. Mod. Phys. 33, 458 (1961);
   F. Salzman, G. Salzman, Phys. Rev. 120, 599 (1960).
   We would like to thank R. Deck, S. Drell, and B.E.Y. Svensson for clarifying the application of these expressions to our problem.
7. J.D. Jackson, Nuovo Cimento 34, 1644 (1964).
8. F. Selleri, Phys. Letters 3, 76 (1962).

9. J.D. Jackson, J.T. Donohue, K. Gottfried, R. Keyser, and B.E.Y. Svensson, Phys. Rev. 139, B 428 (1965); J.D. Jackson, Rev. Modern Phys. 37, 484 (1965).

10. D.O. Caldwell and R. Weinstein, Nuovo Cimento 39, 991 (1965).

11. L. Durand and Y.T. Chiu, Phys. Rev. Letters 14, 1039 (1965).

12. L. Durand and Y.T. Chiu, Phys. Rev. Letters 14, 329 (1965); M. Feldman, W. Frati, J. Halpern, A. Kanofsky, M. Nussbaum, R. Richert, P. Yamin, A. Choudry, S. Devins, J. Grunhaus, Phys. Rev. Letters 14, 869 (1965); and I. Derado, V.P. Kenney, J.A. Poirer, and W.D. Shephard, Phys. Rev. Letters 14, 872 (1965);

13. V. Hagopean, W. Selove, J. Aletti, J.P. Baton, M. Neveu-Rene, R. Gessarolli, and A. Romano, Phys. Rev. Letters 14, 1077 (1965); Rosenfeld, Oxford International Conference on Elementary Particles, Proceedings (Supplement) p.5, (1965), Rutherford High Energy Laboratory, Berks. England (1966).

14. E. Bleuler, D.O. Caldwell, B. Elsner, D. Harting, L.W. Jones, W.C. Middelkoop, B. Zacharov, M.L. Perl, and C.C. Ting, Nucl. Instr. and Methods 20, 208 (1963).

15. D. Harting, P. Blackall, B. Elsner, A.C. Helmholz, W.C. Middelkoop, B. Powell, B. Zacharov, P. Zanella, P. Dalpiaz, M.N. Focacci, S. Focardi, G. Giacomelli, L. Monari, J.A. Beaney, P.A. Donald, P. Mason, L.W. Jones, and D.O. Caldwell, Nuovo Cimento 38, 60 (1965);

D. Harting, "An Experiment on Pion-Proton and Proton-Proton Elastic Scattering at 8.5, 12.4, and 18.4 GeV/c" (thesis) University of Amsterdam (1964).

16. B. Zacharov, (to be published).

17. B. Zacharov, Nuclear Instr. and Methods 32, 163 (1965).

18. B. Zacharov, Nuclear Instr. and Methods 33, 136 (1965).

19. S.B. Trieman and C.N. Yang, Phys. Rev. Letters 8, 140 (1962).

20. These results differ, especially for larger -t, from the preliminary results reported earlier (references 2,3) for three reasons: first, the number of events was doubled over the earlier data sample; second, the fitting and weighting procedures were considerably refined; and third, an error in the calculation of the angle variables in the dipion c.m. system was located and corrected.

21. J.F. Allurd, D. Drijard, J. Hennessy, R. Huson, A. Lloret, J. Six, J.J. Veillet, G. Bellini, M. DiCorato, E. Firoini, P. Negri, M. Rollier, J. Crossard, J. Ginestet, A.H. Tran, H.H. Bingham, R. Diebold, W.B. Fretter, H.J. Lubatti, W. Michael, and K. Moriyasu, Phys. Rev. Letters 19, 431 (1965).

22. From $\pi^+ p \rightarrow \pi^+ \pi^+ n$ and $\pi^- p \rightarrow \pi^- \pi^- N^{*++}$ bubble chamber data, $\sigma_{\pi\pi}(T=2)$ falls from 14 mb near threshold to 4 mb near the ρ mass corresponding to δ_0^2 rising from 5.5° to 20° in the same interval.

23. L.M. Brown and P. Singer, Phys. Rev. Letters 8, 460 (1962); L.M. Brown and P. Singer, Phys. Rev. 133, B 812 (1964).

24. Note that in the lowest momentum transfer interval, the elastic ρ production is a 20% contribution to our data but the larger range of M' permitted in this same t-interval results in a much smaller elastic contribution to the data for m < 450 MeV (Fig. 29). As a result, our computed $\sigma_{\pi\pi}$ is probably low by about 20% for $-t < 0.05$ $(GeV/c)^2$ for the lowest dipion masses and by an amount which decreases as m increases toward the ρ mass. This trend may be seen in Table XII where the lower $|t|$ cross section values are consistently low at low m.

25. G.F. Chew, Phys. Rev. Letters, 16, 60 (1966).

26. C. Lovelace has pointed out that one possible source of a zero in δ^1 could be the interpretation of the ρ meson as a Castellejo-Dalitz-Dyson pole (private communication).

27. I.F. Corbett, C.J.S. Damerell, N. Middlemass, D. Newton, A.B. Clegg, and W.S.C. Williams, Rutherford Laboratory preprint RPP/H/7 (1965) and A.B. Clegg, private communication.

28. The existing Ke_4 data suggest a positive δ_0^0 near threshold (Birge, Ely, Gidal, Kalmus, Kerman, Powell, Camerini, Cline, Fry, Gaidos, Murphree, and Murphy, Phys. Rev. 139, B1600 (1965) and C.T. Murphy, private communication). Recently L.D. Jacobs and W. Selove (Phys. Rev. Letters 16, 669 (1966)) have analyzed $\pi^-\pi^+$ production in bubble chamber data and have also concluded

that δ_0^0 is positive, although the conclusions are based on an order of magnitude, fewer events, larger momentum transfers, and lower energies than this study.

28. G.F. Chew and F.E. Low, Phys. Rev. 113, 1640 (1959).

TABLE I.

Factors of f(M') to be applied to Eqs. (2) - (5) to account for the spin of the final-state nucleon system, M'.

$-t$ $(GeV/c)^2$	M'(GeV) J^P	1.24 $(3/2)^+$	1.51 $(3/2)^-$	1.68 $(5/2)^-$
0		1.28	1.14	1.12
0.05		2.06	1.52	1.45
0.10		2.87	1.98	1.85
0.15		3.70	2.44	2.32
0.20		4.55	3.08	2.85

TABLE II.

One-pion exchange calculation of elastic and inelastic ρ^0 production. The elastic cross-sections are given with and without the Selleri form factor. The calculations used $\chi = 1$, $m_0 = 750$ MeV, and $\Gamma_0 = 100$ MeV. The entries are cross-sections in microbarns (10^{-30} cm^2).

Elastic ρ^0 production cross-section Eq. (6)												
p(GeV/c)	4		8		12		18		50		200	
$\|t\|$ (GeV/c)^2	a	b	a	b	a	b	a	b	a	b	a	b
<0.05	213	124	53	31	24	13.8	10.5	6.1	1.36	0.80	0.085	0.050
0.05-0.10	192	78	48	19	21	8.7	9.5	3.8	1.23	0.50	0.077	0.031
0.10-0.20	303	87	76	22	34	9.7	15.0	4.3	1.94	0.56	0.121	0.035
0.20-0.30	261	56	65	14	29	6.2	12.9	2.8	1.67	0.36	0.104	0.022
<0.30	975	350	244	88	108	38.9	48.1	17.3	6.24	2.24	0.390	0.140
0.30-1.0	1766	245	441	61	196	27.2	87.2	12.1	11.30	1.57	0.706	0.098

a: Eq. (6) b: Eq. (6) multiplied by $F^2(t)$ of Eq. (7)

Inelastic ρ^0 production cross-section Eq. (5) ;						
p(GeV/c)	4	8	12	18	50	200
$\|t\|$ (GeV/c)^2						
<0.05	7.6	57	58	57	50	40
0.05-0.10	142	127	122	115	94	77
0.10-0.20	340	305	281	258	213	187
0.20-0.30	358	319	292	267	224	205
<0.30	848	809	753	696	580	509

TABLE III.

Decay mean-free path λ of a ρ meson (Γ = 100 MeV) in the recoil nucleon c.m. for different incident pion momenta. The final state is considered a nucleon (M' = M) or a state of M' = 1.5 GeV.

p(GeV/c)	M' = M λ(fermis)	M' = 1.5 GeV λ(fermis)
2	4.6	
4	9.9	
8	20.6	
12	31	18.6
18	47	29

TABLE IV.

Yield of dibosons from the target and from the dE/dx counters used to find the dependence of diboson yield on atomic weight for carbon. Events from the target are only those with $-t < 0.30$ $(GeV/c)^2$ and $M' < 2200$ MeV (12 GeV/c) or $M' < 2500$ MeV (18 GeV/c).

P	Target	Dibosons from dE/dx Counters	Dibosons from Target	
			m<650 MeV	650<m<850 MeV
18 GeV/c	CH_2	544	589	358
	C	97	144	93
12 GeV/c	CH_2	891	979	707
	C	29	54	31

TABLE V.

A. Percentages of dibosons with different Cherenkov counter signatures for the 12 GeV/c data, 18 GeV/c data, and for the total.

	Neither Boson Through a Counter	One of Two Bosons Through a Counter	Both Bosons Through Both Counters
12 GeV/c	24.3%	57.5%	18.2%
18 GeV/c	35.8%	39.9%	24.3%
12 & 18 GeV/c	29.4%	49.6%	21.0%

B. Percentages of bosons passing through each Cherenkov counter, labelled as pions.

	Counter #1	Counter #2	Average of #1 & #2	% Labelled as Kaons
12 GeV/c	69.6%	79.6%	74.2%	25.8%
18 GeV/c	85.6%	78.0%	81.9%	18.1%
12 & 18 GeV/c	76.2%	79.0%	77.5%	22.5%

C. Percentage of dibosons, where each boson passed through a Cherenkov counter, labelled as dipions.

	Dipions	Dikaons and Kaon-Pion Pairs
12 GeV/c	52.9%	47.1%
18 GeV/c	72.3%	27.7%
12 & 18 GeV/c	63.0%	37.0%

TABLE V. (cont'd.)

D. Percentage of events "incorrectly" assumed dipions (assuming 100% Cherenkov counter efficiency; pion/kaon ratio the same for bosons and dibosons missing counters as those detected). Data from A, B, and C above.

	One Boson Labelled; Kaons Missed	Neither Boson Labelled; Dikaons and Kaon-Pions Missed	Total Overestimate of Dipions
12 GeV/c	57.5%x0.258=14.8%	24.3%x0.471=11.5%	26.3%
18 GeV/c	39.9%x0.181= 7.2%	35.8%x0.277= 9.9%	17.1%
12 & 18 GeV/c	49.6%x0.225=11.2%	29.4%x0.370=10.9%	22.1%

E. Percentage of all events not labelled as probable dipions.

12 GeV/c	17.5%
18 GeV/c	12.5%
12 & 18 GeV/c	15.3%

TABLE VI.

Breit-Wigner resonance fits to dipions in range 600 < m < 900 MeV. Fit made to the weighted data using a Breit-Wigner resonance plus a linearly-varying background.

	$\lvert t \rvert$ Range $(GeV/c)^2$	m_o (MeV)	Γ_o (MeV)	χ^2 per Degree of Freedom
p = 12 GeV/c *	< .05	765 ± 6	129 ± 19	1.30
M' < 2500 MeV	.10 - .20	749 ± 5	157 ± 16	0.58
	.20 - .30	750 ± 8	102 ± 25	0.94
p = 18 GeV/c	< .05	745 ± 13	169 ± 41	0.68
M' < 3000 MeV	.05 - .10	760 ± 9	175 ± 30	1.25
	.10 - .20	761 ± 6	157 ± 19	0.63
	.20 - .30	780 ± 10	157 ± 31	0.72

* Due to a computer error the values for 12 GeV/c, .05 < $\lvert t \rvert$ < .10 were lost.

TABLE VII.

Fits of the weighted 12 GeV/c data, in 100 MeV dipion mass intervals, to $f(\theta) = a_o + a_1 \cos\theta + a_2 \cos^2\theta$; $b_o = a_o + \frac{1}{3} a_2$. The cross section in each interval is found from b_o and the normalization of Section V. The errors are statistical only.

Four Momentum Transfer $\|t\|$ $(GeV/c)^2$	Dipion Mass (MeV)	a_o	a_1	a_2	b_o	σ (μb)
< .05	300-400	57 ± 10	-24 ± 15	49 ± 28	73 ± 7	7.73 ± .83
	400-500	99 ± 16	- 6 ± 23	-8 ± 43	96 ± 12	10.2 ± 1.3
	500-600	66 ± 14	45 ± 27	74 ± 46	91 ± 13	9.5 ± 1.4
	600-700	108 ± 20	-15 ± 35	2 ± 67	109 ± 17	11.5 ± 1.8
	700-800	122 ± 31	296 ± 85	672 ± 184	347 ± 51	36.4 ± 5.4
	800-900	35 ± 19	237 ± 102	811 ± 561	306 ± 176	32.1 ± 18.5
.05 - .10	300-400	-17 ± 15	- 7 ± 16	134 ± 39	27 ± 7	2.9 ± 0.8
	400-500	52 ± 22	-30 ± 26	100 ± 53	86 ± 14	9.1 ± 1.5
	500-600	41 ± 16	34 ± 35	212 ± 65	112 ± 18	11.8 ± 1.9
	600-700	74 ± 23	106 ± 45	273 ± 90	165 ± 24	17.4 ± 2.5
	700-800	203 ± 42	351 ± 117	797 ± 242	469 ± 69	49.3 ± 7.3
	800-900	40 ± 21	207 ± 135	1401 ± 477	508 ± 151	53.3 ± 15.9
.10 - .20	300-400	-18 ± 47	0.9 ± 19	150 ± 74	31 ± 24	3.3 ± 2.6
	400-500	468 ± 533	-17 ± 59	-227 ± 634	392 ± 324	41.2 ± 34.1
	500-600	415 ± 243	19 ± 66	-202 ± 332	347 ± 137	36.5 ± 14.4
	600-700	126 ± 32	372 ± 98	904 ± 165	428 ± 52	45.0 ± 5.5
	700-800	132 ± 46	410 ± 164	2320 ± 429	905 ± 125	95.1 ± 13.2
	800-900	137 ± 48	123 ± 211	685 ± 821	365 ± 246	38.4 ± 25.8

TABLE VIII.

Fits of the weighted 18 GeV/c data, in 100 MeV dipion mass intervals, to $f(\theta) = a_o + a_1 \cos\theta + a_2 \cos^2\theta$; $b_o = a_o + \frac{1}{3} a_2$. The cross section in each interval is found from b_o and the normalization of Section V. The errors are statistical only.

Four Momentum transfer $-t$ $(GeV/c)^2$	Dipion Mass (MeV)	a_o	a_1	a_2	b_o	σ (μb)
.05	300-400	21.3±3.0	-1.7±5.9	9.2±11.5	24.4±3.1	14.1±1.7
	400-500	21.5±4.6	6.1±9.0	10.5±16.9	25.1±4.5	14.5±2.6
	500-600	11.0±4.5	12.2±10.3	50.7±24.8	27.9±6.4	16.1±3.7
	600-700	16.0±5.1	37.6±15.9	80.8±31.0	42.9±8.9	24.8±5.1
	700-800	17.7±7.0	69.0±23.6	159.8±46.3	71.0±14.4	41.0±8.3
	800-900	-	-	-	-	-
.05 - .10	300-400	7.9±2.3	4.2±4.7	17.6±7.4	13.8±2.2	8.0±1.3
	400-500	15.3±6.1	8.2±9.0	34.8±18.5	26.9±4.6	15.5±2.6
	500-600	24.0±7.0	13.6±12.7	30.8±21.9	34.2±6.4	19.8±3.7
	600-700	21.8±7.7	-0.7±17.9	72.1±30.4	45.9±8.9	26.5±5.1
	700-800	44.7±11.7	87.9±32.6	203.2±61.5	112.5±18.3	65.0±10.6
	800-900	26.4±11.7	4.7±23.7	77.4±48.6	52.2±12.1	30.1±7.0
.10 - .20	300-400	54.6±17.7	-6.9±7.4	-42.8±25.2	40.3±10.0	23.3±5.8
	400-500	32.5±31.6	11.8±9.0	- 9.7±46.2	29.3±17.0	16.9±9.8
	500-600	27.9±16.1	0.6±12.8	13.3±31.5	32.4±9.0	18.7±5.3
	600-700	39.0±14.6	79.3±24.9	119.2±40.8	78.8±13.2	45.5±7.6
	700-800	35.5±14.7	99.5±40.5	489.5±83.6	198.6±23.8	114.8±13.7
	800-900	31.4±15.5	47.3±29.3	154.2±70.8	82.8±17.3	47.8±10.1
.20 - .30	300-400	21.0±10.1	-1.6±5.5	-13.6±15.1	16.4±5.8	9.5±3.3
	400-500	171.6±90.8	6.8±16.8	-179.3±115.2	111.8±53.1	64.6±30.7
	500-600	41.8±75.3	5.5±16.9	128.3±104.8	1.0±41.4	0.6±24.0
	600-700	0.6±72.4	5.0±24.2	111.9±103.0	37.9±40.5	21.9±23.4
	700-800	-10.1±67.9	65.2±30.7	231.9±115.1	67.2±34.3	38.8±19.8
	800-900	46.7±16.9	-58.5±36.7	65.3±49.6	68.4±18.4	39.5±10.6

TABLE IX.

Comparison between normalized experimental cross sections for inelastic ρ^o production and the one-pion-exchange calculation of Eq. (5) over the dipion mass interval $700 \leq m < 800$ MeV. For the calculation, the ρ^o is characterized by $m_o = 750$ MeV, $\Gamma = 100$ MeV.

	Four-Momentum Transfer $-t(GeV/c)^2$	$\sigma_{\mu b}$ Calculation Eq. (5)	$\sigma_{\mu b}$ (a) Experiment	$\sigma_{\mu b}$ (b) Experiment Corrected for Elastic Production
p = 12GeV/c	< .05	42	36.4 ± 5.4	28
M' <2500MeV	.05 - .10	89	49.3 ± 7.3	47
	.10 - .20	201	95.1 ± 13.2	94
p = 18GeV/c				
M' <3000MeV	< .05	42	41.1 ± 8.3	35
	.05 - .10	89	65.1 ± 10.6	64
	.10 - .20	184	114.8 ± 13.7	115
	.20 - .30	131	38.8 ± 19.8	39

(a) The errors are statistical. There is an additional normalization uncertainty of +20%, - 38%.

(b) The ratio of elastic to inelastic ρ^o production as deduced from the missing mass spectra as given in Table X was used to correct the experimental values as given here in Tables VII and VIII.

TABLE X.

Comparison of elastic to inelastic ρ^0 production. Define elastic ρ production as that where a single neutron recoils, $M' < 1050$ MeV; inelastic ρ production as that where an excited nucleon system, $M' > 1050$ recoils. The calculation compares the elastic cross sections with a form factor applied (columns b, Table II) to the inelastic cross section with no form factor. $M'_{max} = 2500$ MeV (12 GeV/c data) and 3000 MeV (18 GeV/c data).

Incident Pion Momentum p(GeV/c)	Four-Momentum Transfer $-t$ $(GeV/c)^2$	Elastic Events Observed N_e $500 < M' < 1050$ MeV	Inelastic Events Observed N_I $1050 < M' < M'_{max}$	Elastic to Inelastic Ratio Observed N_e/N_I	Elastic to Inelastic Ratio Calculated (from Table 1)* N_e/N_I
12	<0.05	50	222	0.225	0.159
	0.05-0.10	19	368	0.052	0.048
	0.10-0.20	4	459	0.009	0.023
	0.20-0.30	1	195	0.005	0.014
18	<0.05	14	101	0.139	0.072
	0.05-0.10	3	188	0.016	0.022
	0.10-0.20	1	279	0.004	0.011
	0.20-0.30	0	103	-	0.007

* The theoretical ratios are 2/3 the ratios of the cross sections of Table II as the target contains only 2/3 (effective) protons.

TABLE XI.

The ratio, Q, of isotropic to total dipion production in 100 MeV dipion mass intervals. The weighted data were fit by $f(\theta) = a_o + a_1 \cos\theta + a_2 \cos^2\theta$; $b_o = a_o + \frac{1}{3} a_2$; and $Q = a_o/b_o$.

Incident Pion Momentum (GeV/c)	Interval of Dipion Mass (MeV)	Intervals of Four-Momentum Transfer $-t$ $(GeV/c)^2$		
		< .05	.05 - .10	.10 - .20
12	300 - 400	.78 ±.16	.62 ±.58	-.58 ±1.56
	400 - 500	1.03 ±.22	.61 ±.28	1.19 ±1.68
	500 - 600	.73 ±.19	.37 ±.16	1.19 ± .84
	600 - 700	1.00 ±.25	.45 ±.16	.30 ± .08
	700 - 800	.35 ±.10	.43 ±.11	.15 ± .05
	800 - 900	.12 ±.09	.08 ±.05	.37 ± .28
18	300 - 400	.87 ±.17	.57 ±.19	1.35 ± .56
	400 - 500	.86 ±.24	.57 ±.25	1.11 ±1.26
	500 - 600	.40 ±.19	.70 ±.24	.86 ± .55
	600 - 700	.37 ±.16	.48 ±.19	.50 ± .20
	700 - 800	.25 ±.11	.40 ±.12	.18 ± .08
	800 - 900		.51 ±.25	.38 ± .20
12 & 18 Averaged	300 - 400	.82 ±.12	.58 ±.18	1.14 ± .52
	400 - 500	.95 ±.16	.59 ±.18	1.14 ±1.01
	500 - 600	.55 ±.13	.47 ±.13	1.22 ± .52
	600 - 700	.55 ±.13	.46 ±.12	.32 ± .08
	700 - 800	.30 ±.08	.42 ±.08	.16 ± .04
	800 - 900	.12 ±.09	.10 ±.05	.38 ± .17

TABLE XII.

The s-wave cross section for $\pi^+ + \pi^- \rightarrow \pi^+ + \pi^-$, phase shift, and scattering length as deduced from peripheral $\pi^- + N \rightarrow \pi^- + \pi^+ + (N + n\pi)$ reactions.

	$\sigma_{\pi\pi}(s)$ in millibarns							
Dipion Mass m (MeV)	$\lvert t\rvert < .05 (GeV/c)^2$			$.05 < \lvert t\rvert < .10$ $(GeV/c)^2$		Average $\sigma_{\pi\pi}(s)$	Phase Shift δ_o° [a]	Scattering Length A_o° (fermis) [a,b]	Number of Events
	p	12 GeV/c	18 GeV/c	12 GeV/c	18 GeV/c				
280		26.8	21.0	37.3	57.1	35.6			123
300		23.5	53.2	47.6	73.0	49.4	20°	1.12	262
325		25.0	55.7	39.4	52.2	43.1	25°	1.17	212
350		26.0	46.9	42.1	39.4	38.6	29°	1.23	173
375		27.4	44.3	30.5	34.4	34.2	32°	1.28	141
400		36.2	37.9	29.2	40.2	35.9	38°	1.51	136
425		36.1	34.6	31.4	40.0	35.6	43°	1.71	128
450		29.7	34.7	20.4	27.3	28.1	42°	1.57	97
475		25.5	27.5	23.7	31.1	27.0	44°	1.68	103
500		27.1	19.9	16.9	41.1	26.3	48°	1.89	109
525		12.5	17.1	18.8	38.5	21.8	47°	1.75	93
550		21.9	20.3	13.1	35.3	22.7	52°	2.10	95
575		27.2	11.9	10.2	38.5	22.0	55°	2.34	82
600		30.5	8.5	18.5	25.2	20.7	57°	2.44	88
625		39.0	26.9	23.0	34.4	30.9			98
650		46.5	28.2	28.5	34.5	34.5			119
675		34.4	20.4	24.6	28.9	27.1			92
700									
No. of Events		799	510	473	369			Total No. of Events	2151

b. $(A_o^\circ)^{-1} = k \left(\frac{k^2}{\mu^2} + 1 \right)^{-\frac{1}{2}} \cot \delta_o^\circ$

a. Assuming $\delta_o^2 = 0$

TABLE XIII.

Forward-backward asymmetry, P, for dipions of mass below 450 MeV. $P = (F - B)/(F + B)$ where F is the number of events corresponding to a π^- scattering angle in the dipion c.m.s., $\theta < 90°$, and B is the number for $\theta > 90°$.

Incident Pion Momentum (GeV/c)	Upper Limit of Missing Mass M' MeV	Range of Four-Momentum Transfer $t(GeV/c)^2$	P (%)	Number of Events
12	2500	<0.05	-7.50 ± 4.60	467
		0.05 - 0.10	-3.96 ± 7.62	177
18	3000	<0.05	-8.46 ± 5.38	343
		0.05 - 0.10	-3.71 ± 7.26	189
12 & 18	As Above	<0.10	-6.64 ± 2.91	1176

TABLE XIV.

The forward-backward asymmetry, P*, in 100 MeV dipion mass intervals. The weighted data were fit by

$$f(\theta) = a_o + a_1 \cos\theta + a_2 \cos^2\theta;\ b_o = a_o + \tfrac{1}{3} a_2;$$

and the asymmetry parameter $P^* = a_1/2b_o$.

Incident Pion Momentum (GeV/c)	Interval of Dipion Mass (MeV)	Intervals of Four-Momentum Transfer $-t$ $(GeV/c)^2$		
		<.05	.05 - .10	.10 - .20
12	300 - 400	-.16 ±.11	-.13 ±.29	.01 ±.31
	400 - 500	.03 ±.12	-.18 ±.15	-.02 ±.08
	500 - 600	.25 ±.16	.15 ±.16	.03 ±.10
	600 - 700	-.13 ±.30	.32 ±.14	.44 ±.13
	700 - 800	.43 ±.14	.37 ±.14	.23 ±.10
	800 - 900	.39 ±.28	.21 ±.15	.17 ±.31
18	300 - 400	-.06 ±.21	.15 ±.17	-.09 ±.09
	400 - 500	.12 ±.18	.15 ±.22	.20 ±.20
	500 - 600	.22 ±.19	.20 ±.19	.01 ±.20
	600 - 700	.44 ±.20	-.01 ±.19	.50 ±.18
	700 - 800	.49 ±.19	.39 ±.16	.25 ±.11
	800 - 900		.05 ±10.28	.29 ±2.15
12 & 18 Averaged	300 - 400	-.12 ±.09	.08 ±.15	-.08 ±.09
	400 - 500	.02 ±.10	-.07 ±.13	.01 ±.07
	500 - 600	.24 ±.12	.17 ±.12	.02 ±.09
	600 - 700	.26 ±.17	.21 ±.12	.46 ±.10
	700 - 800	.45 ±.11	.38 ±.10	.24 ±.07
	800 - 900	.39 ±.28	.20 ±.15	.17 ±.31

FIGURE CAPTIONS

Figure 1. Feynman diagrams appropriate for the peripheral reactions discussed here: (a) Elastic meson scattering at the meson vertex, single nucleon recoil; (b) production of a meson resonance, single nucleon recoil (e.g., "elastic" ρ meson production); (c) elastic meson scattering at meson vertex, recoil of an excited nucleon system; and (d) production of a meson resonance, recoil of an excited nucleon system (e.g., "inelastic" ρ meson production).

Figure 2. The kinematic limits on missing mass, M', versus four-momentum transfer, t, for the process $\pi^- N \rightarrow \rho^\circ N^*$, where the state N* has total energy M'. Curves for incident pion momenta of 4, 8, 12, and 18 GeV/c are presented.

Figure 3. The kinematic limits presented in Fig. 2 expanded for the region of M', t of interest for this experiment. The limit for incident momentum of 100 GeV/c is also given in addition to those of 4 - 18 GeV/c. The regions used in the analysis are bounded by the dotted lines.

Figure 4. The difference between incident pion momentum, p, and the outgoing dipion momentum, p_3, versus recoil nucleon mass M' for $-t = 0.05$ $(\text{GeV/c})^2$. The expression is approximately valid for $p \gg M'$; $p_3 = p$, and for dipion mass $m < M, M'$. The dependence on t is not strong, and the graph for $-t = 0.20$ is very close to the curve given here.

Figure 5. The ratio of the weighted dipion events with $M' \geq 2500$ MeV to those with $M' < 2500$ MeV versus dipion mass, m. The broad peak about 500 MeV is interpreted as due to the two charged pions from ω production.

Figure 6. The kinematic limits on missing mass, M', versus dipion mass, m, for different values of four-momentum transfer, t, and for 12 GeV/c incident momentum.

Figure 7. The kinematic limits on missing mass, M', versus dipion mass, m, for different values of four-momentum transfer, t, and for 18 GeV/c incident momentum.

Figure 8. A plan view of the geometry of the experiment, showing the relative locations of magnets, target, spark chambers, and counters. The spark chambers are numbered 1 through 8.

Figure 9. Photograph of the terminal portion of the apparatus. From lower left to upper right the magnet, spark chambers 7 and 8, the trigger scintillation counters, and the gas Cherenkov counters may be seen. Plastic field lenses and mirror supports are apparent above the chambers.

Figure 10. The z-vertex distribution of ρ mesons produced by 12 and 18 GeV/c incident pions. The geometrical extent of the target and the dE/dx scintillation counters is shown. There was an anticoincidence counter with an aperture for the incident beam a few centimeters to the left of the target.

Figure 11. Design of the gas threshold Cherenkov counters. The counters were always at the ambiant atmospheric pressure, and operated with F 22 and F 114.

Figure 12. The dipion mass spectrum of events with apparent vertices between the target and dE/dx counters showing a peak at the K° mass. This confirms the mass resolution and normalization as computed.

Figure 13. A film frame of a typical dipion event. The spark chambers are bordered by fiducial lights.

Figure 14. A sketch of the film frame format showing the views of each spark chamber numbered as in Fig. 8. The lower member of each view pair is the direct (vertical) view; the upper member, specified s, is the stereo (horizontal) view.

Figure 15. Calculation of detection probability for fixed Treiman-Yang angle, φ. The direction of each particle is represented by a point. B: beam particle, D: dipion, N: negative pion, P: positive pion. //// allowed regions for P. \\\\ allowed region for N. XXXX allowed regions for both P and N, with fixed $\Delta\varphi$. The detection probability due to the pair of allowed regions for f_P and f_N shown is $P = (14.3^{\circ} + 7.0^{\circ})/180^{\circ} = 0.118$.

Figure 16. Unweighted dipion mass spectra for 12 and 18 GeV/c incident momenta in the four different intervals of four-momentum transfer, t. The ordinates are numbers of events in each 10 MeV dipion mass interval. Missing mass cuts have been imposed as indicated.

Figure 17. Unweighted dipion mass spectrum as in Fig. 16 with all 12 GeV/c data taken together. Also shown is the 12 GeV/c mass spectrum of all events without restriction in missing mass or momentum transfer.

Figure 18. Unweighted dipion mass spectrum as in Fig. 16 with all 18 GeV/c data taken together. Also shown is the 18 GeV/c mass spectrum of all events without restriction in missing mass or momentum transfer.

Figure 19. Unweighted dipion mass spectrum for those events between 600 and 900 MeV, $|\cos\theta| < 0.3$, and four-momentum transfer $|t| < 0.1$ $(\text{GeV/c})^2$. This selection was made to seek evidence of an s-wave dipion resonance in the presence of the dominent ρ°.

Figure 20. Unweighted dipion mass spectrum for all events between 600 and 900 MeV with no restriction on cos θ or t other than $|t| < 0.3$ $(\text{GeV/c})^2$ and limits on missing mass M' as in Fig. 16.

Figure 21. Dipion mass spectra of Fig. 16 weighted according to the average detection probability as a function of dipion mass in each momentum transfer interval. No account was taken here of the dependence of detection probability on cos θ nor of the varying cos θ distributions with dipion mass. The ordinate scale is in arbitrary units.

Figure 22. The dipion mass spectra of Fig. 21 summed over the four intervals of momentum transfer for each incident momentum separately and together. Combining the data from 12 and 18 GeV/c involves a rather arbitrary relative normalization. The ordinate scale is in arbitrary units.

Figure 23. Dipion mass spectra of Fig. 16 and Fig. 21 weighted including effects of the cos θ dependence of detection probability. The actual weighting procedure is described in the text. The ordinates scale is in arbitrary units.

Figure 24. The dipion mass spectra of Fig. 23 summed over the four intervals of momentum transfer for each incident momentum separately and together. Combining the data from 12 and 18 GeV/c involves a rather arbitrary relative normalization. The ordinate scale is in arbitrary units. These histograms differ from Fig. 22 in that the cos θ dependence of detection probability and dipion production has been included.

Figure 25. The experimental distributions of missing mass, M', for ρ° production by 12 GeV/c incident pions. The data are divided into the intervals of four-momentum transfer of Fig. 16. The calculated spectra, normalized in area to the events with M' > 1050 MeV, are superimposed as smooth curves. This data sample contains 1319 events. The ordinates are numbers of events in each 50 MeV interval of M'.

Figure 26. The experimental distributions of missing mass, M', for ρ^0 production by 18 GeV/c incident pions. The data are divided into the intervals of four-momentum transfer of Fig. 16. The calculated spectra, normalized in area to the events with M' > 1050 MeV, are superimposed as smooth curves. This data sample contains 693 events. The ordinates are numbers of events in each 50 MeV interval of M'.

Figure 27. The ratio, Q, of the isotropic to the total dipion production versus momentum transfer for each 100 MeV interval of dipion mass as tabulated in Table X. Data from 12 and 18 GeV/c have been combined statistically. The data were fit to $f(\theta) = a_o + a_1 \cos\theta + a_2 \cos^2\theta$; $b_o = a_o + (1/3)\, a_2$; and $Q = a_o/b_o$.

Figure 28. The total cross section for the process $\pi^+\pi^- \rightarrow \pi^+\pi^-$ in the s-wave channel versus dipion mass as deduced from $\pi^- + N \rightarrow \pi^+ + \pi^- + (N + n\pi)$ for incident pions of 12 and 18 GeV/c and for two intervals of momentum transfer, $-t < 0.05$ $(GeV/c)^2$ and $0.05 < -t < 0.10$ $(GeV/c)^2$. The solid histogram is the average of the four data subsets; dashed histograms represent the average over both incident pion momenta in each momentum transfer interval, and extreme values from the four data samples in each 25 MeV mass interval are indicated by x's. The unitarity limit for J=T=0 scattering, $(4/9)4\pi\lambda^2$, is also indicated.

Figure 29. The experimental distributions of missing mass, M', for production of low-mass dipions ($m < 400$ MeV) for the different intervals of incident momentum and momentum transfer. The ordinates are numbers of events per 50 MeV.

Figure 30. The forward-backward asymmetry, $P = (F - B)/(F + B)$ versus dipion mass for all data with $-t < 0.10$ $(GeV/c)^2$. F is the unweighted number of events where the π^- scattering angle in the dipion c.m.s., $\theta < 90°$; and correspondingly, B is the unweighted number of events where $\theta > 90°$.

Figure 31. The forward-backward asymmetry, P*, as deduced from cos θ expansions of the weighted data versus four-momentum transfer in 100 MeV intervals of dipion mass taken from Table XIII. Data from 12 and 18 GeV/c have been combined statistically. The data were fit to $f(\theta) = a_o + a_1 \cos\theta + a_2 \cos^2\theta$; $b_o = a_o + (1/3)\, a_2$; and $P^* = a_1/2b_o$.

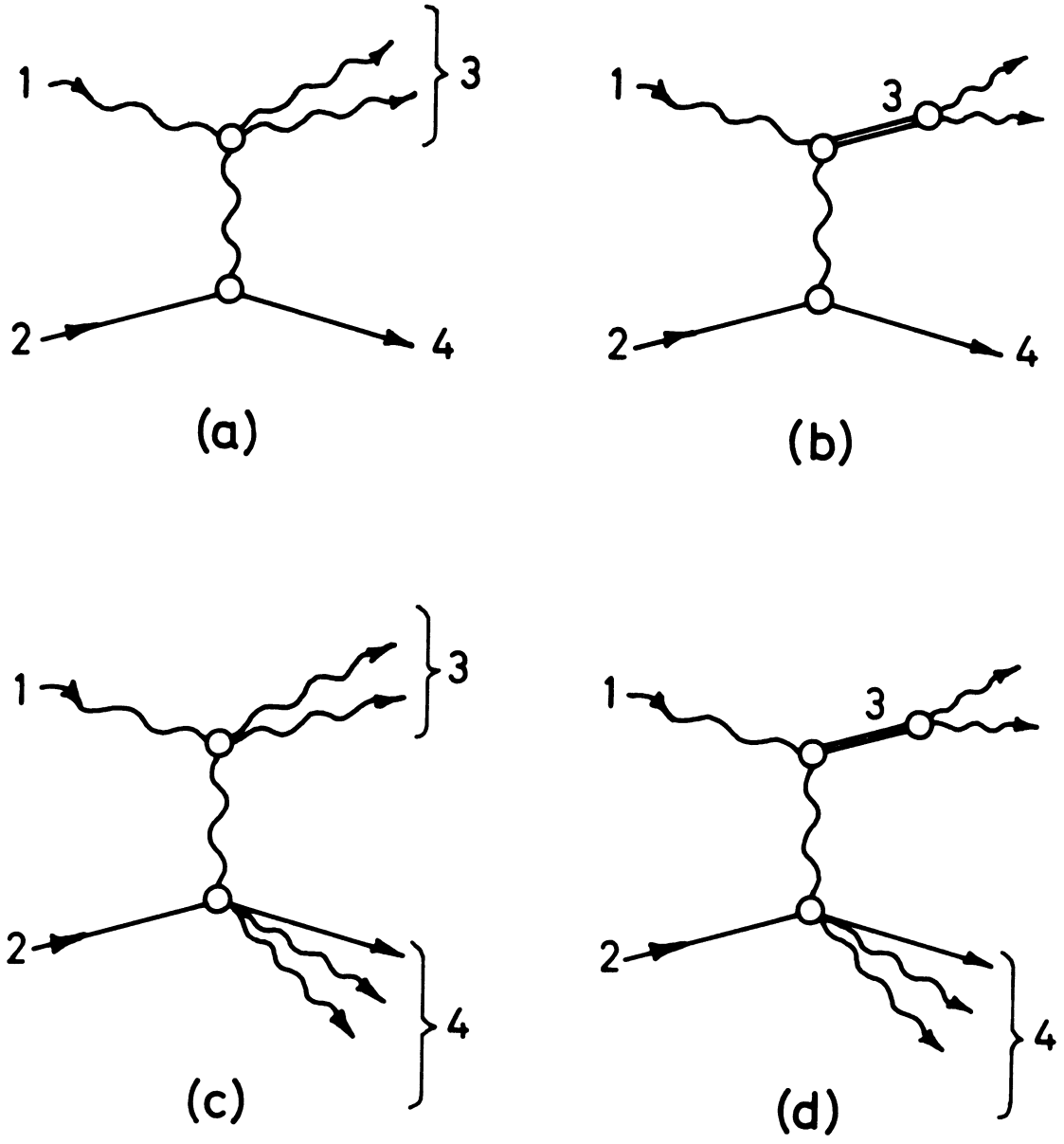

Figure 1

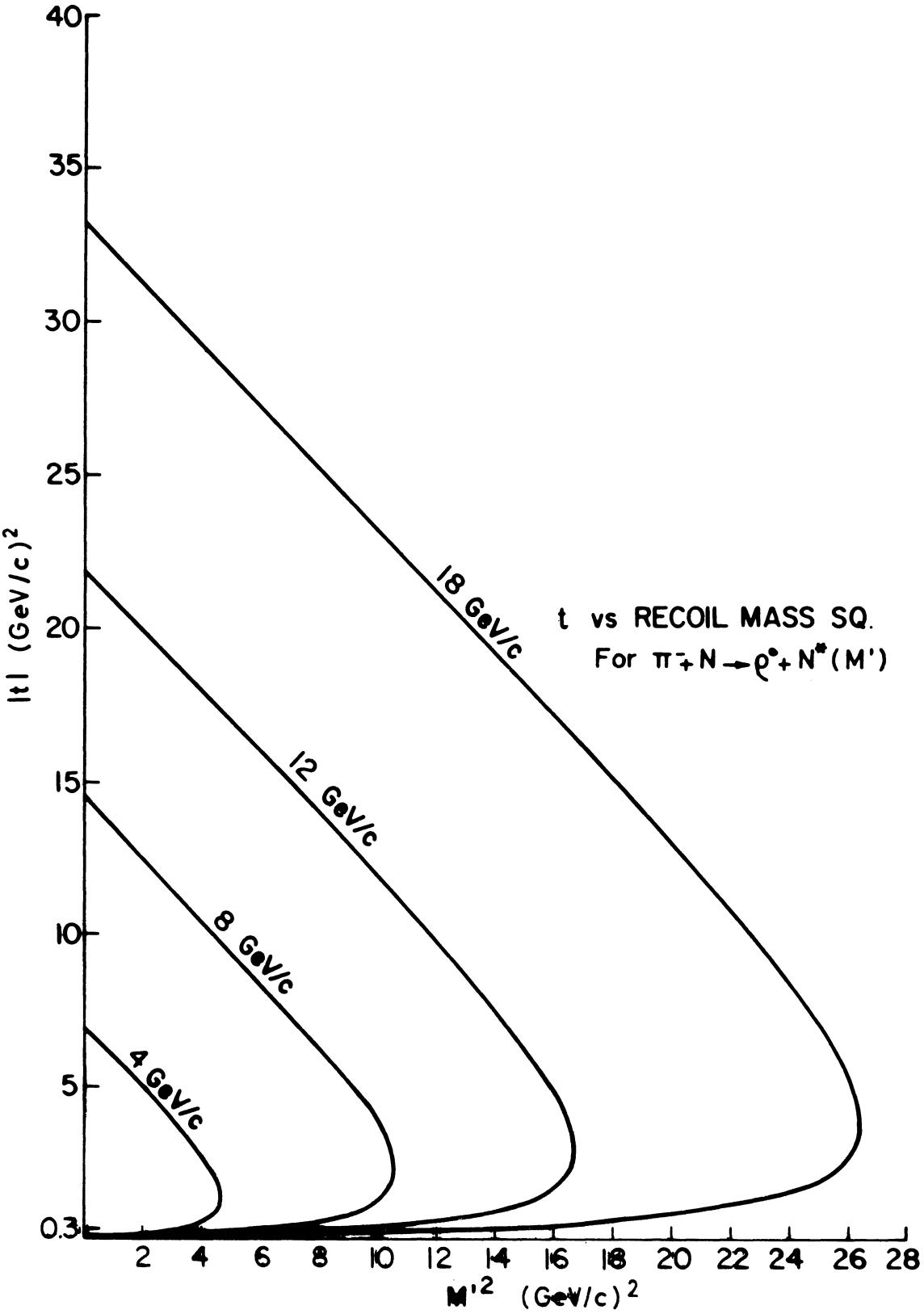
40
35
30
25
20
15
10
5
0.3
|t| (GeV/c)²
18 GeV/c
12 GeV/c
8 GeV/c
4 GeV/c
t vs RECOIL MASS SQ.
For π⁻ + N → ρ⁰ + N*(M')
2 4 6 8 10 12 14 16 18 20 22 24 26 28
M'² (GeV/c)²

Figure 2

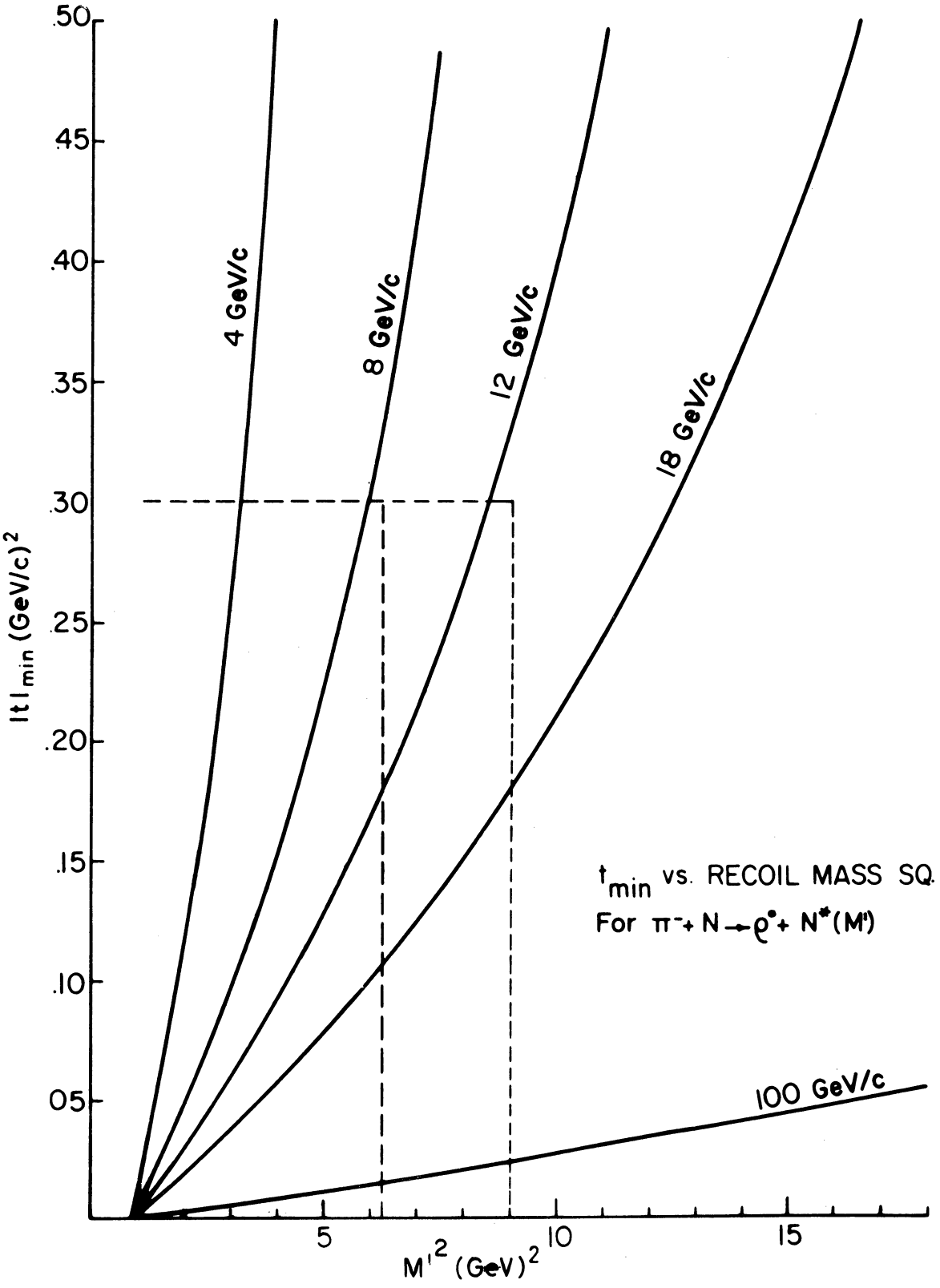
.50
.45
.40
.35
.30
.25
.20
.15
.10
05
$|t|_{min}$ (GeV/c)^2
4 GeV/c
8 GeV/c
12 GeV/c
18 GeV/c
100 GeV/c
t_{min} vs. RECOIL MASS SQ.
For $\pi^- + N \rightarrow \rho^0 + N^*(M')$
5
10
15
M'^2 (GeV)^2

Figure 3

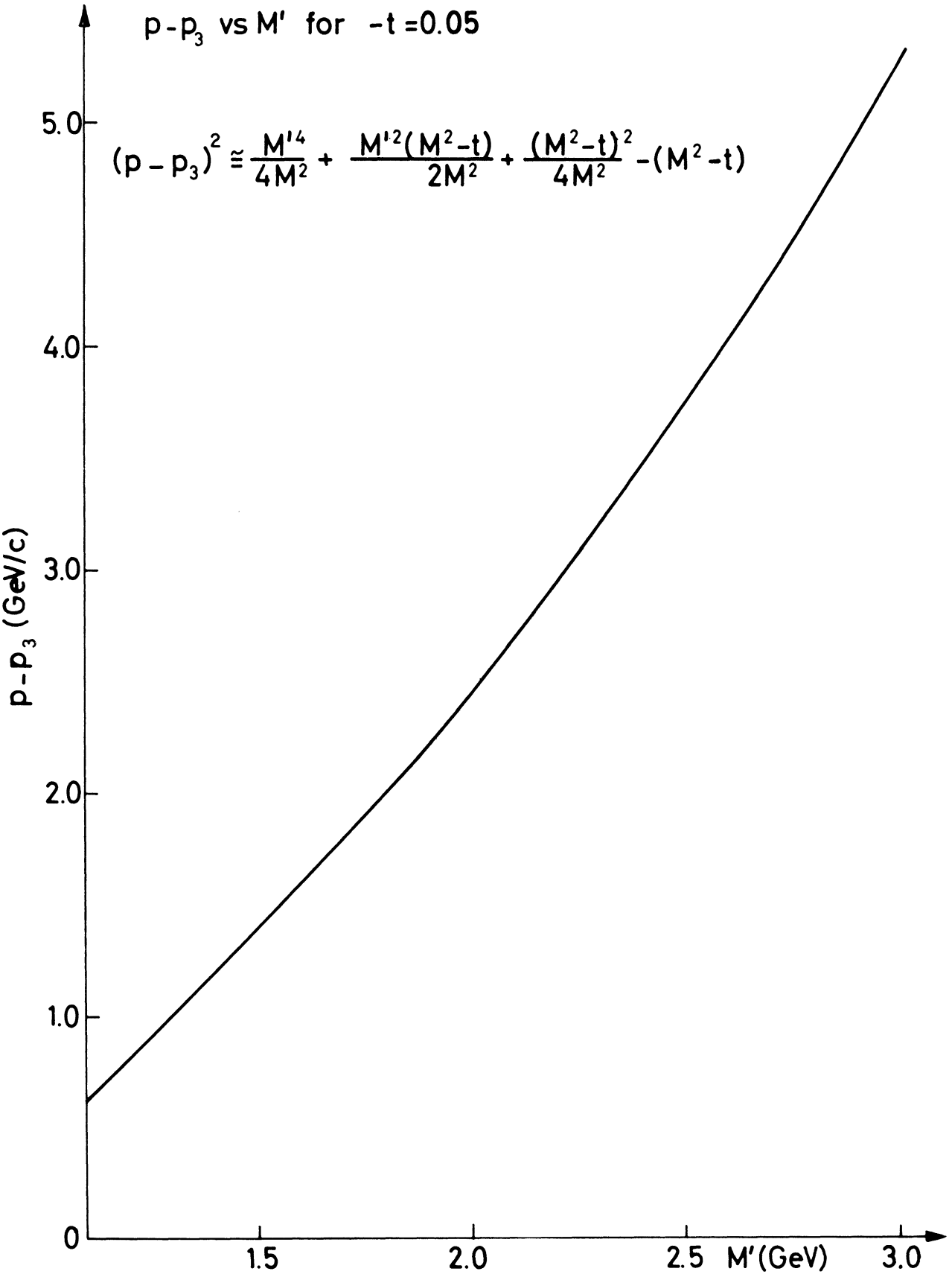
p - p3 vs M' for -t =0.05
(p - p3)2 ≅ M'4/4M2 + M'2(M2-t)/2M2 + (M2-t)2/4M2 -(M2-t)
p - p3 (GeV/c)
5.0
4.0
3.0
2.0
1.0
0
1.5
2.0
2.5
M'(GeV)
3.0

Figure 4

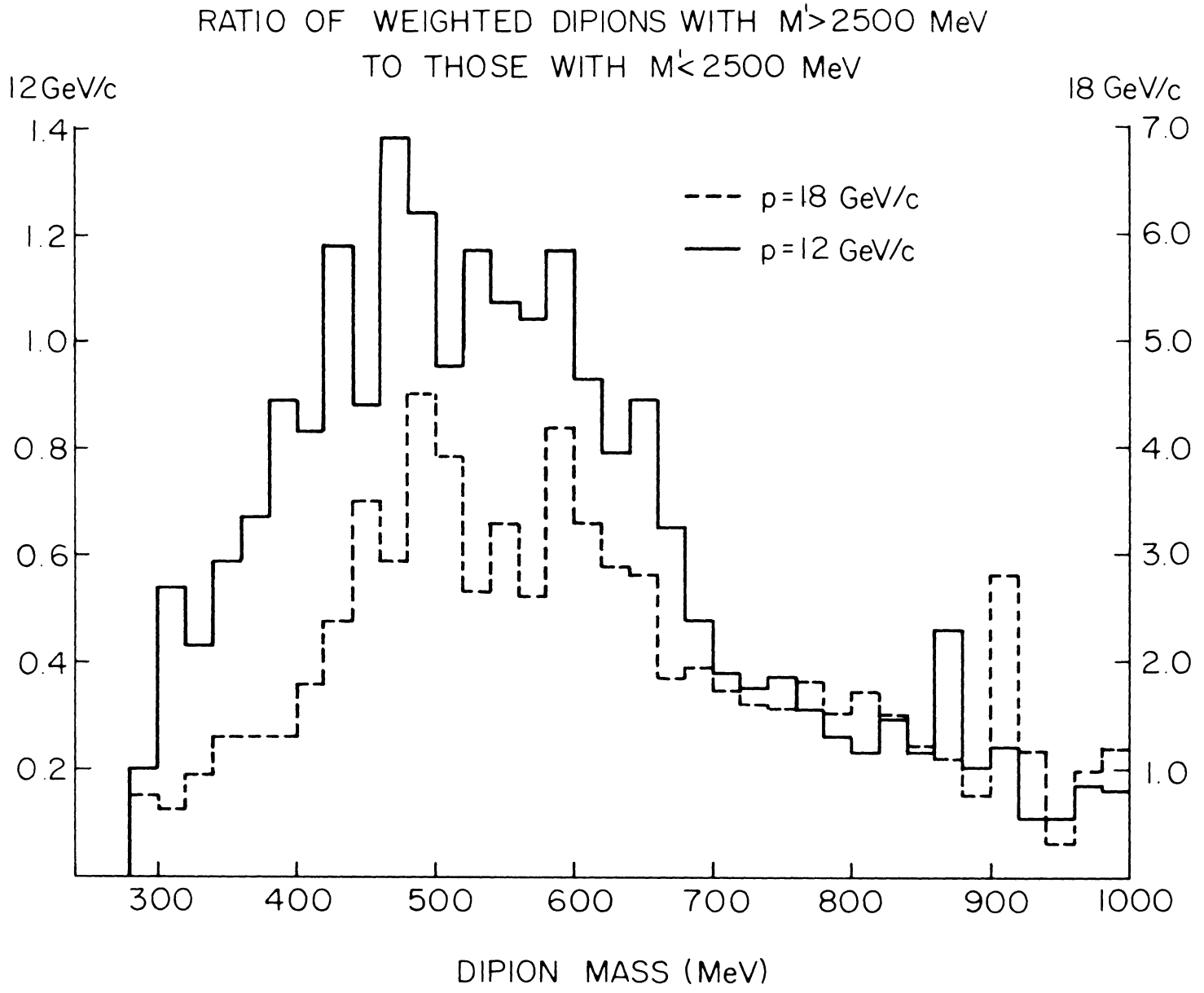
RATIO OF WEIGHTED DIPIONS WITH M'>2500 MeV
TO THOSE WITH M'<2500 MeV
12 GeV/c
18 GeV/c
1.4
1.2
1.0
0.8
0.6
0.4
0.2
7.0
6.0
5.0
4.0
3.0
2.0
1.0
p=18 GeV/c
p=12 GeV/c
300
400
500
600
700
800
900
1000
DIPION MASS (MeV)

Figure 5

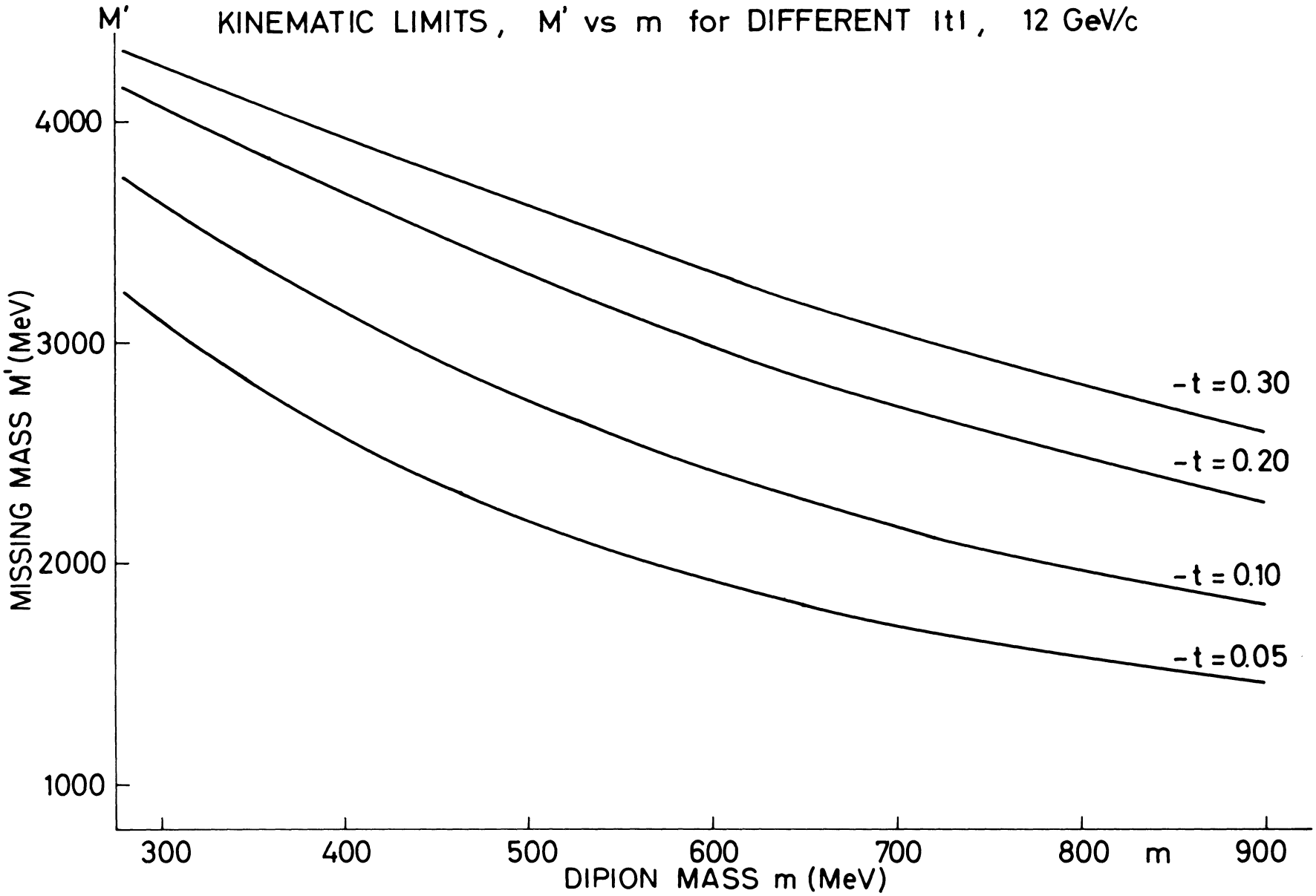
M'
KINEMATIC LIMITS, M' vs m for DIFFERENT |t|, 12 GeV/c
4000
3000
2000
1000
MISSING MASS M' (MeV)
-t = 0.30
-t = 0.20
-t = 0.10
-t = 0.05
300
400
500
600
700
800
m
900
DIPION MASS m (MeV)

Figure 6

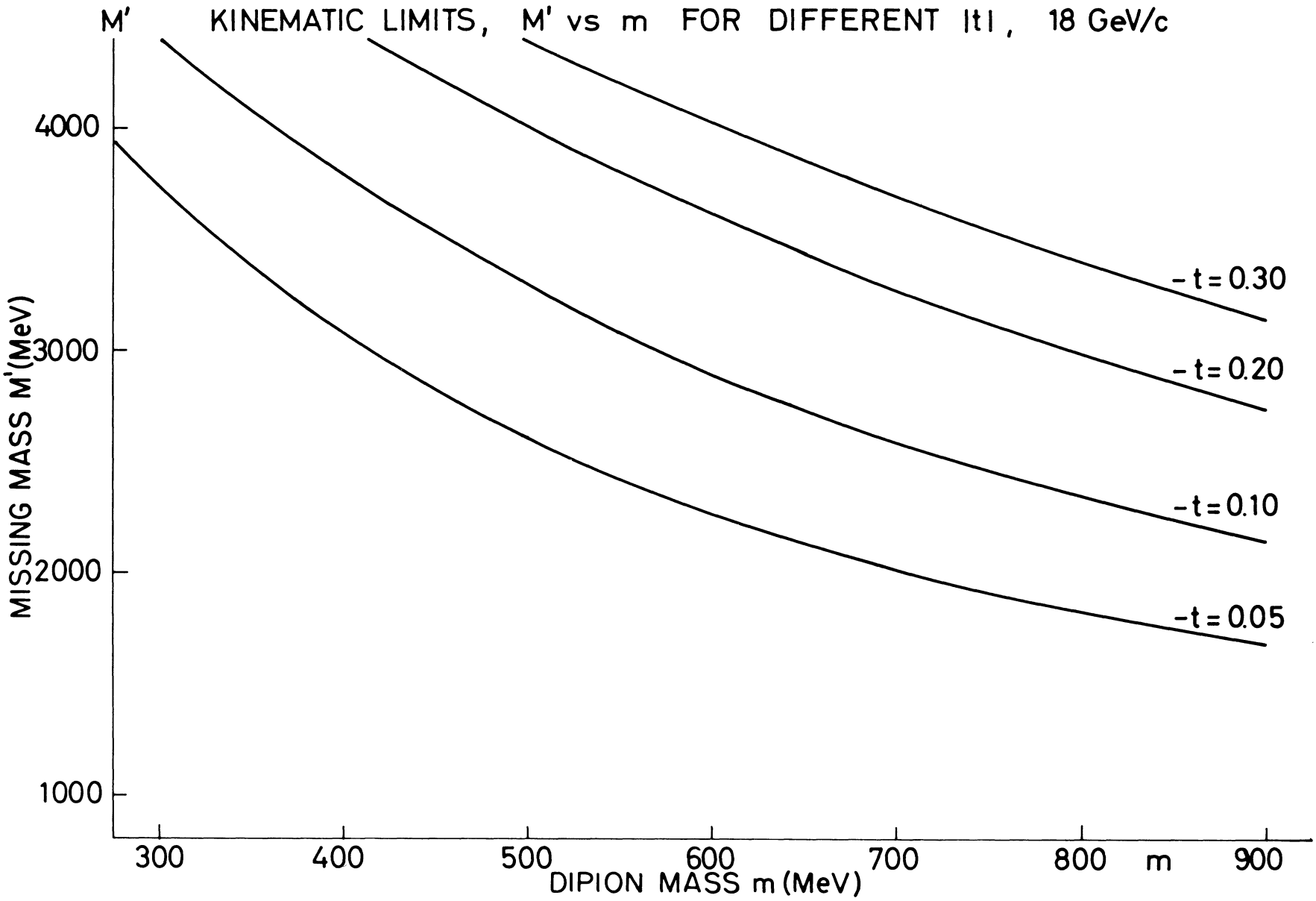
M'
KINEMATIC LIMITS, M' vs m FOR DIFFERENT |t|, 18 GeV/c
4000
3000
2000
1000
MISSING MASS M'(MeV)
-t = 0.30
-t = 0.20
-t = 0.10
-t = 0.05
300
400
500
600
700
800
m
900
DIPION MASS m (MeV)

Figure 7

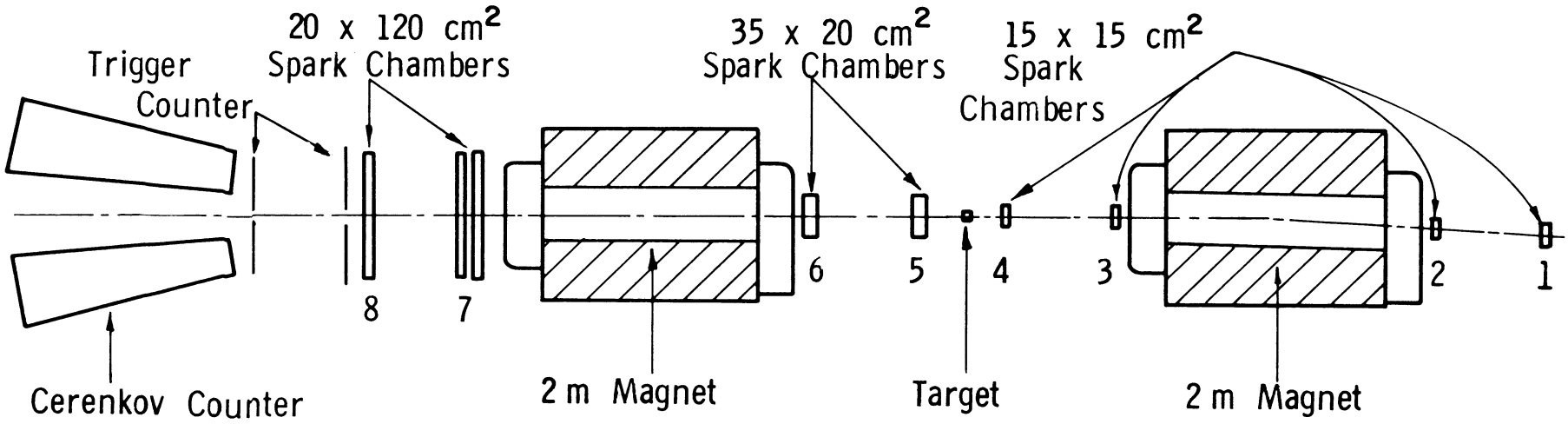

GEOMETRY FOR DIBOSON EXPERIMENT

(PLAN VIEW)

Figure 8

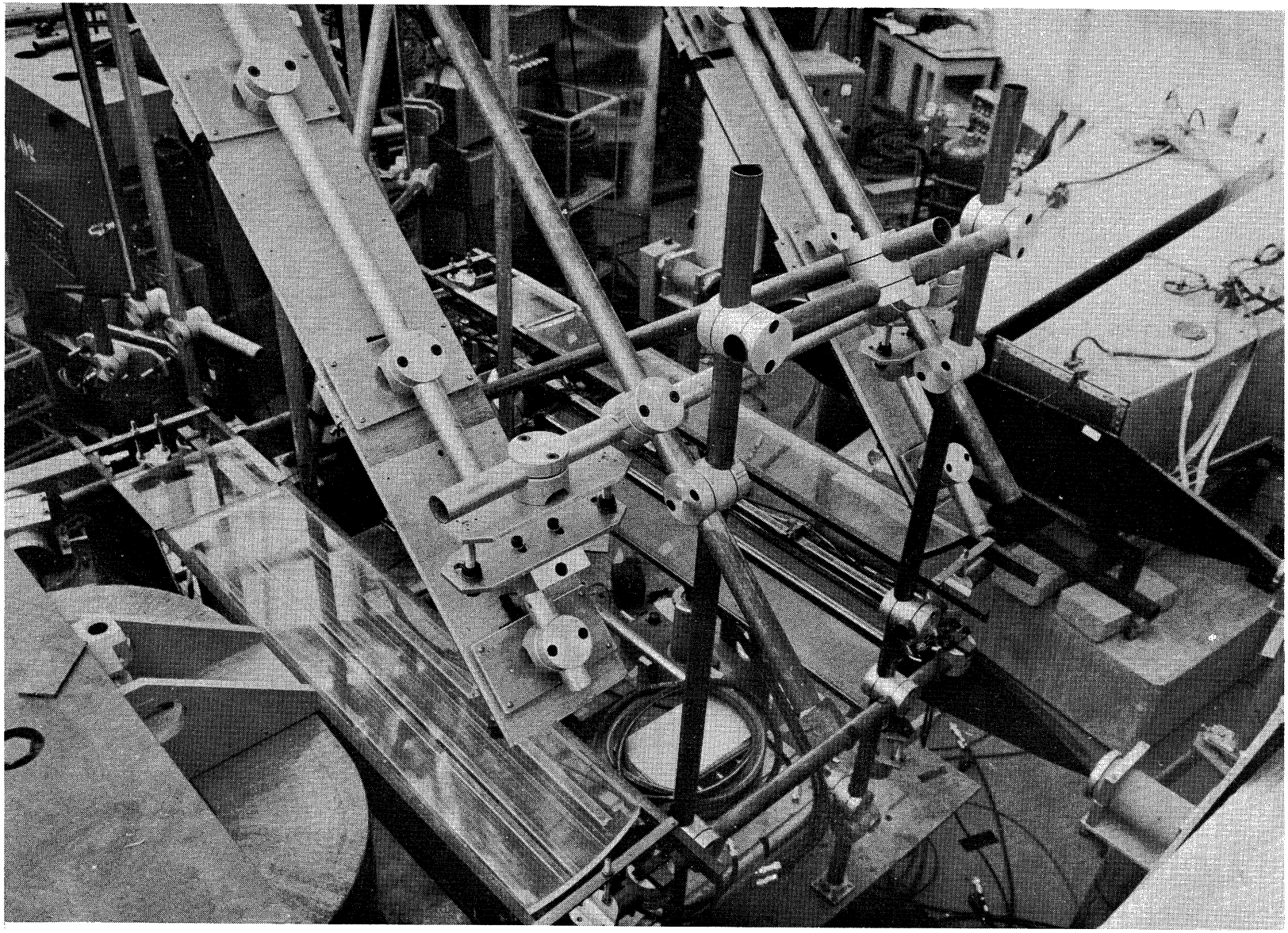

Figure 9

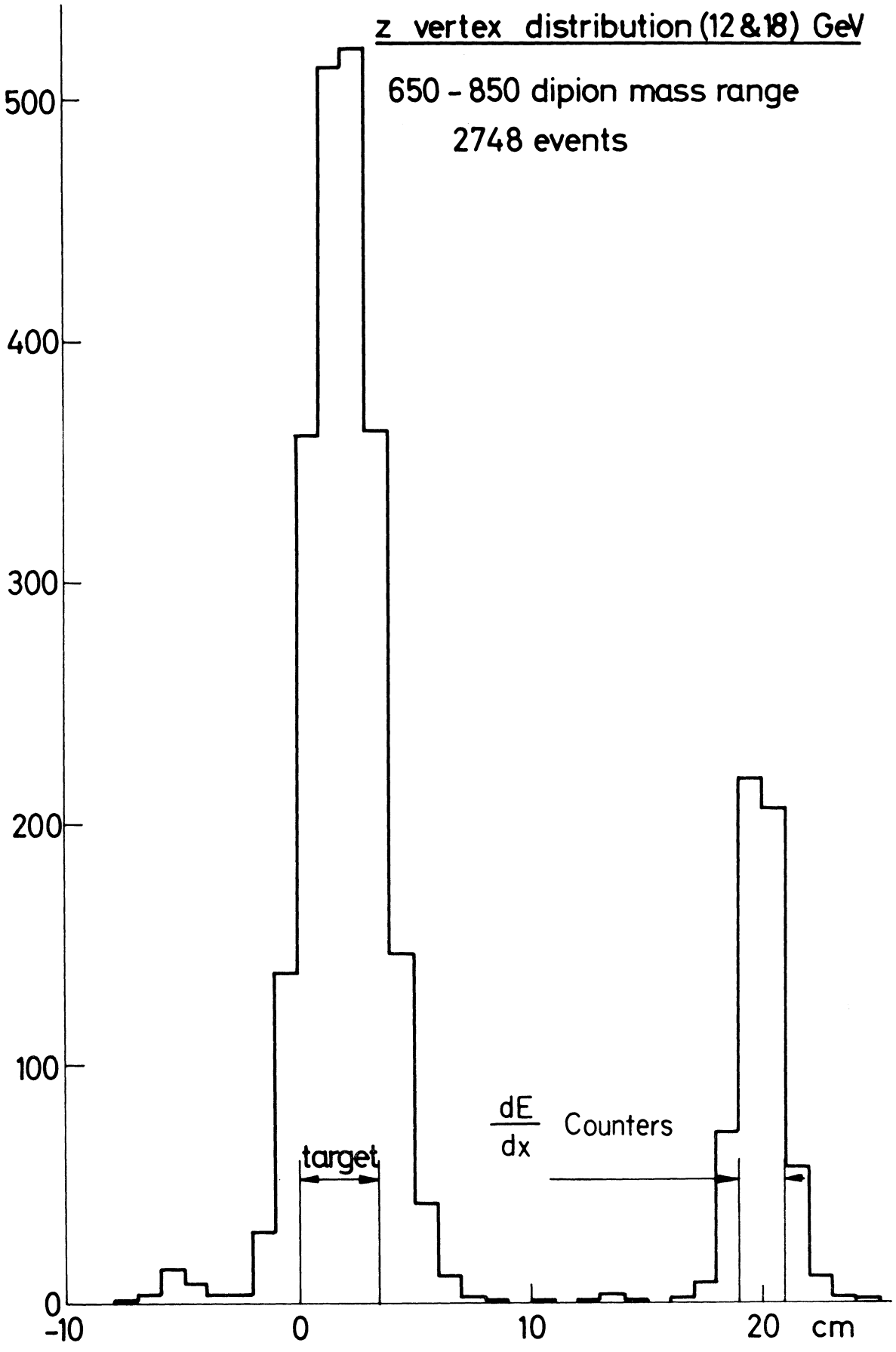
z vertex distribution (12 & 18) GeV
650 - 850 dipion mass range
2748 events
500
400
300
200
100
0
-10
0
10
20
cm
target
dE/dx
Counters

Figure 10

THRESHOLD GAS ČERENKOV COUNTER

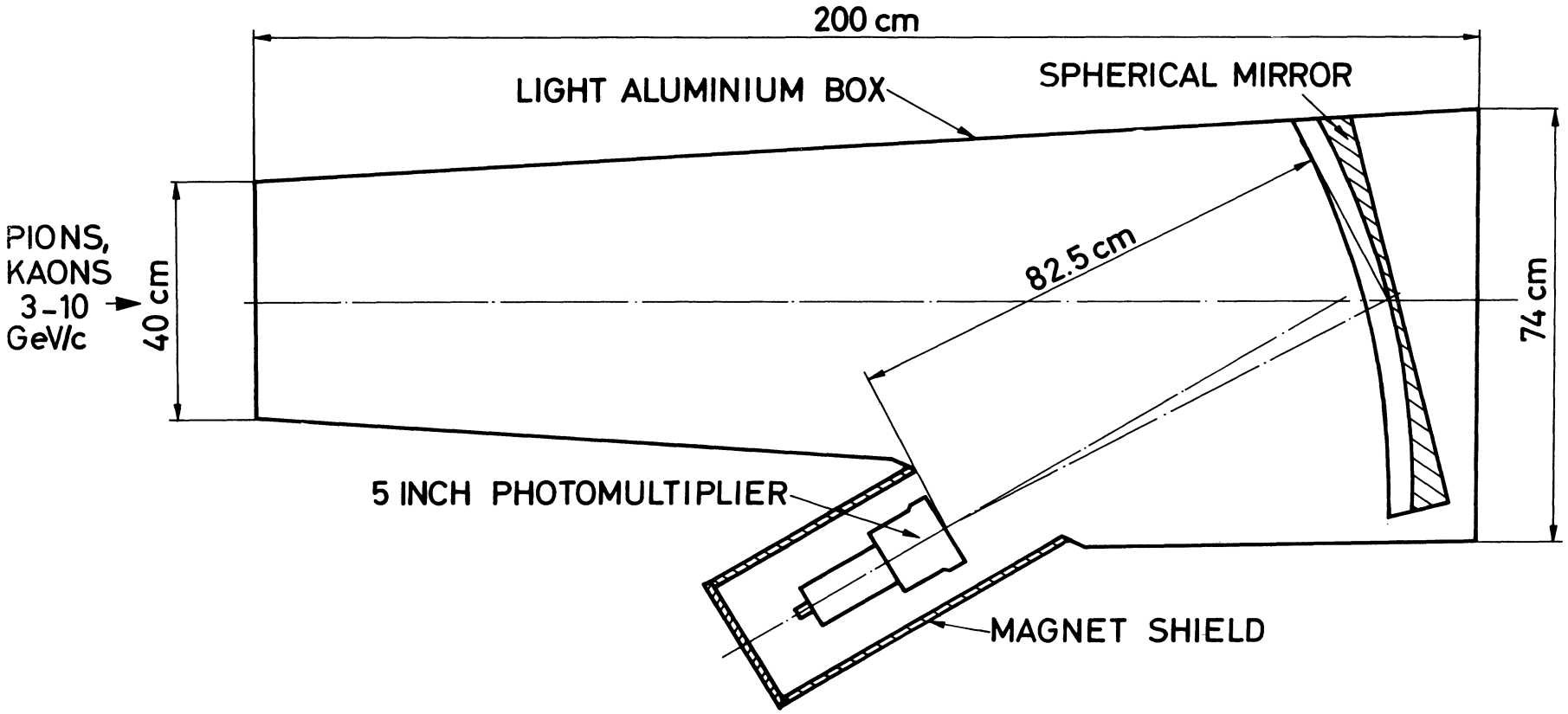

Figure 11

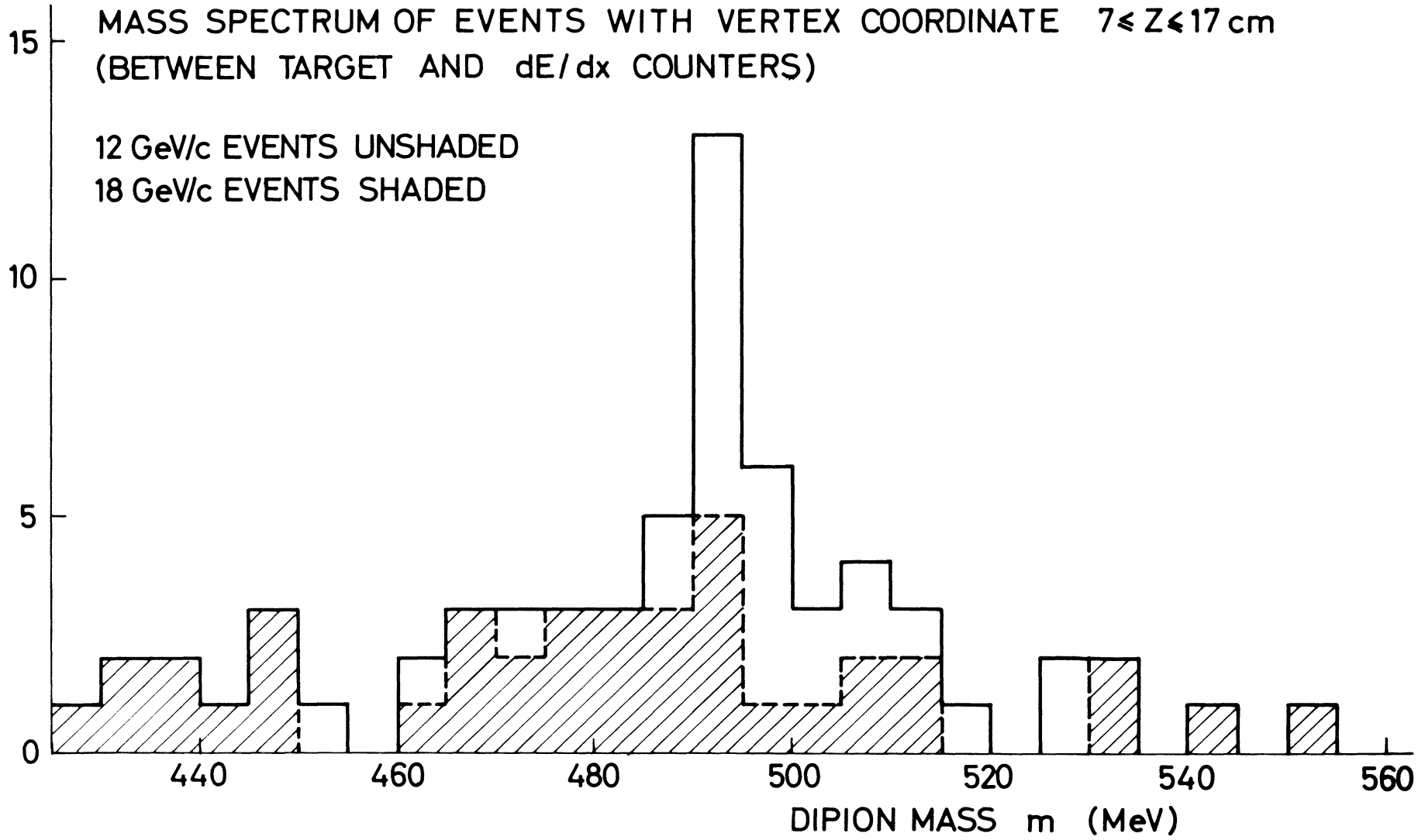
MASS SPECTRUM OF EVENTS WITH VERTEX COORDINATE 7≤Z≤17 cm
(BETWEEN TARGET AND dE/dx COUNTERS)
12 GeV/c EVENTS UNSHADED
18 GeV/c EVENTS SHADED
15
10
5
0
440
460
480
500
520
540
560
DIPION MASS m (MeV)

Figure 12

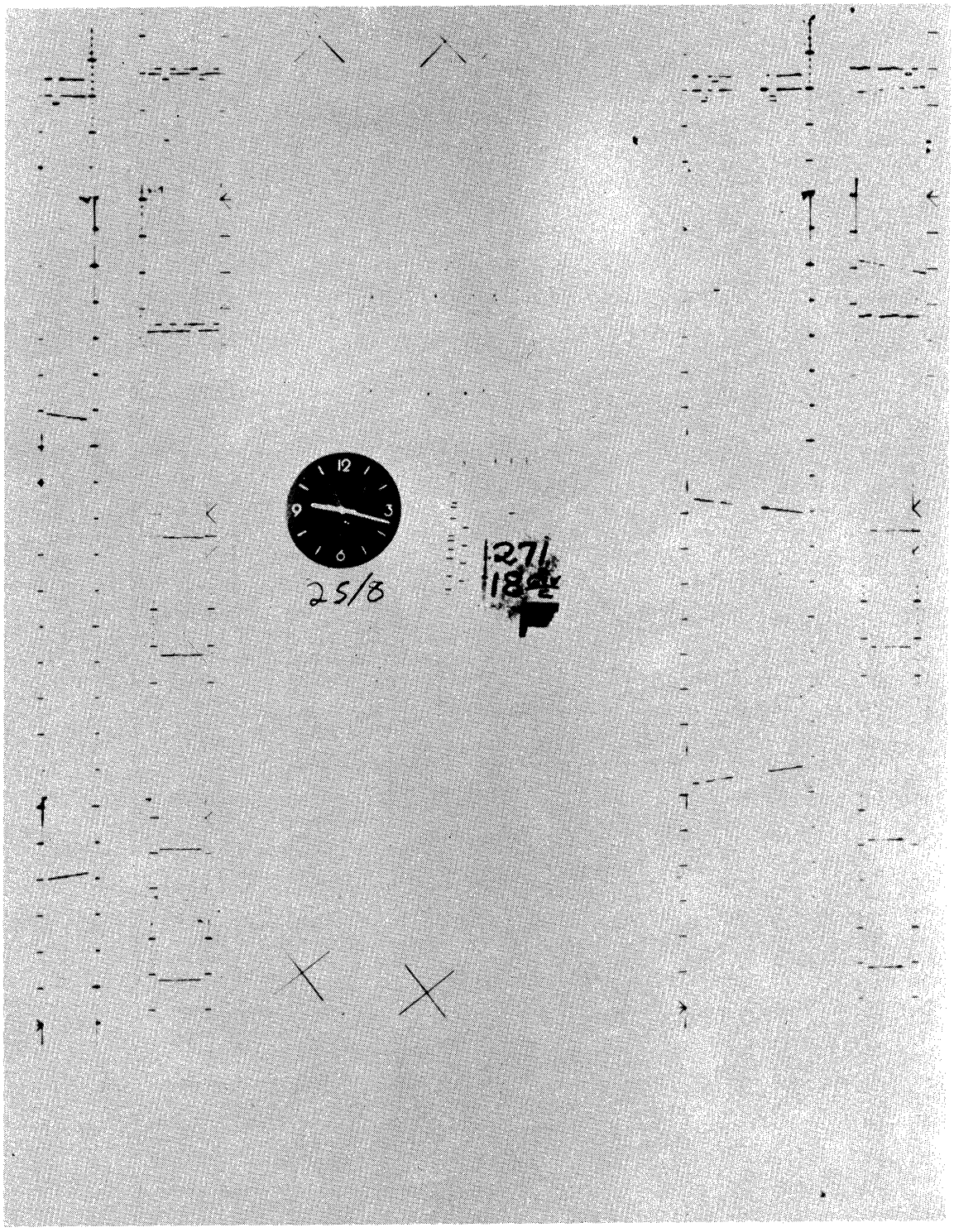

Figure 13

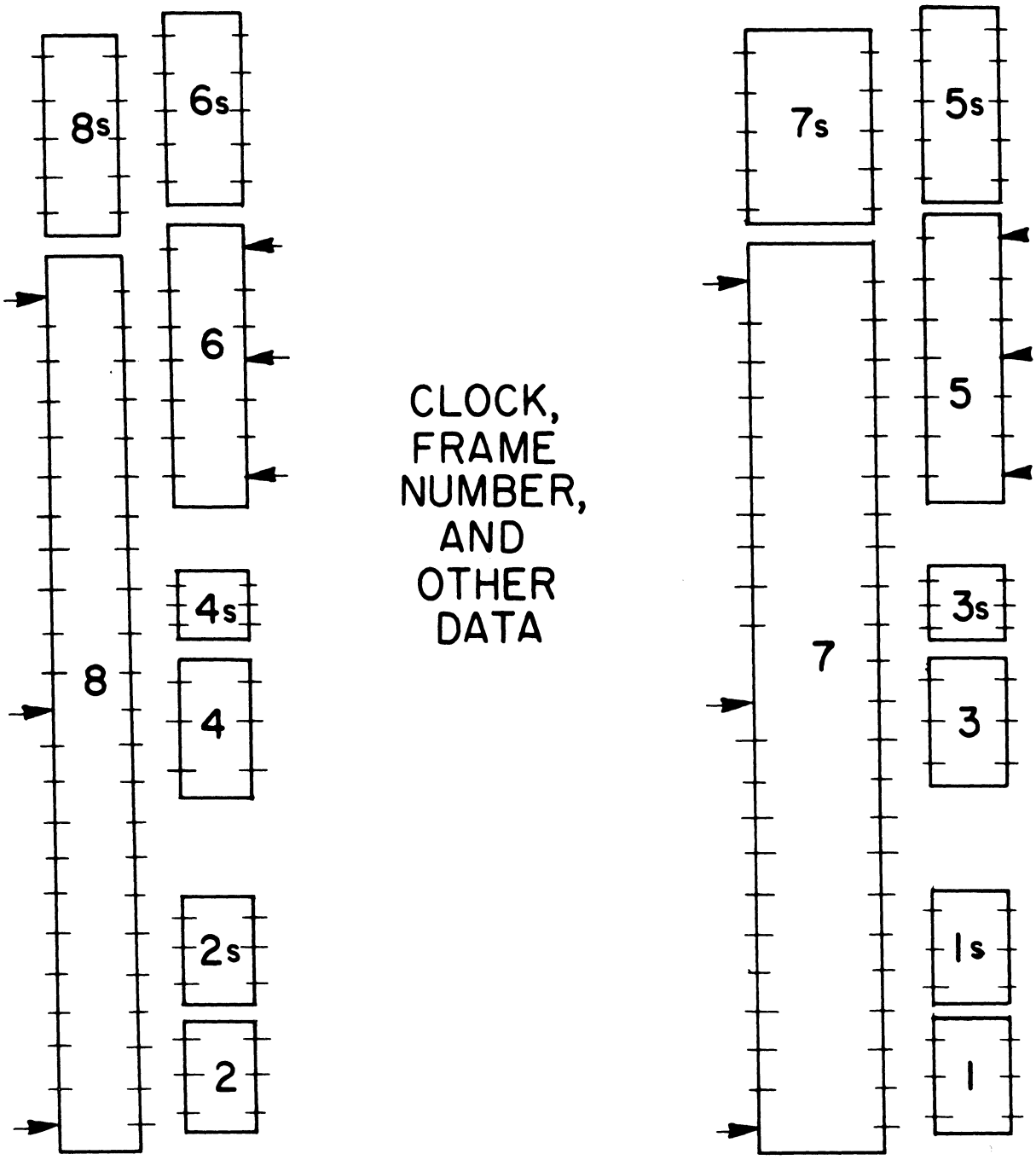
8s
6s
6
8
4s
4
2s
2
CLOCK,
FRAME
NUMBER,
AND
OTHER
DATA
7s
5s
5
7
3s
3
1s
1

Figure 14

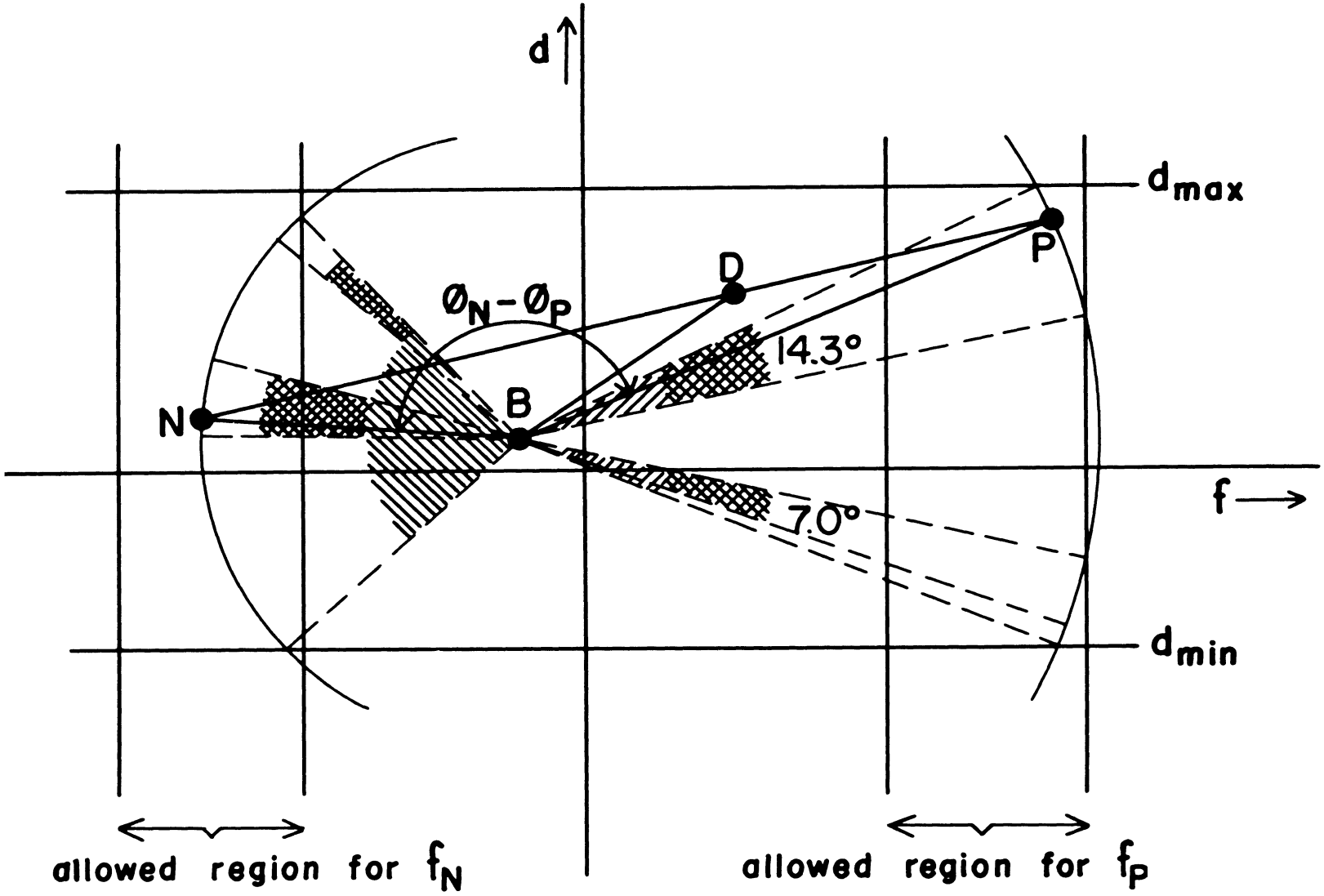
d
d_{max}
d_{min}
P
D
$\emptyset_N - \emptyset_P$
14.3°
B
N
7.0°
f
allowed region for f_N
allowed region for f_P

Figure 15

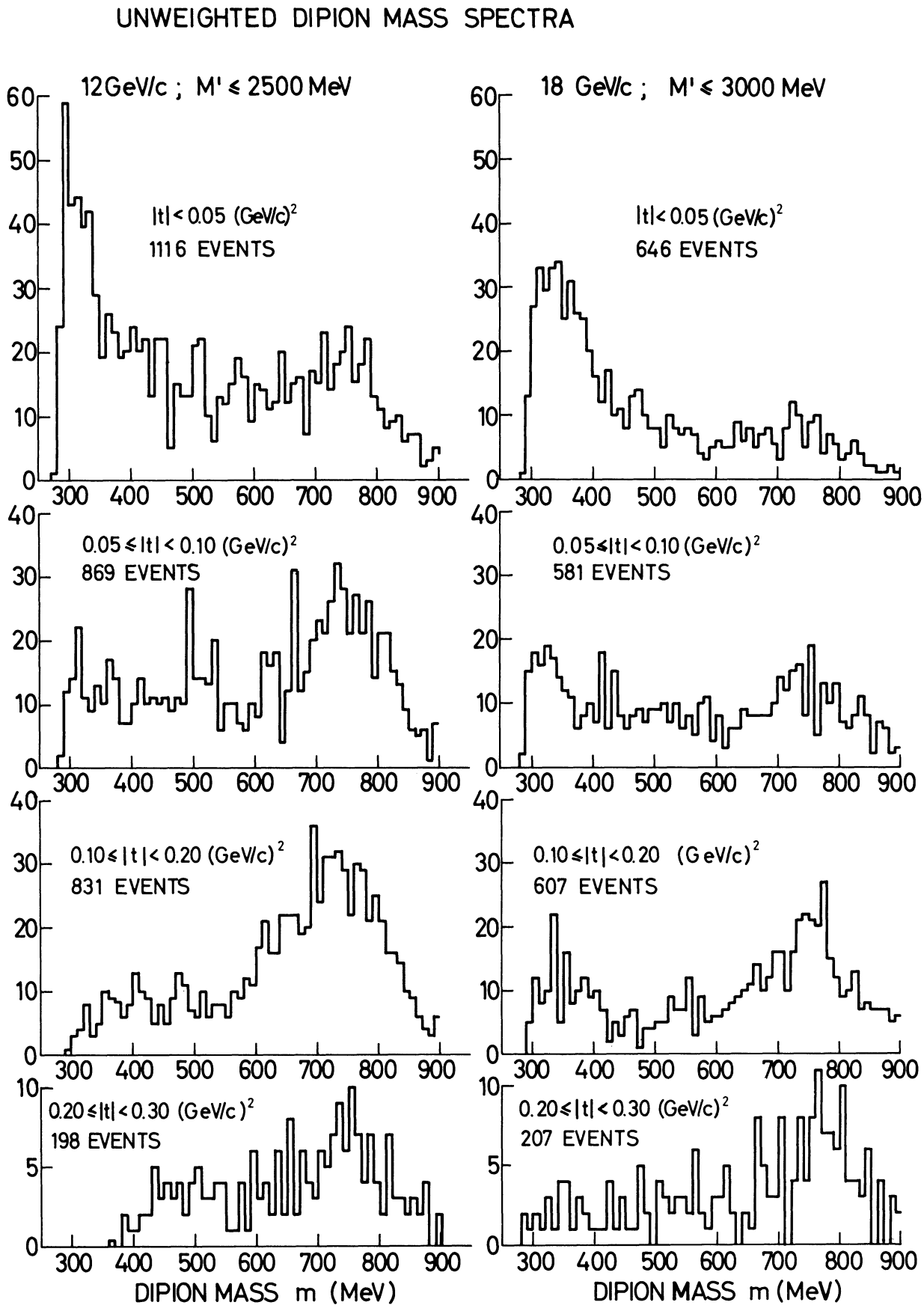
UNWEIGHTED DIPION MASS SPECTRA
12GeV/c ; M' ≤ 2500 MeV
|t| < 0.05 (GeV/c)²
1116 EVENTS
18 GeV/c ; M' ≤ 3000 MeV
|t| < 0.05 (GeV/c)²
646 EVENTS
0.05 ≤ |t| < 0.10 (GeV/c)²
869 EVENTS
0.05 ≤ |t| < 0.10 (GeV/c)²
581 EVENTS
0.10 ≤ |t| < 0.20 (GeV/c)²
831 EVENTS
0.10 ≤ |t| < 0.20 (GeV/c)²
607 EVENTS
0.20 ≤ |t| < 0.30 (GeV/c)²
198 EVENTS
0.20 ≤ |t| < 0.30 (GeV/c)²
207 EVENTS
DIPION MASS m (MeV)
DIPION MASS m (MeV)

Figure 16

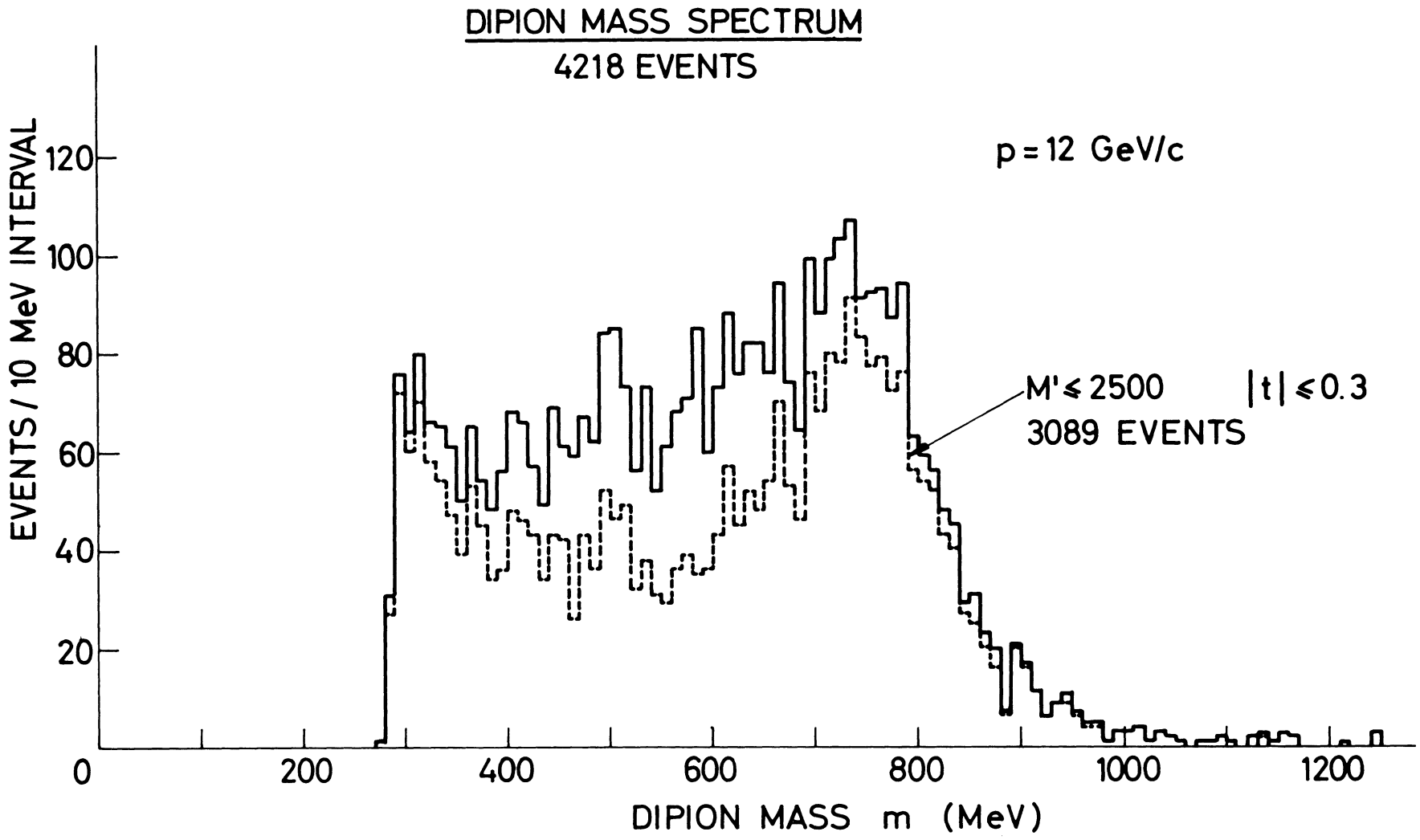
DIPION MASS SPECTRUM
4218 EVENTS
p = 12 GeV/c
M' ≤ 2500
|t| ≤ 0.3
3089 EVENTS
EVENTS / 10 MeV INTERVAL
0
20
40
60
80
100
120
200
400
600
800
1000
1200
DIPION MASS m (MeV)

Figure 17

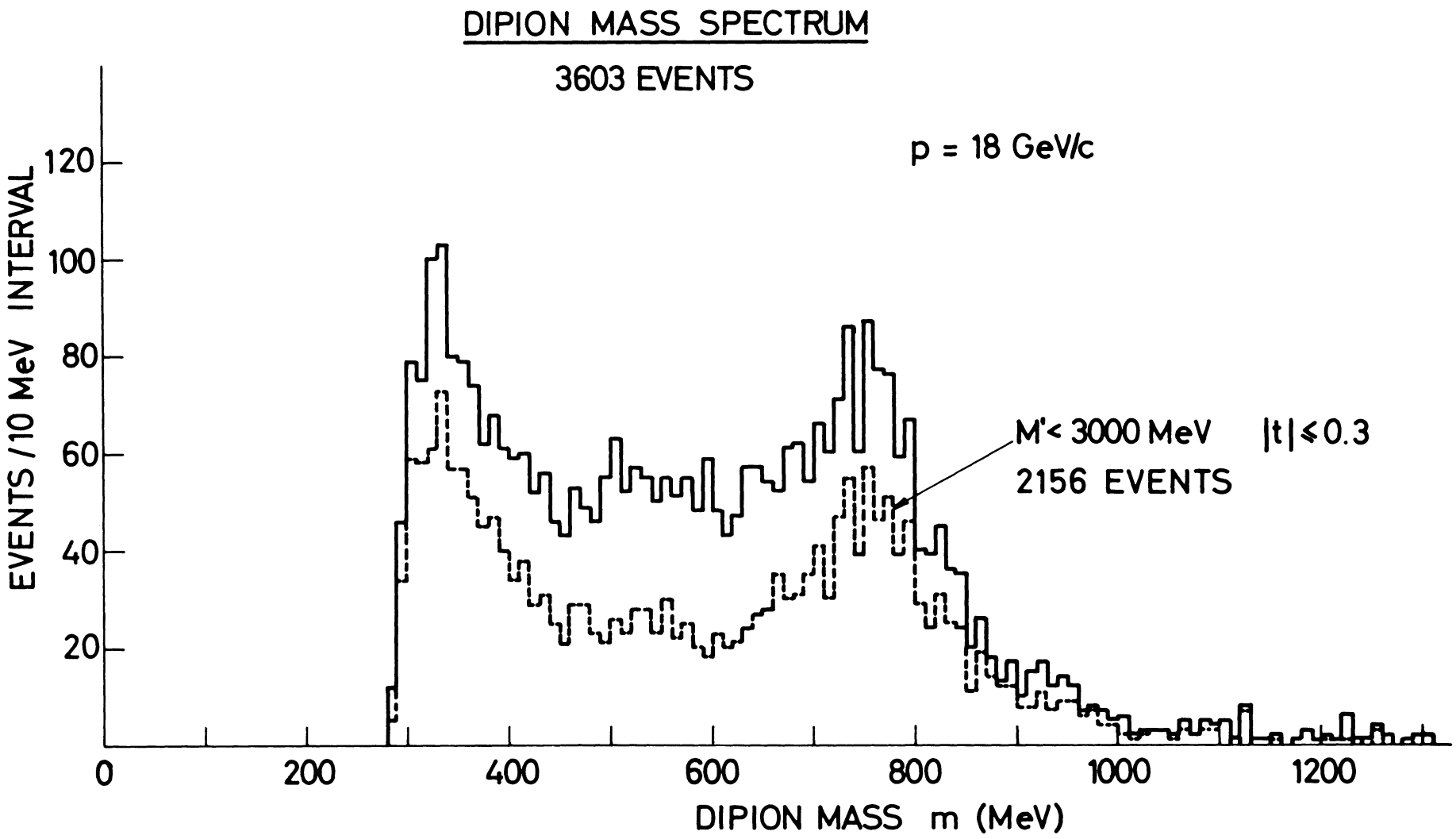
DIPION MASS SPECTRUM
3603 EVENTS
p = 18 GeV/c
M'< 3000 MeV |t|≤0.3
2156 EVENTS
EVENTS /10 MeV INTERVAL
120
100
80
60
40
20
0
200
400
600
800
1000
1200
DIPION MASS m (MeV)

Figure 18

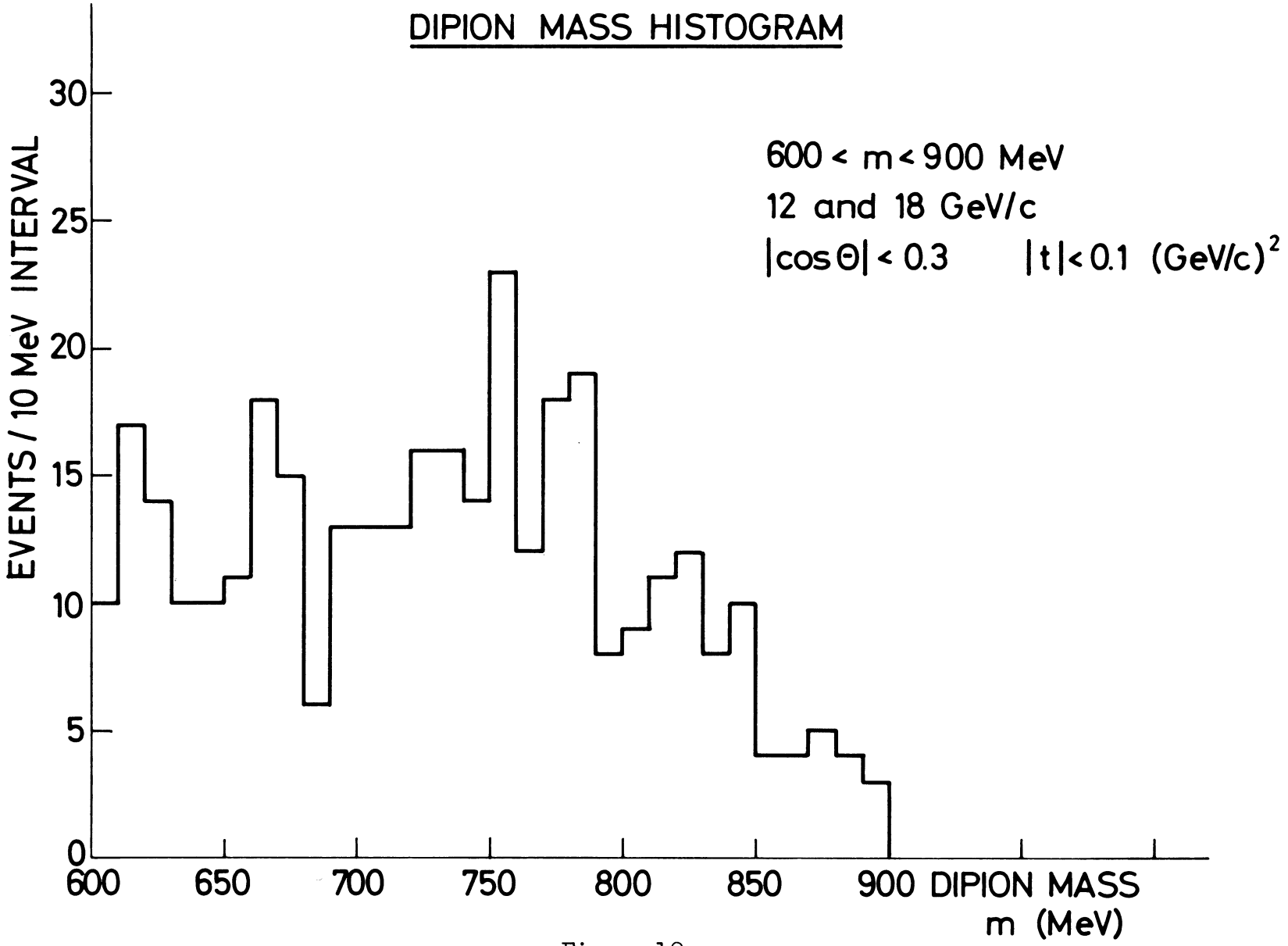
DIPION MASS HISTOGRAM
600 < m < 900 MeV
12 and 18 GeV/c
|cos Θ| < 0.3
|t| < 0.1 (GeV/c)²
EVENTS / 10 MeV INTERVAL
0
5
10
15
20
25
30
600
650
700
750
800
850
900
DIPION MASS
m (MeV)

Figure 19

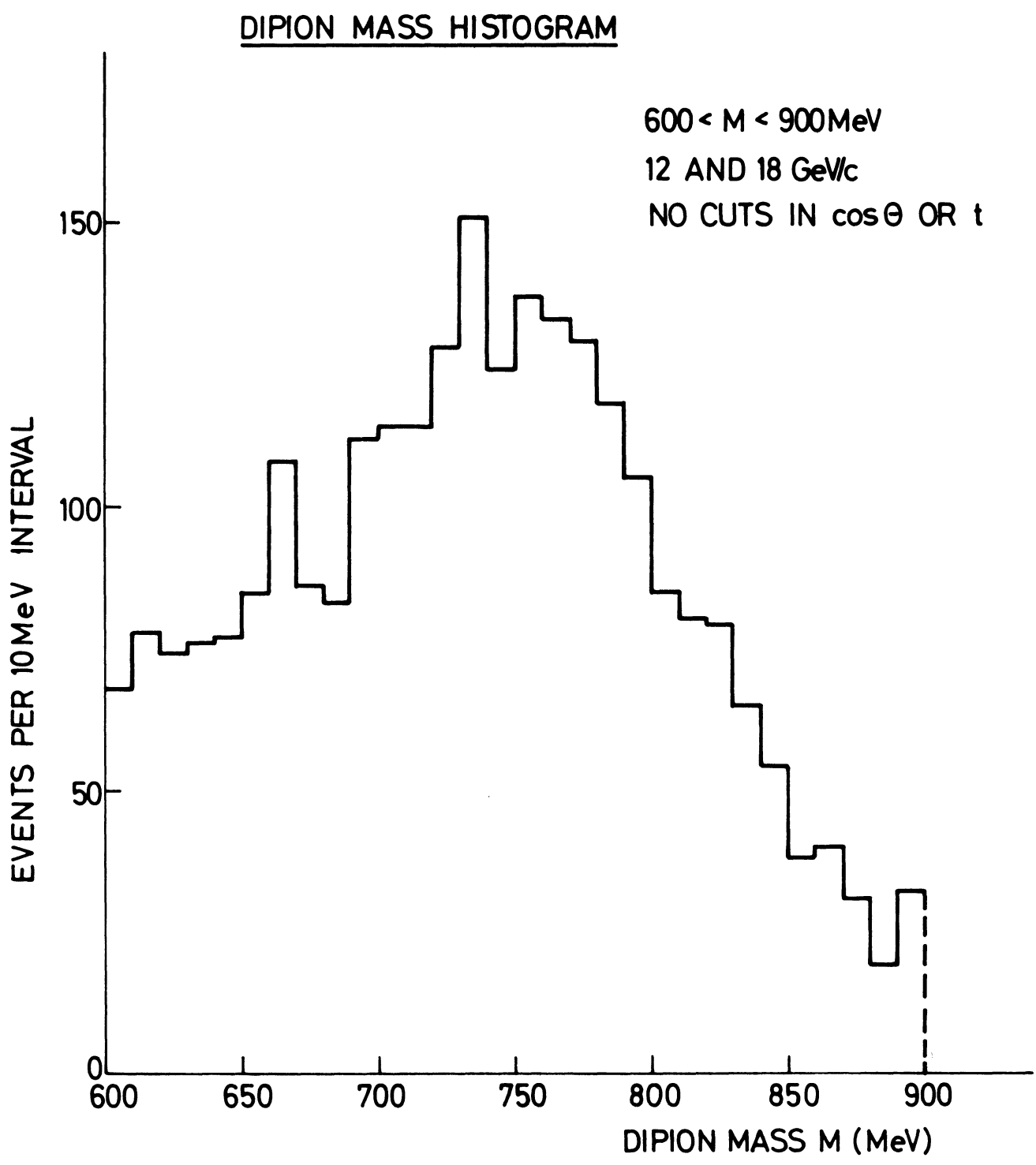
DIPION MASS HISTOGRAM
600 < M < 900 MeV
12 AND 18 GeV/c
NO CUTS IN cosΘ OR t
EVENTS PER 10 MeV INTERVAL
150
100
50
0
600
650
700
750
800
850
900
DIPION MASS M (MeV)

Figure 20

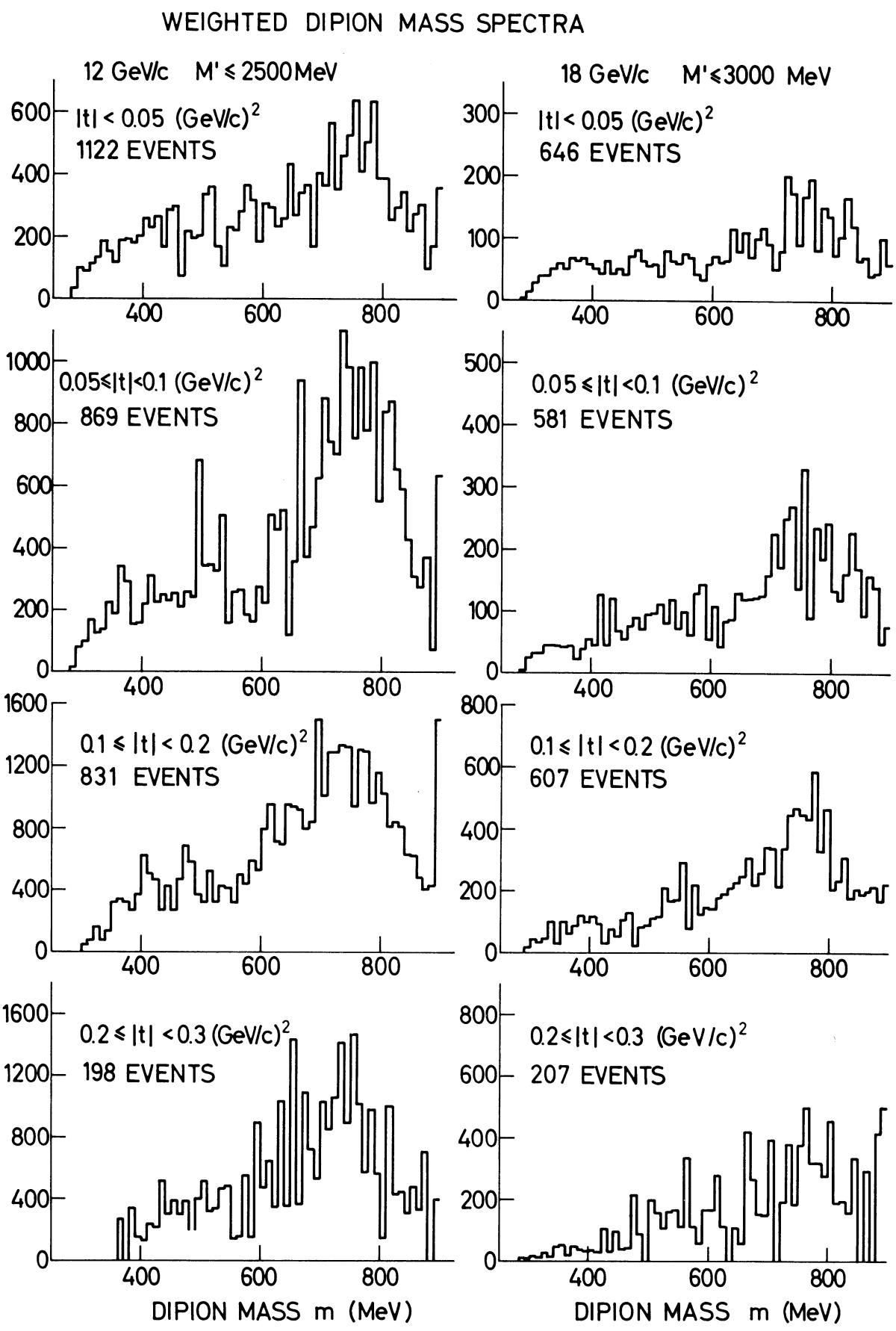
WEIGHTED DIPION MASS SPECTRA
12 GeV/c M' ≤ 2500MeV
|t| < 0.05 (GeV/c)²
1122 EVENTS
18 GeV/c M'≤3000 MeV
|t|< 0.05 (GeV/c)²
646 EVENTS
0.05≤|t|<0.1 (GeV/c)²
869 EVENTS
0.05 ≤|t|<0.1 (GeV/c)²
581 EVENTS
0.1 ≤ |t| < 0.2 (GeV/c)²
831 EVENTS
0.1 ≤ |t| < 0.2 (GeV/c)²
607 EVENTS
0.2 ≤ |t| < 0.3 (GeV/c)²
198 EVENTS
0.2≤|t|<0.3 (GeV/c)²
207 EVENTS
DIPION MASS m (MeV)
DIPION MASS m (MeV)

Figure 21

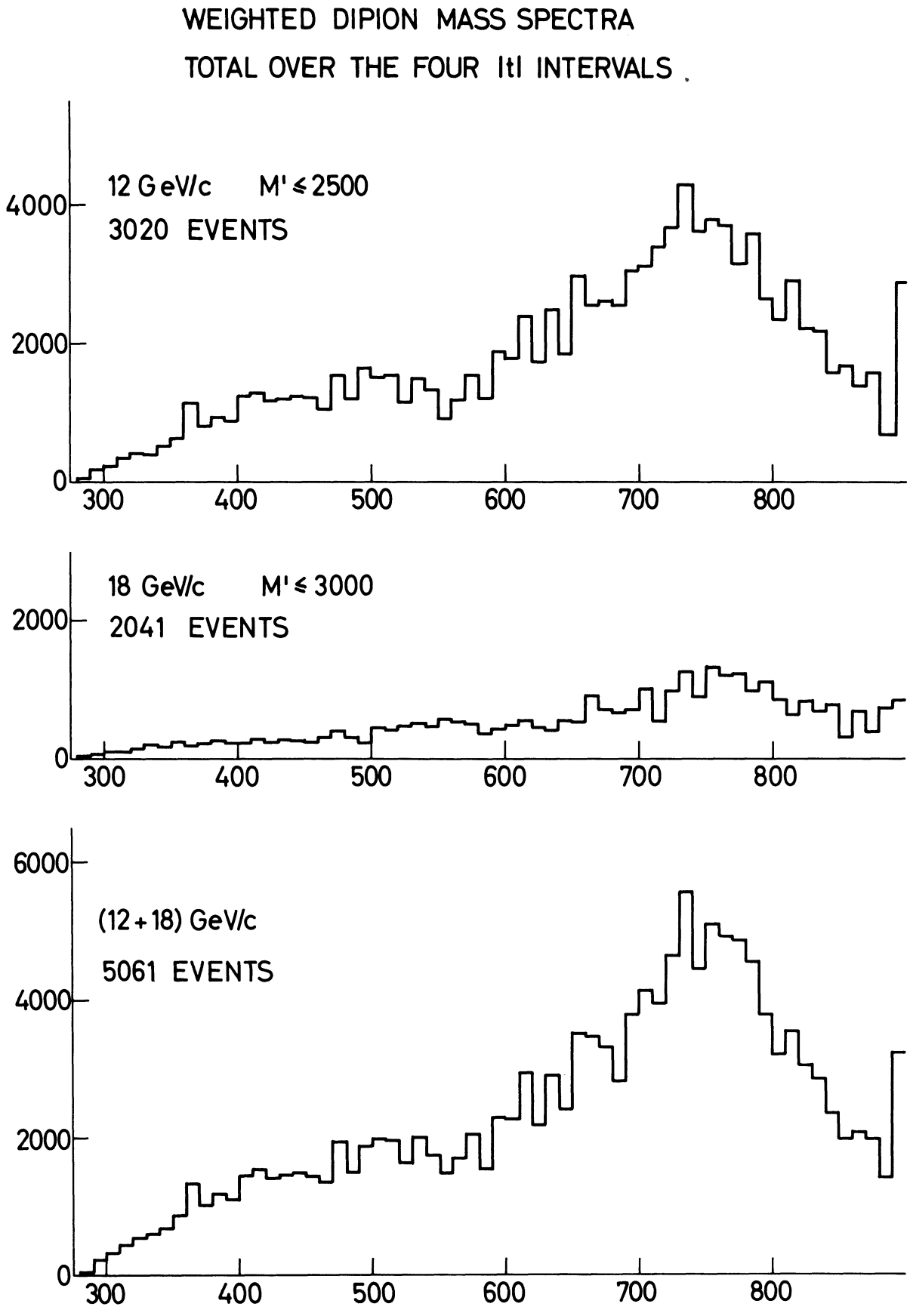
WEIGHTED DIPION MASS SPECTRA
TOTAL OVER THE FOUR |t| INTERVALS
12 GeV/c M' ≤ 2500
3020 EVENTS
4000
2000
0
300
400
500
600
700
800
18 GeV/c M' ≤ 3000
2041 EVENTS
2000
0
300
400
500
600
700
800
6000
(12+18) GeV/c
5061 EVENTS
4000
2000
0
300
400
500
600
700
800

Figure 22

WEIGHTED DIPION MASS SPECTRA INCLUDING
ANGULAR DISTRIBUTION EXTRAPOLATIONS

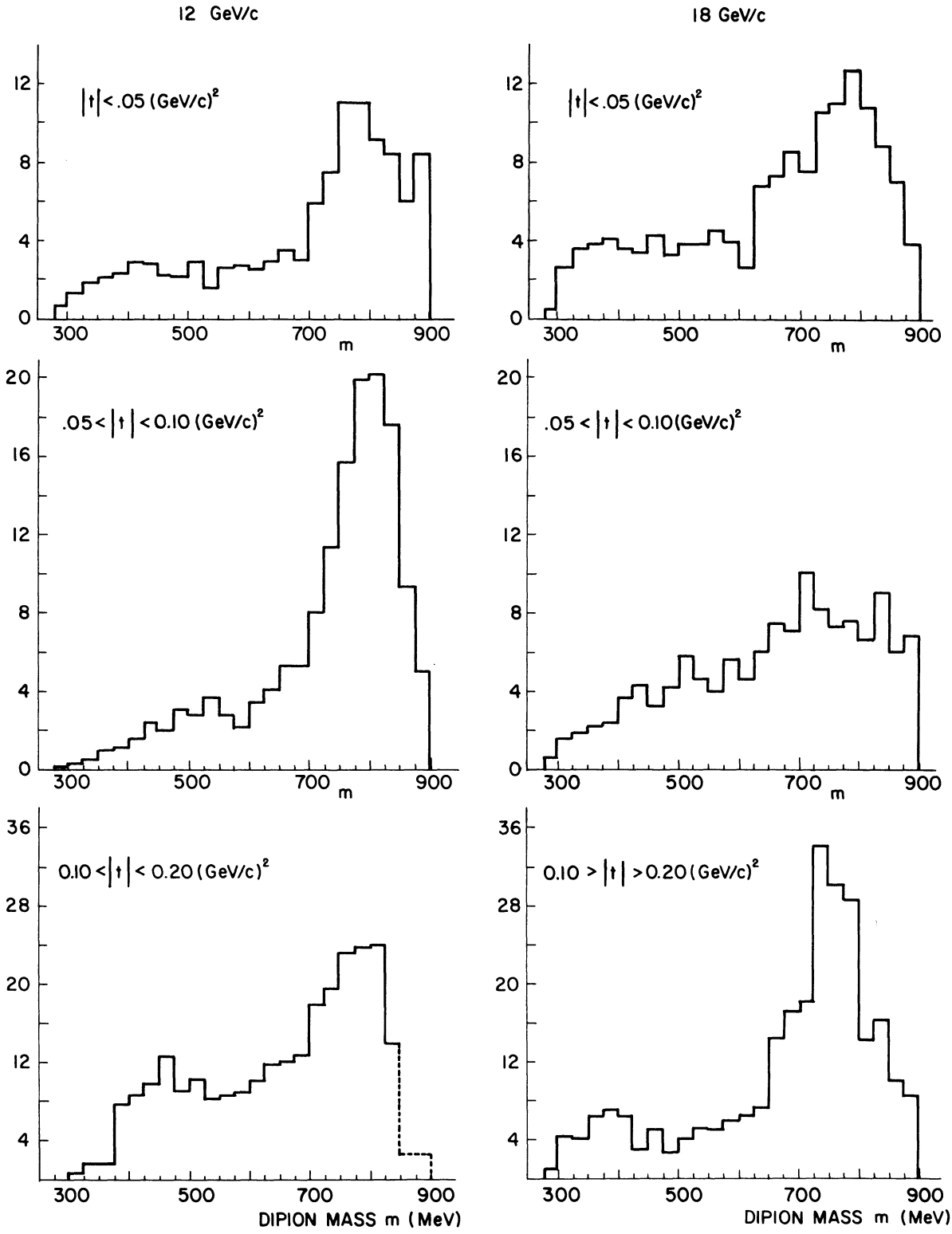

Figure 23

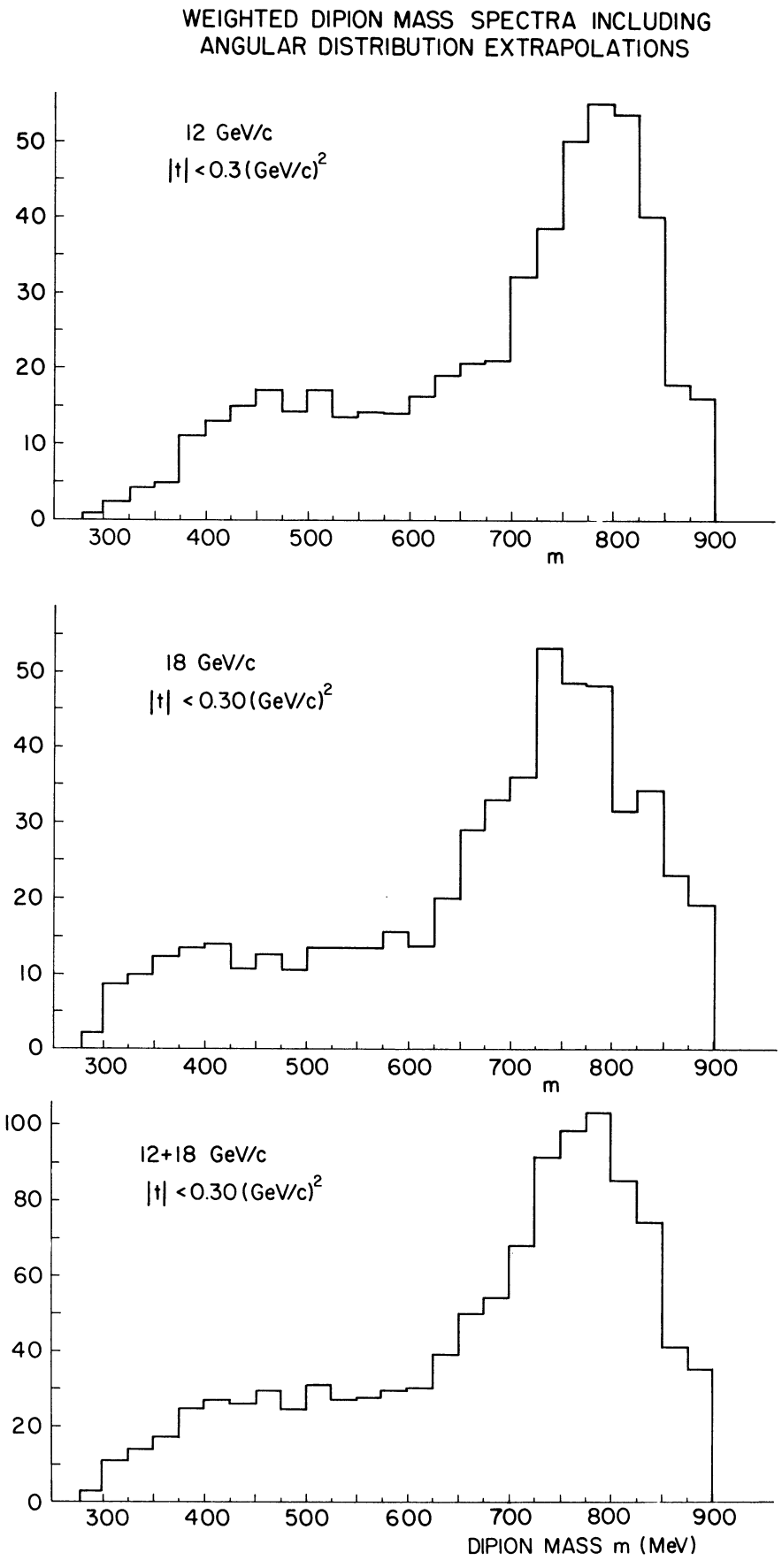
WEIGHTED DIPION MASS SPECTRA INCLUDING
ANGULAR DISTRIBUTION EXTRAPOLATIONS
12 GeV/c
|t| < 0.3 (GeV/c)²
18 GeV/c
|t| < 0.30 (GeV/c)²
12+18 GeV/c
|t| < 0.30 (GeV/c)²
0
10
20
30
40
50
60
80
100
300
400
500
600
700
800
900
m
DIPION MASS m (MeV)

Figure 24

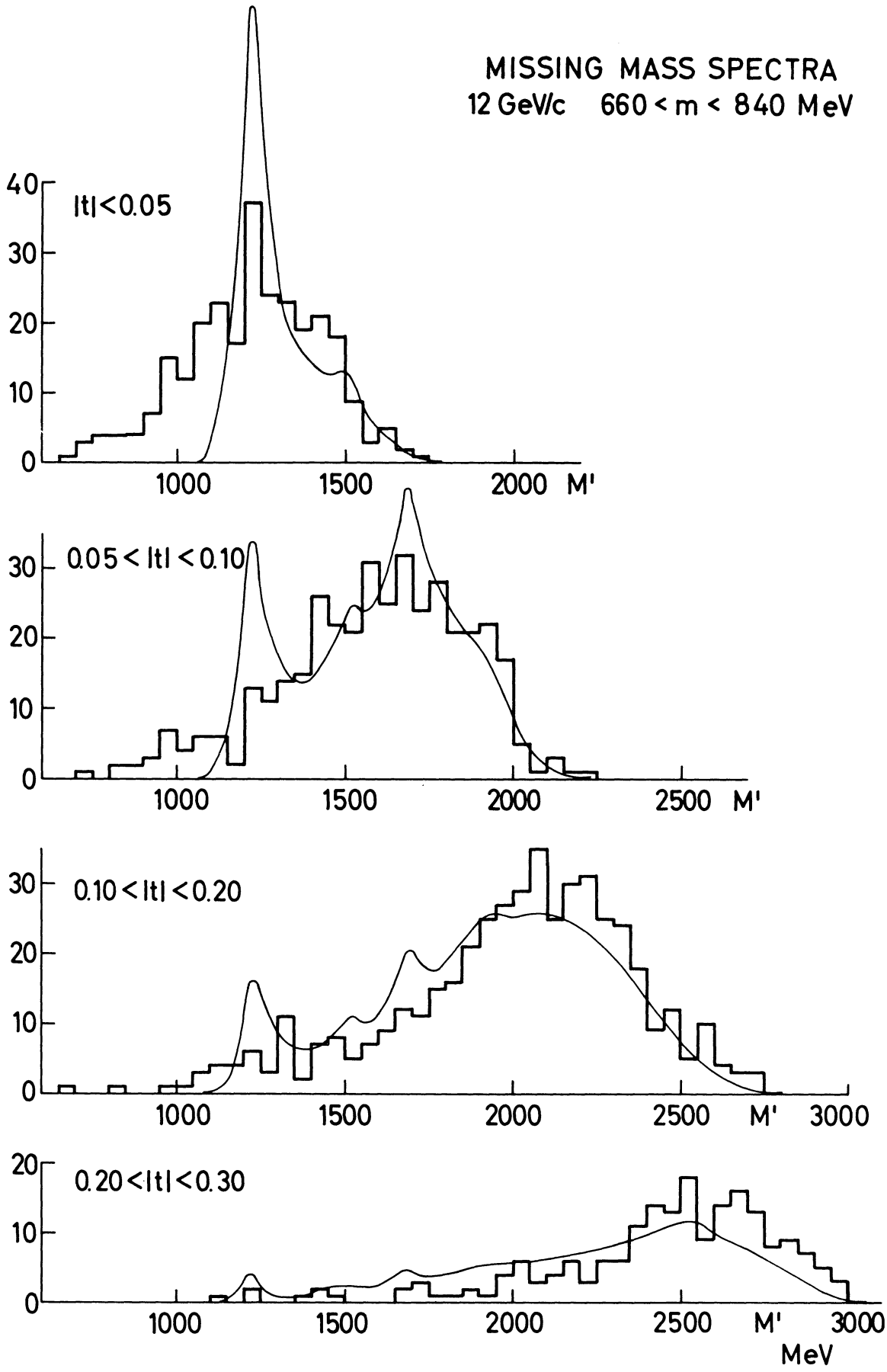
MISSING MASS SPECTRA
12 GeV/c 660 < m < 840 MeV
|t|<0.05
0.05 < |t| < 0.10
0.10 < |t| < 0.20
0.20 < |t| < 0.30
M'
MeV

Figure 25

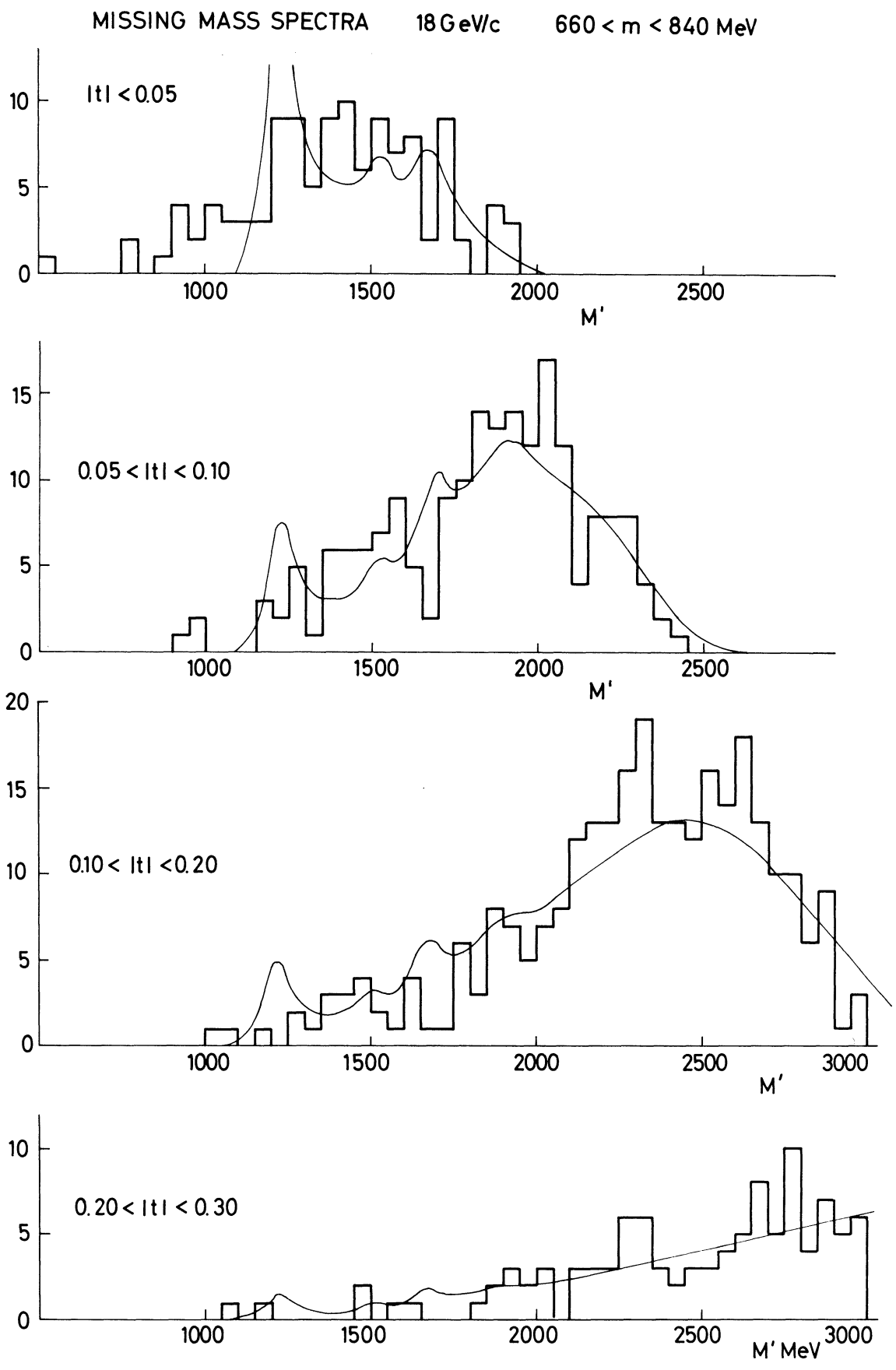
MISSING MASS SPECTRA 18 GeV/c 660 < m < 840 MeV
|t| < 0.05
0.05 < |t| < 0.10
0.10 < |t| < 0.20
0.20 < |t| < 0.30
M'
M' MeV

Figure 26

RATIO OF ISOTROPIC TO TOTAL DIPION-PION SCATTERING, Q, VS. MOMENTUM TRANSFER, t, FOR DIFFERENT DIPION MASS INTERVALS

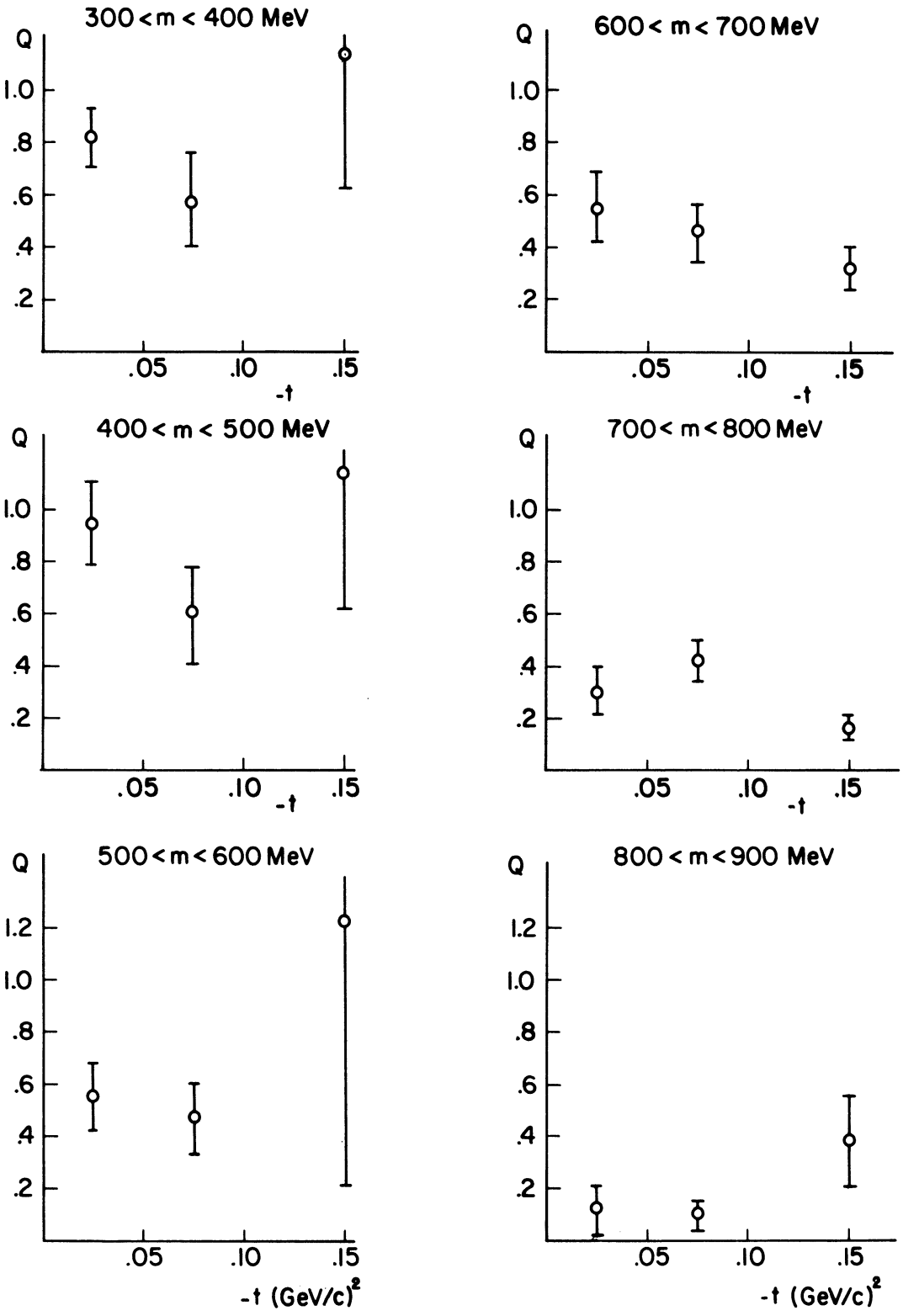

Figure 27

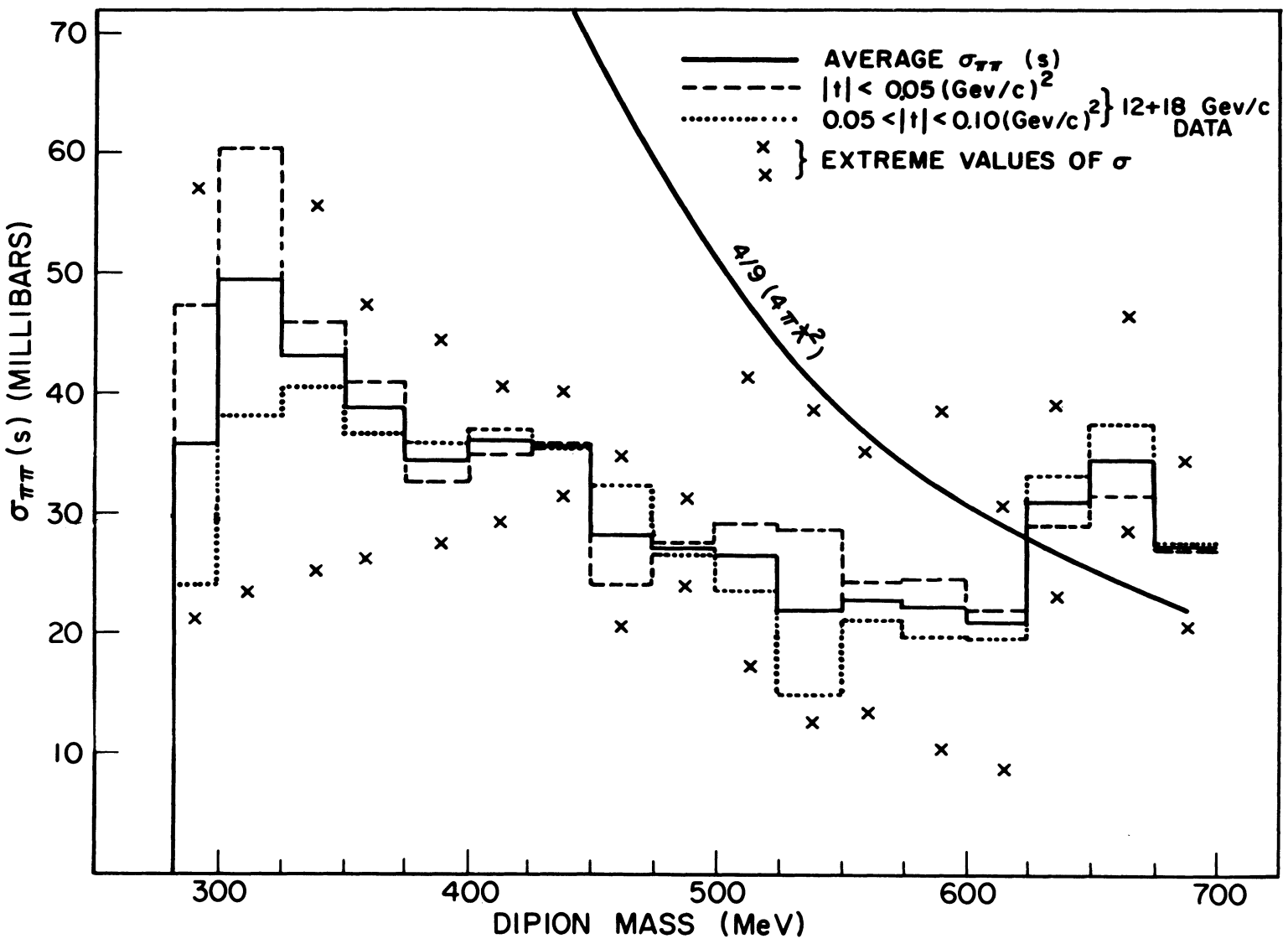
S-WAVE CROSS SECTION FOR $\pi^+ + \pi^- \rightarrow \pi^+ + \pi^-$
DEDUCED FROM PERIPHERAL DIPION PRODUCTION
AVERAGE $\sigma_{\pi\pi}$ (s)
$|t| < 0.05$ (Gev/c)^2
$0.05 < |t| < 0.10$ (Gev/c)^2
12+18 Gev/c DATA
EXTREME VALUES OF σ
$4/9\,(4\pi\lambda^2)$
$\sigma_{\pi\pi}$ (s) (MILLIBARS)
DIPION MASS (MeV)
70
60
50
40
30
20
10
300
400
500
600
700

Figure 28

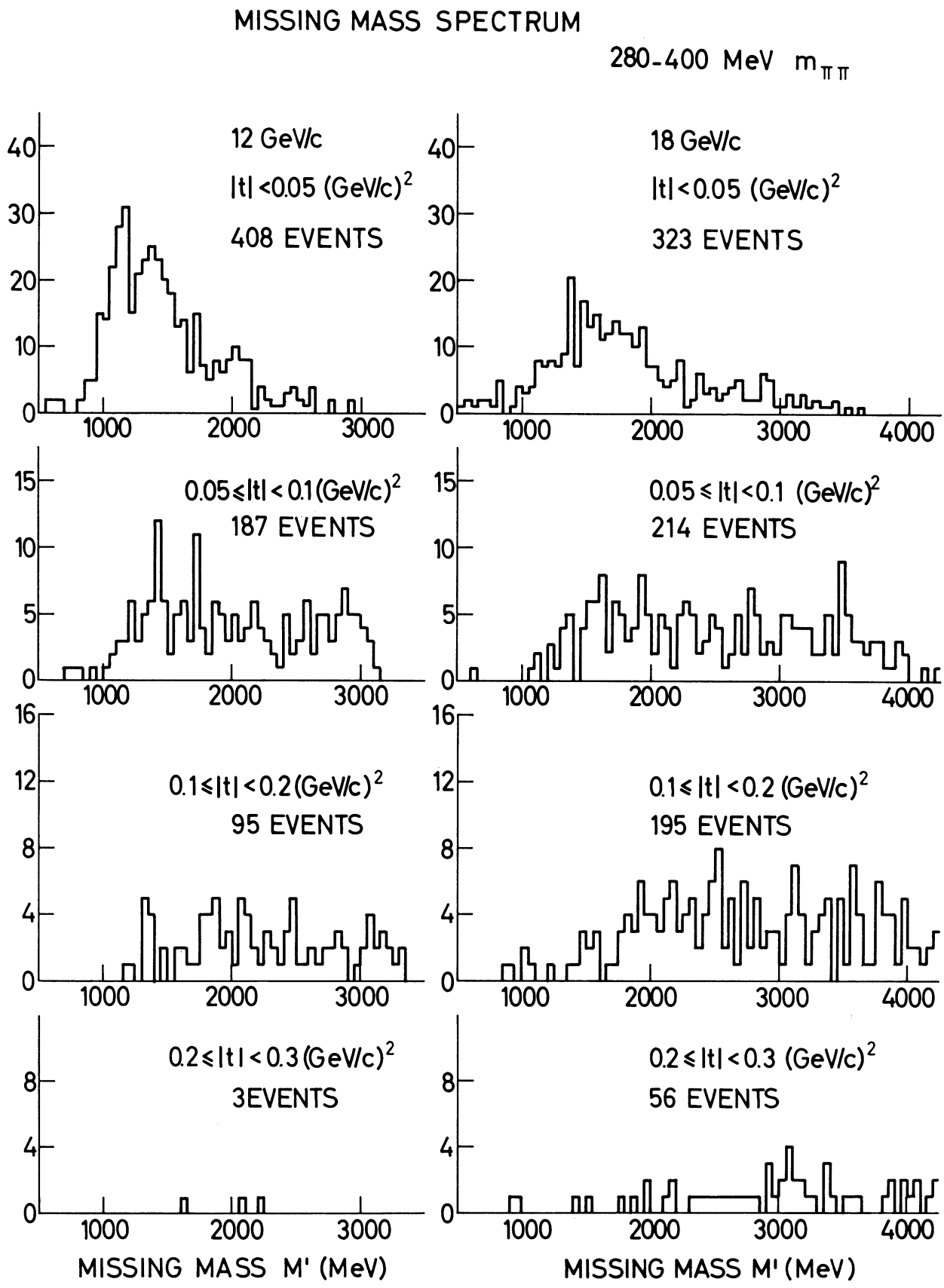
MISSING MASS SPECTRUM
280-400 MeV $m_{\pi\pi}$
12 GeV/c
|t| <0.05 (GeV/c)^2
408 EVENTS
18 GeV/c
|t| <0.05 (GeV/c)^2
323 EVENTS
0.05≤|t| <0.1(GeV/c)^2
187 EVENTS
0.05 ≤ |t| <0.1 (GeV/c)^2
214 EVENTS
0.1≤|t| <0.2(GeV/c)^2
95 EVENTS
0.1≤ |t| <0.2 (GeV/c)^2
195 EVENTS
0.2≤|t| <0.3(GeV/c)^2
3EVENTS
0.2≤ |t| <0.3 (GeV/c)^2
56 EVENTS
MISSING MASS M' (MeV)
MISSING MASS M' (MeV)

Figure 29

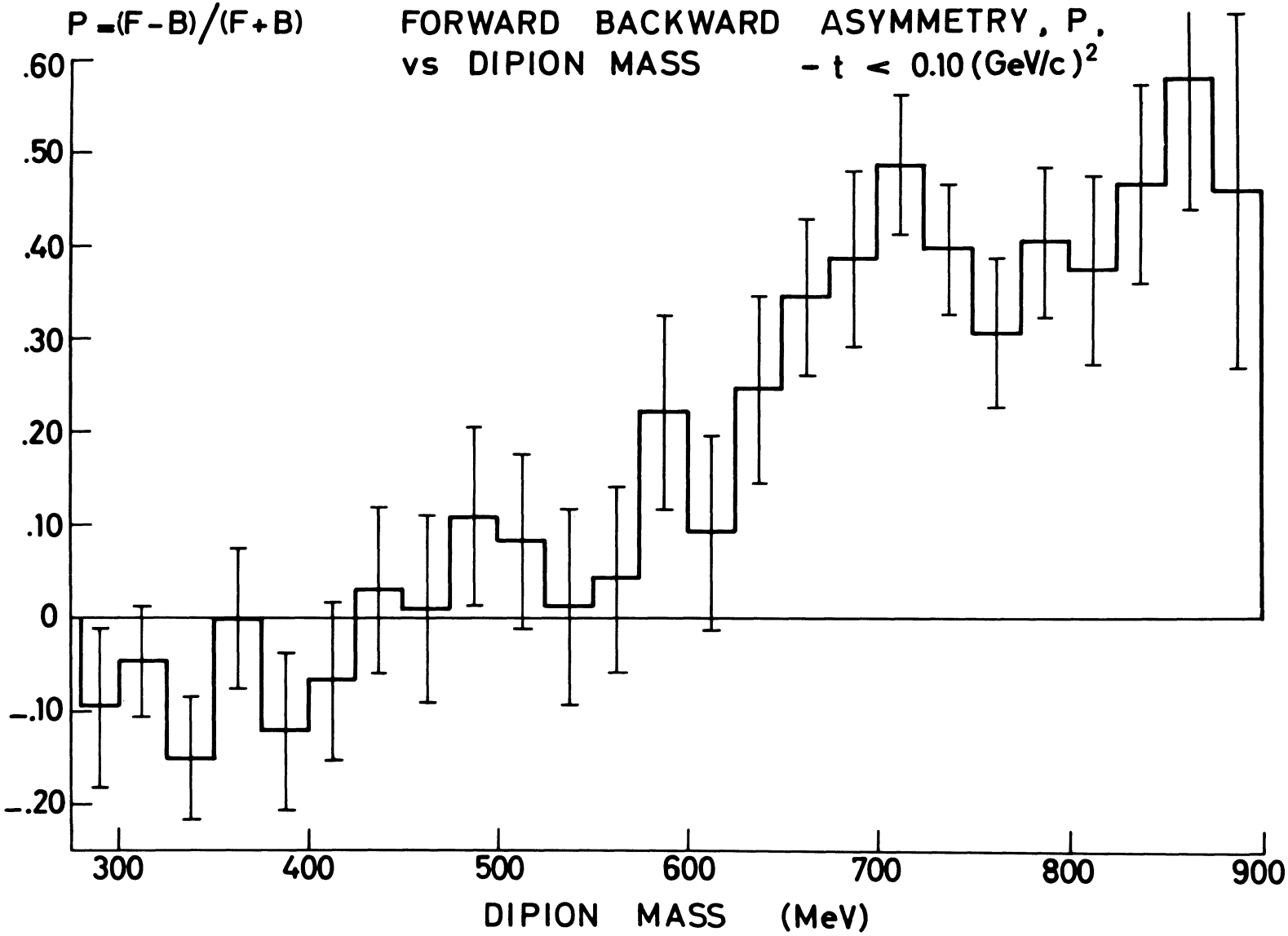
P = (F - B)/(F + B)
FORWARD BACKWARD ASYMMETRY, P,
vs DIPION MASS
- t < 0.10 (GeV/c)²
.60
.50
.40
.30
.20
.10
0
-.10
-.20
300
400
500
600
700
800
900
DIPION MASS (MeV)

Figure 30

DIPION FORWARD-BACKWARD ASSYMMETRY, P^*, VS. MOMENTUM TRANSFER, t, FOR DIFFERENT DIPION MASS INTERVALS

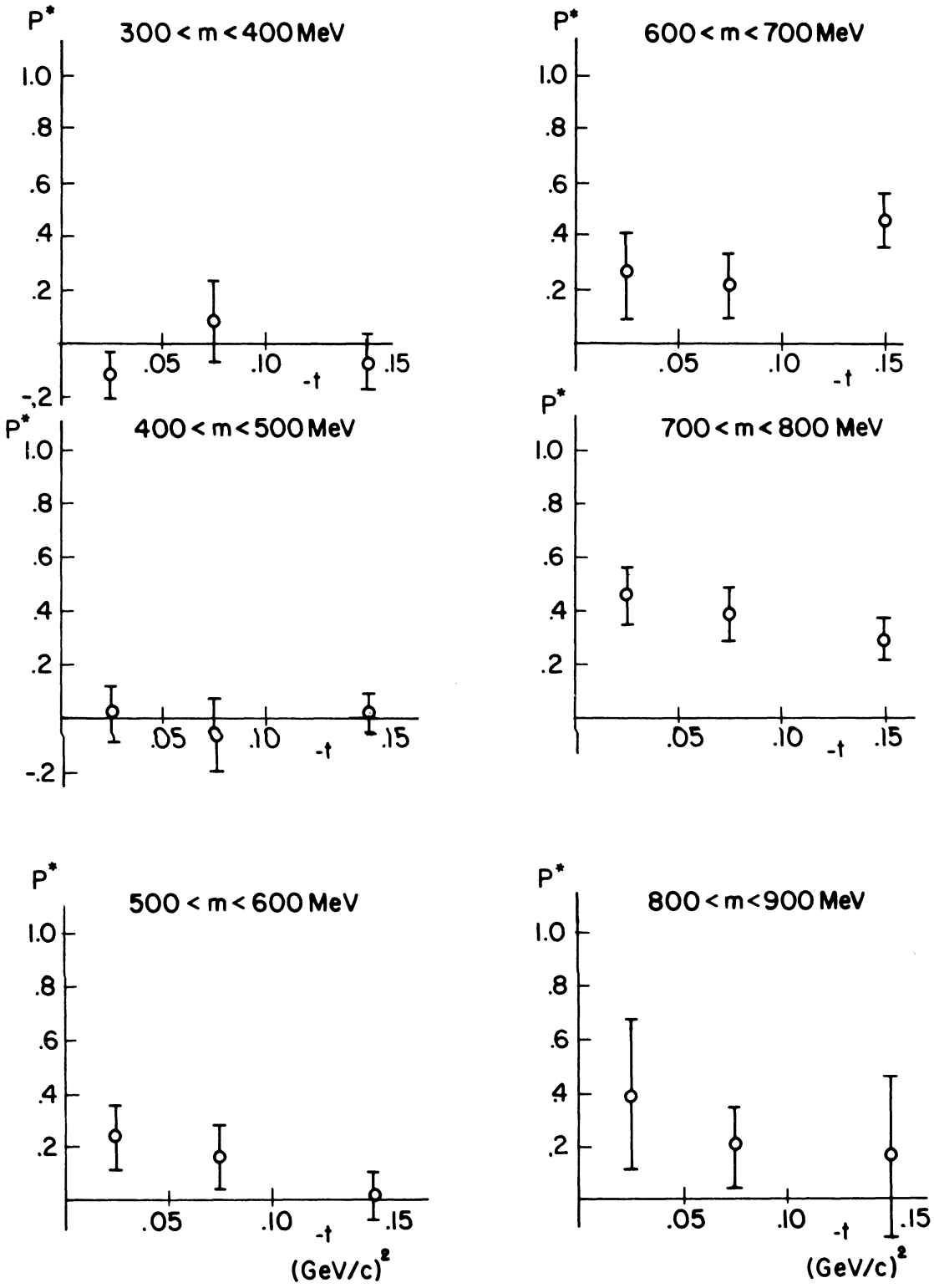

Figure 31

Unclassified
Security Classification

DOCUMENT CONTROL DATA - R&D

(Security classification of title, body of abstract and indexing annotation must be entered when the overall report is classified)

1. ORIGINATING ACTIVITY *(Corporate author)*
The University of Michigan
Department of Physics
Ann Arbor, Michigan

2a. REPORT SECURITY CLASSIFICATION
Unclassified

2b GROUP

3. REPORT TITLE
PERIPHERAL DIPION PRODUCTION BY PIONS OF 12 AND 18 GeV/c

4. DESCRIPTIVE NOTES *(Type of report and inclusive dates)*
Technical Report No. 24

5. AUTHOR(S) *(Last name, first name, initial)*
Jones, L. W., Bleuler, E., Caldwell, D. O., Elsner, B., Harting, D., Middelkoop, W. C., Zacharov, B.

6. REPORT DATE	7a. TOTAL NO. OF PAGES	7b. NO. OF REFS
June 1966	120	28

8a. CONTRACT OR GRANT NO.
Nonr-1224(23)
b. PROJECT NO.
NR-022-274
c.
d.

9a. ORIGINATOR'S REPORT NUMBER(S)
03106-24-T

9b. OTHER REPORT NO(S) *(Any other numbers that may be assigned this report)*

10. AVAILABILITY/LIMITATION NOTICES
Reproduction in whole or in part is permitted for any purpose of the U. S. Government.

11. SUPPLEMENTARY NOTES

12. SPONSORING MILITARY ACTIVITY
Department of the Navy
Office of Naval Research
Washington, D. C.

13. ABSTRACT

A spark chamber experiment on the peripheral production of 9245 pion pairs by 12 and 18 GeV/c incident pions is reported and analyzed in terms of the one pion-exchange model wherein the final state at the nucleon vertex contains generally one or more pions. The relevant dynamics and kinematics appropriate to this problem are reviewed, and the experimental and analysis techniques permitting good resolution and detection bias correction are discussed in some detail. From the results, fair agreement is found between the data and the one pion exchange calculation for the ρ^0 production cross sections and the nucleon vertex missing mass spectra. The ρ^0 is found to be consistent with a single peak, and no evidence of peak splitting is observed. A search for a narrow s-wave dipion resonance is made with negative results. Normalizing to the ρ^0 meson, the s-wave $\pi^+\pi^-$ scattering cross section is computed from the abundant low dipion-mass events, giving a cross section falling smoothly from 50 mb (300 MeV) to about 20 mb (600 MeV). No evidence of an s-wave resonance is found in this range of energies. The forward-backward pion-pion scattering asymmetry is found to be negative by 2-1/2 standard deviations below 450 MeV consistent with a negative and falling J=T=0 phase shift. The extrapolated forward-backward asymmetry and the s-wave cross section are both consistent with a J=T=0 phase shift near $|90°|$ near 750 MeV.

DD FORM 1 JAN 64 1473

Unclassified
Security Classification

14. KEY WORDS	LINK A		LINK B		LINK C	
	ROLE	WT	ROLE	WT	ROLE	WT

INSTRUCTIONS

1. ORIGINATING ACTIVITY: Enter the name and address of the contractor, subcontractor, grantee, Department of Defense activity or other organization *(corporate author)* issuing the report.

2*a*. REPORT SECURITY CLASSIFICATION: Enter the overall security classification of the report. Indicate whether "Restricted Data" is included. Marking is to be in accordance with appropriate security regulations.

2*b*. GROUP: Automatic downgrading is specified in DoD Directive 5200.10 and Armed Forces Industrial Manual. Enter the group number. Also, when applicable, show that optional markings have been used for Group 3 and Group 4 as authorized.

3. REPORT TITLE: Enter the complete report title in all capital letters. Titles in all cases should be unclassified. If a meaningful title cannot be selected without classification, show title classification in all capitals in parenthesis immediately following the title.

4. DESCRIPTIVE NOTES: If appropriate, enter the type of report, e.g., interim, progress, summary, annual, or final. Give the inclusive dates when a specific reporting period is covered.

5. AUTHOR(S): Enter the name(s) of author(s) as shown on or in the report. Enter last name, first name, middle initial. If military, show rank and branch of service. The name of the principal author is an absolute minimum requirement.

6. REPORT DATE: Enter the date of the report as day, month, year; or month, year. If more than one date appears on the report, use date of publication.

7*a*. TOTAL NUMBER OF PAGES: The total page count should follow normal pagination procedures, i.e., enter the number of pages containing information.

7*b*. NUMBER OF REFERENCES: Enter the total number of references cited in the report.

8*a*. CONTRACT OR GRANT NUMBER: If appropriate, enter the applicable number of the contract or grant under which the report was written.

8*b*, 8*c*, & 8*d*. PROJECT NUMBER: Enter the appropriate military department identification, such as project number, subproject number, system numbers, task number, etc.

9*a*. ORIGINATOR'S REPORT NUMBER(S): Enter the official report number by which the document will be identified and controlled by the originating activity. This number must be unique to this report.

9*b*. OTHER REPORT NUMBER(S): If the report has been assigned any other report numbers *(either by the originator or by the sponsor)*, also enter this number(s).

10. AVAILABILITY/LIMITATION NOTICES: Enter any limitations on further dissemination of the report, other than those imposed by security classification, using standard statements such as:

(1) "Qualified requesters may obtain copies of this report from DDC."

(2) "Foreign announcement and dissemination of this report by DDC is not authorized."

(3) "U. S. Government agencies may obtain copies of this report directly from DDC. Other qualified DDC users shall request through _____."

(4) "U. S. military agencies may obtain copies of this report directly from DDC. Other qualified users shall request through _____."

(5) "All distribution of this report is controlled. Qualified DDC users shall request through _____."

If the report has been furnished to the Office of Technical Services, Department of Commerce, for sale to the public, indicate this fact and enter the price, if known.

11. SUPPLEMENTARY NOTES: Use for additional explanatory notes.

12. SPONSORING MILITARY ACTIVITY: Enter the name of the departmental project office or laboratory sponsoring *(paying for)* the research and development. Include address.

13. ABSTRACT: Enter an abstract giving a brief and factual summary of the document indicative of the report, even though it may also appear elsewhere in the body of the technical report. If additional space is required, a continuation sheet shall be attached.

It is highly desirable that the abstract of classified reports be unclassified. Each paragraph of the abstract shall end with an indication of the military security classification of the information in the paragraph, represented as *(TS)*, *(S)*, *(C)*, or *(U)*

There is no limitation on the length of the abstract. However, the suggested length is from 150 to 225 words.

14. KEY WORDS: Key words are technically meaningful terms or short phrases that characterize a report and may be used as index entries for cataloging the report. Key words must be selected so that no security classification is required. Identifiers, such as equipment model designation, trade name, military project code name, geographic location, may be used as key words but will be followed by an indication of technical context. The assignment of links, rules, and weights is optional.